MICROCHIP LASERS: AN INVESTIGATION OF TRANSVERSE MODE DEFINITION, SPECTRAL SELECTIVITY AND NOVEL FREQUENCY MODULATION\UP-CONVERSION TECHNIQUES.

Neil MacKinnon

A Thesis Submitted for the Degree of PhD
at the
University of St Andrews

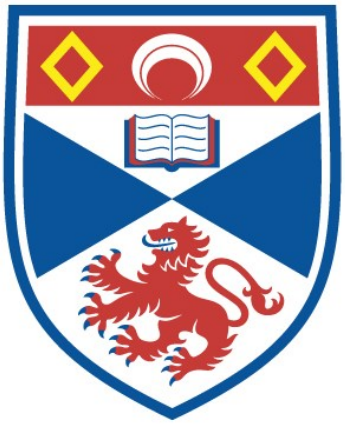

1994

Microchip Lasers: An Investigation of Transverse Mode Definition, Spectral Selectivity and Novel Frequency Modulation/Up-conversion Techniques

A Thesis Presented by
Neil MacKinnon, B.Sc.,
in Application for the Degree of
Doctor of Philosophy

May 1994

TL
B573

Declaration

I, Neil MacKinnon, hereby certify that this thesis has been composed by myself, that it is a record of my own work, and that it has not been accepted in partial or complete fulfilment of any other degree or professional qualification.

I was admitted to the Faculty of Science of the University of St. Andrews under Ordinance General No. 12 on the first of October 1990.

In submitting this thesis to the University of St. Andrews I wish access to it to be subject to the following conditions.

For a period of five years from the date of submission the thesis shall be made available for use only with the consent of the Head of School or Chairman of the Department in which the work was carried out.

I understand, however, that the title and abstract of the thesis will be published during this period of restricted access and that after the expiry of this period the thesis will be made available for use in accordance with regulations of the University Library for the time being in force, subject to any copyright in the work not being affected thereby, and a copy of the work may be made and supplied to any *bona fide* library or research worker.

Neil MacKinnon,

May 1994

Certificate

I hereby certify that the candidate has fulfiled the conditions of the Resolution and Regulations appropriate to the Degree of Ph.D.

Dr. Bruce D. Sinclair,

May 1994

Acknowledgements

I am greatly indebted to many people in St. Andrews both in my time here as an undergraduate and as a postgradute. In particular I would like to thank Dr. Bruce Sinclair for his technical assisstance on this project and his boundless enthusiasm.

In addition to my supervisor I would like to acknowledge the following for their assistance in the ruination of my liver over the past three years, having to suffer them in flat 1/172 and a few other things.

G-Gordy Gordo, Sara, Gordon K., Malx, Greg., Dunx, Finbarr, the "W" squad, Richard, Big Jazza, Colin, Angus, Cameron, Hong, David, Jonny T., Christian, Dom, Jimmy L. and all the staff at the "Whey Pat".

Abstract

In this thesis describes experimental and theoretical work is described for a class of solid-state lasers which are classified by the term "microchip". The work presented here may be grouped into two parts. Chapters 2 and 5 describe work directed towards novel frequency modulation and up-conversion and are therefore of a more developmental flavour. The work presented in chapters 3 and 4 are of a more fundamental nature and pertains to transverse mode definition and spectral selectivity in these devices.

In chapter 2 a laser diode array pumped, electro-optically tunable microchip laser is described. Based on the combined gain/non-linear material neodymium doped magnesium oxide lithium niobate (Nd:MgO:$LiNbO_3$) tuning of the six oscillating axial modes was achieved at a sensitivity of 8.9 MHz V^{-1} mm. The device operated in a fundamental spatial mode (M^2=1.1) at all the incident pump powers used. The incident pump power threshold was 32 mW and the incident pump power slope efficiency was 6.5 %. The maximum output power obtained was 13 mW. From the pump power dependence of the oscillating mode size and the thermal characteristics of the gain material it was postulated that definition of the transverse mode of operation was by a longitudinally distributed positive guiding duct.

Chapter 3 describes the mechanisms observed to define the transverse mode of operation in lithium neodymium tetraphosphate, $LiNdP_4O_{12}$, or LNP, microchip lasers. This material was of interest in this particular study in that the dn/dT of the material was negative and would clearly preclude the guiding mechanisms postulated for the Nd:MgO:$LiNbO_3$ microchip laser as described in chapter 2. The LNP microchip laser was excited by a Ti:sapphire laser and a HeNe based Fizeau interferometer was used to map out the pump induced changes in optical thickness between the cavity mirrors. Further investigation using a modified interferometer revealed that definition of the transverse mode of operation was primarily due to

pump induced input surface deformation. As expected bulk changes in the refractive index of the gain material were found not to contribute to cavity stability. The LNP output beam was found to propagate with an M^2 value of 1.05 at all the pump powers used. The LNP microchip laser was found to operate in a single axial mode up to 20 mW of output power. Above this level the output of the device consisted of the principal mode located under the 1.047 μm gain bandwidth and a cavity mode located under the 1.055 μm gain bandwidth. It was found that the single frequency performance of the device could be degraded by detuning of the pump radiation away from peak absorption although the overall performance of the device did not show such a marked dependence on gain length.

The single frequency properties of a laser diode pumped LNP device, as a function of gain length, are the subject of chapter 4. The diode pumped LNP device output exhibited the same excellent spatial characteristics of operation as the Ti:sapphire pumped device. Fourteen milliwatts of single frequency output was obtained. A model, based on spatial dephasing of longitudinal modes, was modified appropriately to predict the single frequency performance of the LNP device as a function of gain length within the resonator. The gain length was controlled by variation of the pump absorption via diode temperature tuning. The discrepancy between the observed results and predicted results was reduced when the effect of a reabsorption loss differential between the 1.047 μm and 1.055 μm modes was taken into account. The single frequency performance of the device was found to improve markedly at the highest absorption coefficients. This was postulated to be due to a pump density dependent excited state migration mechanism of a form similar to Auger recombination. The migration process manifested itself in the increased damping, over what would be expected from the upper state lifetime of the material, of a spiking train from the device.

Chapter 5 deals with developmental work on a laser diode array pumped, composite material microchip laser for green output. The device consisted of a neodymium

doped yttrium vanadate (Nd:YVO_4) gain section in intimate optical contact with a non-linear material (potassium titanyl phosphate, or KTP) for frequency doubling of the 1.064 μm line in Nd:YVO_4. Initial experiments on the device were performed using a laser diode and coupling optics. Six milliwatts of C.W. green power were obtained for 150 mW of incident pump radiation. The device operated in a near diffraction limited spatial mode (M^2=1.1) at all the incident pump powers. The oscillating waist within the device was found to be pump power dependent. The conversion of the fundamental into the green was observed to be only slightly reduced by the variable elliptical eigenpolarisation within the cavity. Oscillation of two axial modes in the infra-red was observed at 6 mW of green output power. Separated by the free spectral range of the cavity the intensity ratio of the two modes was measured to be eight to one from the stronger to weaker mode. The amplitude stability of the green output was examined using a photodiode and spectrum analyser. No evidence of periodic amplitude fluctuations in the green could be observed. The lack of the so-called "green-problem" was attributed to the relatively weak coupling between the two longitudinal modes in this system. Using direct coupling of the device on to the open facet of a half-Watt laser diode array 50 mW of C.W. green output was obtained for approximately 400 mW of incident pump. The output of the device exhibited the same spatial characteristics as that obtained from the lens coupled device. In experiments with a two-Watt laser diode array 130 mW of near diffraction limited spatial output was achieved at 650 mW of incident pump power. This advance represents the "state-of-the-art" microchip laser development.

Table of Contents

Chapter 1: Introduction

In this chapter a brief historical perspective of the early development of diode pumped solid-state lasers will be given before the current status of research and application of laser diode pumped microchip lasers is discussed.

Particular emphasis will be given to the generation of coherent, visible light from all-solid-state, or holosteric, systems including direct generation from large band-gap II-VI semiconductors, frequency up-conversion of III-V semiconductor laser diodes and frequency doubling of laser diode pumped solid-state lasers. A perspective will then be given on the new breed of solid-state lasers reported on in this thesis; the microchip laser. The accent will be on the potential for mass-production of such devices, the present status of research and the current realisation of some of the many commercial applications of this device concept. Finally, future avenues of development for this device concept will be outlined as will the contribution of the work presented in this thesis to the evolution of the microchip laser.

Section 1.1: Historical Perspective

The potential use of diode lasers as pump sources was first identified by Newman [1] who demonstrated that 1.06 μm fluorescence in Nd:$CaWO_4$ could be excited by 880 nm radiation generated by electron hole recombination in a GaAs light emitting diode (LED). The first lasing action in a diode pumped system was demonstrated by Keyes and Quist [2] at the Lincoln laboratories of the Massachusetts Institute of Technology who used a bank of GaAs diodes to transversely excite a U^{3+}:CaF_2 laser rod. The diagram below (figure 1.1.1) shows schematically the first diode pumped solid-state laser.

All these preliminary experiments were, however, conducted with the diodes and gain media at either liquid nitrogen or liquid helium temperatures but clearly exhibited the

potentialities of diode pumping in producing a laser source of simpler structure and superior performance than in lamp pumped systems.

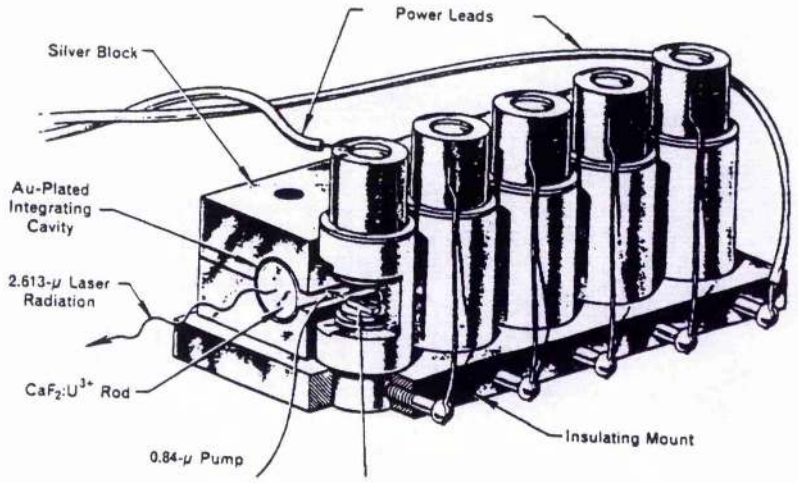

Figure 1.1.1: Schematic of First Laser Diode Pumped Solid-state Laser. In the Above Figure the Laser Rod is 4 cm Long and 3 mm in Diameter (after [2])

As development of GaAs laser diode technology continued apace in the seventies solid-state laser research focused on exploitation of new gain media, mostly utilising the Nd^{3+} ion as the active ion, and investigation of the so-called "end-pumping" excitation geometry [3,4]. This excitation geometry, although limited in the respect that usually only one laser diode may be used to excite the solid-state laser, has the major advantage of facilitating excellent overlap between pump volume and the lasing mode. The first such demonstration of this pumping configuration was successfully performed by Ostermeyer in 1977 [3,4]. In addition to the improved pumping configuration and miniaturisation, laser diodes have considerable advantages over lamp pumping configurations. These include firstly an overall increase in the efficiency of a solid-state laser, secondly, decreased thermal loading in the solid-state gain material and thirdly extended pump-source lifetime. The increase in overall efficiency comes from the fact that although lamps convert electrical energy to optical energy at an efficiency slightly better than laser diodes (80% efficiency for flashlamps as opposed to 30 to 50 % efficiency for laser diodes) the optical energy produced by laser diodes is concentrated in a very narrow spectral band which is well matched to

the absorption of Nd^{3+}. The figure below shows the overlap between the emission spectra of a pulsed flashlamp and a laser diode and the absorption profile of 1% Nd:YAG [5].

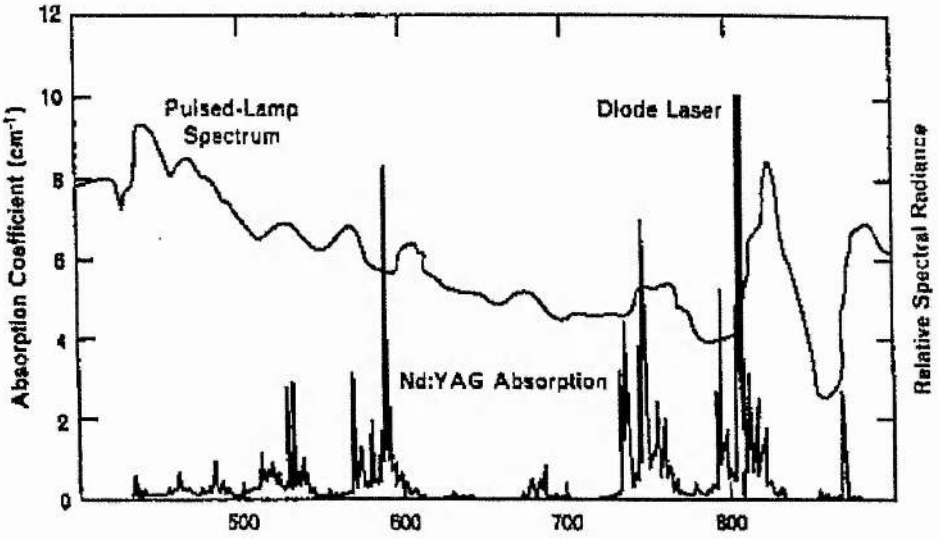

Figure 1.1.2: Emission Spectra of Pulsed Lamp and AlGaAs Laser Diode in Comparison with Absorption Profile of 1 % Nd:YAG (after [5])

The increase in efficiency with laser diode pumping also has the advantage that the waste heat deposited in the solid-state gain material is less and reduces the requirements for active heat sinking. Additional deleterious heat effects such as thermally induced birefringence and catastrophic failure of the laser material are also reduced. Since the early nineteen nineties increasing research and commercial efforts have centred on laser diode pumps as replacements for lamp pumped lasers. The prime stimulus for this move away from lamp pump sources has been the decrease in the unit costs associated with the manufacture and purchase of semiconductor laser diodes. With increasing competition in the marketplace and the collapse of many defence oriented markets, unit cost of $1 per Watt of continuous wave optical radiation is currently available with, in many cases, mounting and packaging costs far out-weighing the costs of the manufacture of the laser diode itself.

All-solid-state lasers, which enjoy the term "holosteric" meaning "wholly solid" to describe them, therefore have a promising future as spatial and spectral purifiers and energy compression devices for laser diode pumps. The increased radiance and

coherence of the output beam from holosteric lasers is more desirable in a number of important applications such as holography, photomedicine, optical storage and micromachining. The upper state lifetime of lasing ions in crystalline hosts is usually much larger than that in semiconductor laser diodes making significant energy storage/extraction possible in solid-state lasers. As will be outlined below in addition to these highly desirable properties the advent of up-conversion or frequency division of laser lines in solid-state gain media, via non-linear optics, has extended the spectral coverage of holosteric lasers from the ultra-violet to the eyesafe region [1-6].

1.2: Compact, Solid-state Visible Laser Sources

The most direct route perhaps to visible coherent radiation will be the use of a semiconductor laser diode itself emitting in the blue-green. To date work in this area has focused on the large band-gap II-VI semiconductors and in particular ZnSe [7,8]. The first successful demonstration of a blue-green laser diode was performed by Haase et al. [7] who achieved pulsed lasing action at 490 nm in ZnSe at 77 K. Continuous wave lasing action in the blue-green in (Zn, Cd) Se/ZnSe multiple quantum well lasers at 100 K was first reported by Jeon et al. [8] in 1991. Since then continued work has focused on attempting to minimise the deleterious thermal problems associated with the poor electrical contacts present in these devices.

Although a practical blue-green laser diode is still some years away perhaps significant research effort has also been placed on the development of C.W. high power laser diodes emitting in the red. Such laser diodes have been developed to replace the ubiquitous 633 nm HeNe laser in many current applications such as interferometry, photodynamic therapy and illumination. In addition to HeNe laser replacement in their low-power forms these red semiconductor lasers may form the basis for optical storage systems of increased information density over that possible with current 780 nm semiconductor laser diode based optical styli. Geels et al. [9] have reported up to 70 mW of fundamental spatial mode 676 nm radiation from a InGaAlP semiconductor laser diode. In their high power, array configurations

AlGaInP semiconductor laser diodes may form the pump source for new vibronic solid-state media such as Cr^{3+} doped lithium strontium aluminium fluoride (Cr:LiSAF) [10]. To this end Spectra Diode Laboratories (SDL) have developed a half-Watt, C.W., ten emitter array which introduces the possibility of holosteric self-modelocked lasers. Indeed, utilising half-Watt 670 nm laser diodes polarisation coupled such all-solid-state, self-mode-locked Cr:LiSAF laser have recently been reported [11].

More currently practicable options for producing visible light from laser diodes is to exploit frequency up-conversion of AlGaAs semiconductor laser diode output. AlGaAs III-V semiconductor laser diode technology has the advantage over other laser diodes in that the technology has considerably matured in the last five years. Another stimulus to this approach has been the wealth and breadth of research devoted to the growth and characterisation of non-linear crystals for frequency doubling techniques. The disadvantages of this approach are that in order to achieve reasonable second harmonic powers an external resonant cavity must be utilised to enhance the fundamental flux within the non-linear crystal [12,13]. Such a scheme, as outlined below, has however been used to produce 41 mW of blue (428 nm) C.W. radiation from 140 mW of diode radiation [13].

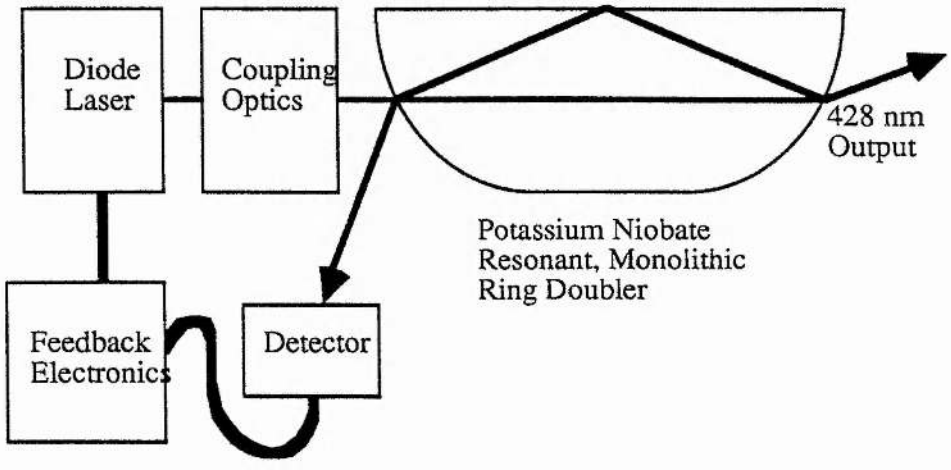

Figure 1.2.1: Resonantly Enhanced Second Harmonic Generation of the Output from a GaAlAs Laser Diode Using a Monolithic Ring (after [13])

The above scheme has further drawbacks in that additional drive electronics are needed to keep the frequency of the laser diode locked to that of the external, enhancement cavity. Additionally the non-linear material offering the highest effective non-linear coefficient for blue generation is potassium niobate ($KNbO_3$) which is notoriously difficult to grow, process and coat. The advent of high power AlGaAs M-MOPA (monolithic master oscillator power amplifier) devices offering single frequency diffraction limited near infra-red powers in the one Watt range may to a certain extent obviate the need for resonantly enhanced doubling schemes with the possibility of single pass doubling in $KNbO_3$. However, the blue-green (478 nm) powers generated are still relatively modest (less than 2 mW) and the M-MOPA device is very sensitive to feedback into the power amplifier section of the device [14].

Perhaps the most commonly used method to generate coherent visible radiation is frequency doubling of diode pumped, near-infrared lasers. Diode pumped, solid-state lasers satisfied long before laser diodes the necessary requirements on coherence, spectral purity, beam brightness and affordability for efficient non-linear conversion. In addition to these highly desirable properties the three most familiar lasing lines possible in neodymium (0.946 μm, 1.064 μm and 1.32 μm) when frequency doubled would give access to the three primary colours (blue, green and red respectively).

The two most commonly used routes to frequency double are to place the nonlinear crystal within the solid-state laser cavity to exploit the very high intra-cavity circulating fields. This approach is the simplest configuration as the non-linear crystal does not require to be locked in any way to the frequency of the solid-state laser. The intra-cavity method does however have the disadvantage that coupling between oscillating axial modes may cause chaotic amplitude fluctuations in the second harmonic output of the laser [15]. This may however be solved by constraining the laser to operate on a single axial mode. In addition to the longitudinal mode coupling in the non-linear crystal use of certain doubling materials may perturb the

eigenpolarisation of the cavity by acting as a temperature sensitive waveplate within the cavity [16] To eliminate these problems the externally resonantly enhanced doubling technique decouples the lasing and the non-linear conversion processes although, as has been outlined above in the consideration of doubled AlGaAs laser diodes, this approach incurs additional cost and complexity. Despite this considerable effort has been given to a monolithic, ring resonant geometry which has successfully generated 29 mW of green light in the non-linear material magnesium doped lithium niobate ($MgO:LiNbO_3$) [12] from a diode pumped ring Nd:YAG laser.

A third recently available option is to combine the lasing properties of the neodymium ion with the non-linear properties of a frequency doubling crystal so as to produce a self-frequency-doubled solid-state laser which may be diode pumped. Two of these materials are lithium niobate co-doped with magnesium oxide and neodymium ($Nd:MgO:LiNbO_3$) and neodymium doped yttrium aluminium borate (Nd:YAB). $Nd:MgO:LiNbO_3$ is a material which has been configured for the first time as an electro-optically tunable microchip laser at St. Andrews and characterised in this thesis (chapter 2). Nd:YAB has produced up to 23 mW of green radiation for 400 mW of incident diode pump [17]. However, Nd:YAB suffers from significant reabsorption of the generated green and has to date been difficult and expensive, in comparison with currently available non-linear crystals, to obtain due to growth problems.

The final option for producing coherent visible radiation is via up-conversion processes in fibre lasers [18.19]. However to date up-conversion in fibre lasers has relied on the exploitation of somewhat exotically doped fibres the pulling of which is still very much a virtuoso art and is far from reaching the volume production associated with conventional silica optical fibres. In addition to fabrication difficulties associated with up-conversion fibre lasers alignment of the pump source, which may either be a solid-state laser or diode laser, needs to be accurate to within sub-micron tolerances. Up-conversion in bulk media is yet another route to visible output from diode pumped systems but currently the visible powers obtained are relatively modest

(in the 2 mW range) and usually require liquid helium cooling of the up-conversion media [20].

Clearly coherent, visible light is, at the moment, most desirably obtained from frequency doubled, diode pumped solid-state lasers. For specialist high power uses flashlamp pumping of doubled solid-state lasers is still an option but is increasingly being superseded by diode pumped designs.

1.3: Derivatives and Applications of Diode Pumped Microchip Lasers

Microchip laser was a term first coined by Mooradian to describe a slice of gain material, polished to plane/parallel etalon tolerances, with dielectric mirrors deposited directly on to the gain material surfaces to define a standing wave lasing cavity [21]. Microchip lasers are excited optically and longitudinally, ideally, by AlGaAs semiconductor laser diodes. Microchip lasers are amongst the smallest and cheapest laser designs available and offer in their many forms desirable operating features comparable with larger conventional laser designs. These desirable characteristics and potentialities of microchip lasers form the technical content of this thesis. These features include linearly polarised emission, fundamental spatial mode operation, high power single frequency operation, electro-optically tunability, pulsed operation and frequency manipulation [21]

One of the highly desirable properties of microchip lasers is their amenability to mass production techniques. The following novel method of high volume production has been developed at the Lincoln Laboratories of the Massachusetts Institute of Technology and is outlined schematically below [21].

Producing a slight radius of curvature on one of the microchip laser surfaces has the effect of relaxing the tolerances on the optical parallelism between the cavity mirrors and of reducing slightly the device threshold [21]. However, alignment of the pump source with the centre of the curved surface is necessary unlike a plano/plano structure.

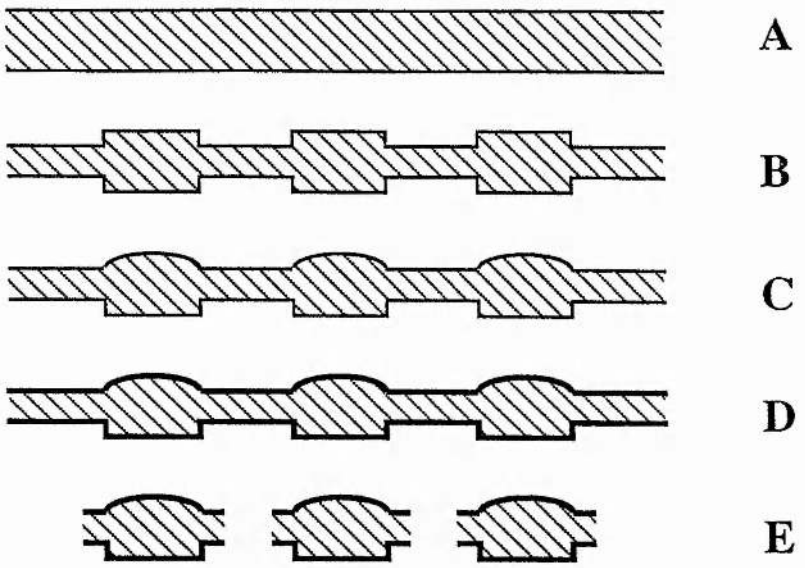

Figure 1.3.1: Five Step Process for Volume Fabrication of Curved Mirror Microchip Lasers (after [21])

The five step process begins (step A) with a slice of gain material being processed so as to produce a thin wafer of gain material with plane parallel surfaces. The next step (step B) is to scribe the wafer with a grid pattern as shown. Step C involves polishing one surface of the wafer again. During this additional stage of polishing a natural rounding of the polished surface occurs as polishing slurry tends to build up directly underneath the polishing element. The degree of curvature on the re-worked surface is a function of several factors including the grade of slurry being used, the width of the scribe between each device and the force applied during polishing [21]. The wafer is then coated appropriately to form the microresonator (step 4). The wafer is then diced along the direction of the scribes which define the transverse dimensions of the microchip laser (step 5). Using this method of fabrication has the clear advantage that for example one polishing run is sufficient for processing the wafer of gain material in each of the two processing steps. Similarly, with one coating run every device is coated appropriately. In this thesis smaller quantities of microchip lasers were required for the investigative experiments and a more conventional fabrication method was employed. Usually a starting block was sectioned first into a number of blanks which were then mounted on a polishing block and worked simultaneously to

the required thicknesses and tolerances. The finished devices were then coated simultaneously. Although not as novel as the mass production method outlined above the techniques employed by our fabricators clearly indicated the cost effectiveness of the microchip laser approach. A number of components were worked and coated simultaneously and expenditure on the acquisition of these devices was essentially dictated by the cost of polishing runs or coating chamber time.

Since their invention microchip lasers have seen rapid commercialisation especially in the field of optical fibre communications. Particularly important has been the application of an electro-optically tunable microchip laser, operating at 1.32 μm, to CATV (common antenna television) systems. This particular, composite material microchip laser is shown schematically below.

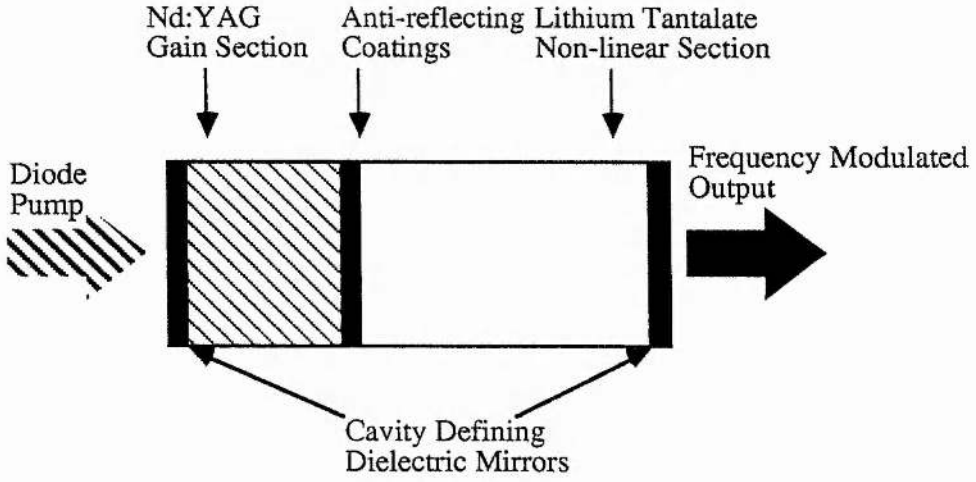

Figure 1.3.2: Electro-optically Tunable, Composite Material Microchip Laser(after [22])

Such an electro-optically tunable microchip laser enables, via frequency shift keying (FSK), the transmission of multiple high definition television (HDTV) channels. The prime advantage in using the electro-optically tunable microchip laser is the higher 1.3 μm output power available with up to 15 mW C.W. single frequency, tunable power from a microchip laser as opposed to 5 mW from a semiconductor laser. Another bonus is the excellent beam quality from a microchip laser which facilitates coupling of the signal light into an optical fibre. A very similar electro-optically

tunable device, though based on a single crystal, is the subject of chapter 2 of this thesis.

Yet another commercial exploitation of novel microchip laser designs has been the commercialisation of Q-switched microchip lasers [23], operating at 1.32 μm, as the basis for OTDR (optical time domain reflectometry) machines. The composite material, Q-switched microchip laser is shown diagramatically below.

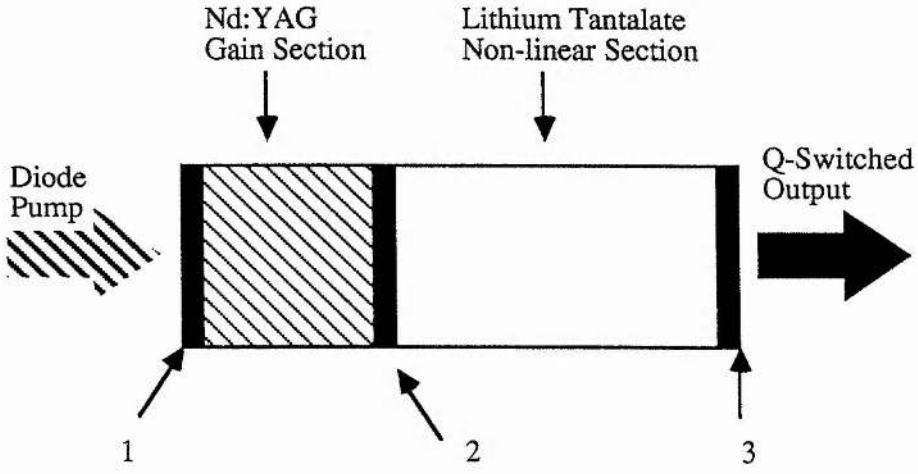

Figure 1.3.3: Electro-optically Q-switched Microchip Laser (after [23])

The $LiTaO_3$ non-linear section acts as a voltage controlled output coupler, between surfaces 2 and 3 for the Nd:YAG gain section between surfaces 1 and 2 [23]. The Nd:YAG gain section effectively defines the frequency properties of the device. Surface 1 is coated so as to be highly reflective at the lasing wavelength, surface 2 is coated so as to be 95 % reflective at the lasing wavelength and surface 3 is coated so as to be 50 % reflective at the lasing wavelength. The thickness of the gain section (the distance between surfaces 1 and 2) is chosen so as to ensure that only one axial mode is present under the principal gain bandwidth. In the low Q-state the optical thickness of the $LiTaO_3$ is adjusted such that the etalon formed by surfaces 2 and 3 becomes highly transmitting for the allowed frequencies defined by surfaces 1 and 2. In the high Q state the etalon is tuned so as to become effectively highly reflecting for the defined frequency of operation of the gain section. Using this approach

Zayhowski et al. have reported single frequency peak power pulses of 25 kW in sub-nanosecond pulse durations [23].

Optical time domain reflectometry (OTDR) is a powerful field technique for determining the attenuation on an optical link down its entire length and resolving the length dependence of the attenuation loss [24]. A short, single frequency, high intensity pulse of the appropriate wavelength is launched down the optical fibre under consideration and the backscattered light is recorded as a function of time. The diagram below illustrates a possible backscatter plot from an optical fibre under examination.

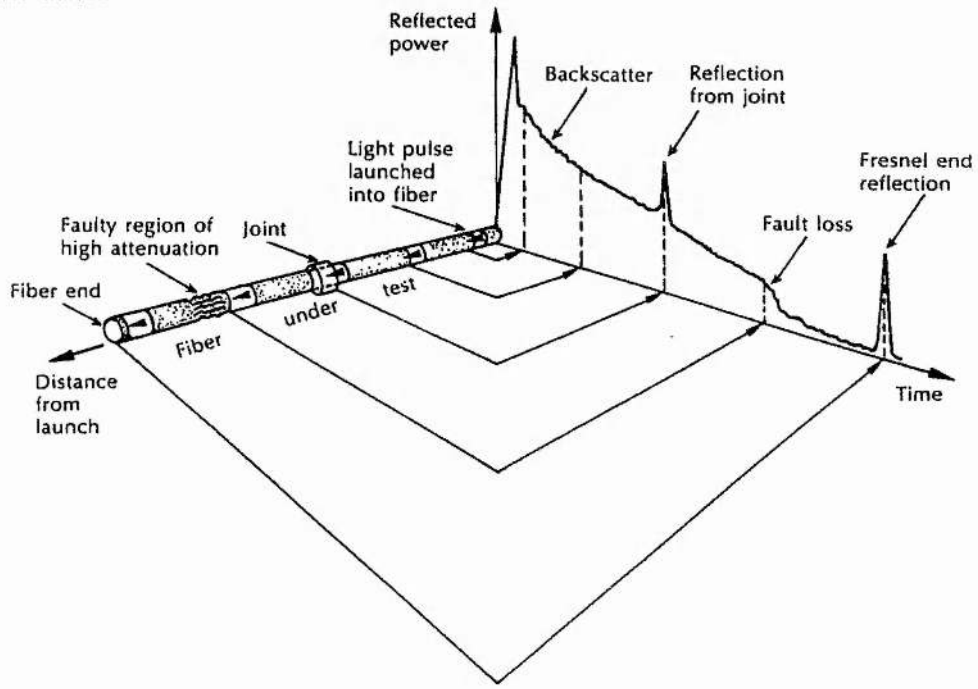

Figure 1.3.4: Testing of the Attenuation of an Optical Fibre Link Using Optical Time Domain Reflectometry (after [24])

The Q-switched microchip laser with its shorter, higher energy pulses offers an improvement in the resolution and range of optical time reflectometry techniques over that currently achievable using intensity modulated semiconductor laser diodes [24]. In addition to the two specific applications outlined above microchip lasers and their derivatives may well find further application in areas such as optical storage systems

displays and other fields presently the domain of larger, conventional diode pumped solid-state lasers.

This thesis contributes to the understanding and evolution of the microchip laser. The material presented here consists of both the developmental work associated with the microchip laser and some of its derivatives and experimental work directed towards further understanding of some of the processes involved in the fundamental operating characteristics of the device. In chapter two a laser diode pumped electro-optically tunable microchip laser is described. The electro-optically tunable microchip laser presented in this chapter was the first ever single crystal electro-optically tunable device. The gain material utilised was lithium niobate co-doped with both neodymium and magnesium oxide (Nd:MgO:$LiNbO_3$). The work presented in chapter 2 is the first configuration of this novel gain/non-linear material in a microchip laser format [25,26].

Chapters 3 and 4 present material of a somewhat more fundamental flavour although the results obtained therein shed new and important light on how the fundamental operating characteristics of microchip lasers may be turned to the advantage of the device designer. Chapter 3 presents work on the examination of the definition of the transverse mode of operation in lithium neodymium tetraphosphate (LNP) microchip lasers when excited by a titanium doped sapphire laser simulating a laser diode pump source. Chapter 4 outlines the performance of an LNP microchip laser when pumped by a half-Watt laser diode array. More detailed consideration is then given to modelling the single frequency properties of microchip laser with a model based on spatial dephasing of adjacent longitudinal modes. The model is adapted appropriately to ascertain the importance of the gain length within the gain material in defining the spectral purity of the output. Chapter 5 presents perhaps the most exciting developmental work carried out for this thesis. In this chapter the design and performance of a composite material microchip laser for the production of green radiation is described. Potentialities for the scaling of these devices, in terms of output

powers, are demonstrated and discussed. Finally in the conclusions section the work presented in this thesis is summarised with particular emphasis on the achievements which further understanding of the operating mechanisms in microchip lasers and contribute to the dynamic field of miniature, visible lasers. The conclusions are then supplemented by a brief discussion of the options for further derivatives of the microchip laser both to extend the spectral coverage of these devices and allow their novel intensity modulation.

References

[1] R. Newman, J. Appl. Phys., **34**, p. 437, (1963)

[2] R. J. Keyes and T. M. Quist, Appl. Phys. Lett., **4**, p. 50, (1964)

[3] L. J. Rosenkrantz, J. Appl. Phys., **43**, no. 11, p.4603, (1972)

[4] F. W. Ostermeyer, I.E.E.E. J. Quant. Electron., **QE-13**, no. 1, p. 1, (1977)

[5] T. Y. Fan, Lincoln Laboratory Journal, **3**, no. 3, p. 415, (1990)

[6] R. Allen, L. Esterowitz, L. Goldberg, J. R. Weller and M. Storm, Electron. Lett., **22**, no. 18, p. 947, (1986)

[7] M. A. Haase, J. Qui, J. M. Depuydt and H. Vheng, Appl. Phys. Lett., **59**, no. 11, p. 1272, (1991)

[8] H. Jeon, J. Ding, A. V. Nurmikko, H. Luo, N. Samarth and J. Furdyna, Appl. Phys. Lett., **59**, no. 11, p. 1293, (1991)

[9] R. S. Geels, D. W. Nam, D. P. Bour, D. W., Treat, D. F. Welch and D. R. Scifres, Paper CMA4, Conference on Lasers and Electro-optics, (CLEO), 1992, Technical Digest Series,Vol. 11, Optical Society of America, Washington D. C., U. S. A., p. 11

[10] R. S. Geels, D. F. Welch, D. R., Scifres, D. P. Bour, D. W. Treat and R. D. Bringans, Paper CThQ3, Conference on Lasers and Electro-optics, (CLEO), 1993, Technical Digest Series, Vol. 12, Optical Society of America, Washington D. C., U. S. A., p. 478

[11] R. Mellish, P. W. French, J. R. Taylor, P. J. Delfyett, L. T. Florez, Paper AMD3, Optical Society of America Topical Meeting on Advanced Solid-State Lasers, Technical Digest, p. 16, 1994

[12] W. J. Kozolovsky, C. D. Nabors and R. L. Byer, I.E.E.E. J. Quant. Electron., **QE-24**, no. 6, p.913, (1988)

[13] W. J. Kozolovsky, W. Lenth, E. E. Latta, A. Moser and G. L. Bona, Appl. Phys Lett., **56**, no. 23, p. 2291, (1990)

[14] R. Waarts, R. Parke, D. Nam, D. Welch, D. Mehuys, R. Lang, S. O' Brien and D. Scifres, Paper CWC2, Conference on Lasers and Electro-optics, (CLEO), 1993, Technical Digest Series, Vol. 12, Optical Society of America, Washington D. C., U. S. A., p. 240

[15] T. Baer, J. Opt. Soc. Am. B, **3**, (1986), p. 1175

[16] T. Sasaki, T. Kojima, A. Yokotani, O. Oguri and S. Nakai, Opt. Lett., **16**, no. 21, p. 1665, (1991)

[17] J. Bartschke, R. Knappe, C. Becher, B. Beier, K. J. Boller and R. Wallenstein, Paper ATuD4, Optical Society of America Topical Meeting on Advanced Solid-State Lasers, Technical Digest, p. 22, 1994

[18] D. Piehler, Laser Focus World, Nov. 1993, 30

[19] S. G. Grubb, K. W. Bennet, R. S. Cannon, W. F. Humer, Paper CPD18, Conference on Lasers and Electro-optics, (CLEO), 1992, Technical Digest Series, Vol. 11, Optical Society of America, Washington D. C., U. S. A., p.35

[20] T. Herbert, W. P. Risk, R. M. MacFarlane and W. Lenth, Paper WE5, Optical Society of America Topical Meeting on Advanced Solid-State Lasers, Technical Digest, 1990

[21] J. J. Zayhowski, Lincoln Laboratory Journal, **3**, no. 3, p. 427, (1990)

[22] J. J. Zayhowski, P. A. Schulz and S. R. Henion, Paper CThR4, Conference on Lasers and Electro-optics, (CLEO), 1993, Technical Digest Series, Vol. 11, Optical Society of America, Washington D. C., U.S.A., p. 484

[23] J. J. Zayhowski,and C, Dill III, Paper CMI7, Conference on Lasers and Electro-optics, (CLEO), 1992, Technical Digest Series, Vol. 11, Optical Society of America, Washington D. C., U.S.A., p. 54

[24] J. M. Senior, "Optical Fiber Communications", Second Edition, Prentice Hall International Series in Optoelectronics, p. 825

[25] N. MacKinnon, C. J. Norrie and B. D. Sinclair, Paper CThS12, Conference on Lasers and Electro-optics, (CLEO), 1993, Technical Digest Series, Vol. 11, Optical Society of America, Washington D. C., U.S.A., p. 496

[26] N. MacKinnon, C. J. Norrie and B. D. Sinclair, J. Opt., Soc., Am., B, **11**, no. 3, p. 1, (1994)

Chapter 2: An Electro-optically Tunable Neodymium Doped Magnesium Oxide Lithium Niobate (Nd:MgO:$LiNbO_3$) Microchip Laser Pumped by a Laser Diode Array.

Introduction

In this chapter the structure and characterisation will be discussed for a single material, laser diode array pumped, electro-optically tunable microchip laser fabricated from lithium niobate co-doped with magnesium oxide and neodymium (Nd:MgO:$LiNbO_3$). We shall first briefly consider the uses for such ultra-compact tunable sources and the specific properties of this material which combines the gain properties of the Nd^{3+} ion with the non-linear properties of lithium niobate. The relevant analysis of the linear electro-optic effect in $LiNbO_3$ is then considered so as to yield a value for the expected electro-optic tuning coefficient of the device. The pump power induced definition of the transverse mode of operation in this material is discussed in comparison with that existing in Nd:YAG microchip lasers. The experimentally obtained operating characteristics of the Nd:MgO:$LiNbO_3$ device are then described and set in context with other similar devices.

2.1: Applications of Electro-optically Tunable Devices and Properties of Nd:MgO:$LiNbO_3$.

Solid-state lasers with the unique property of electro-optically induced frequency agility have two main uses. These are, firstly, frequency modulated optical communications in coherent optical fibre communications via frequency shift keying[1] (FSK) and, secondly, rapid beam pointing [2]. In the first example, frequency shift keying, zeroes and ones are represented by different spectral components in order to convey digital information. The advantage in using FSK techniques in a coherent fibre optic

communication system is that the laser source itself can be modulated directly and consequently unlike amplitude shift keying (ASK) or phase shift keying (PSK) [1] there is no need for an external modulator for the carrier wave. In fibre optic systems using semiconductor laser diodes as the laser source frequency modulation is accomplished by rapid changes in the injection current [1]. In the second example fast, one dimensional pointing of a laser beam may be accomplished by the use of a frequency tunable source and a diffraction grating [2]. The rapid, electro-optically induced frequency shift of the laser is translated into positional agility in a time interval very much faster than can be accomplished using mechanical techniques [2]. Clearly an ultra-compact, robust, electro-optically tunable device such as a laser diode pumped tunable microchip laser, of the appropriate output power, would be a useful component in the systems outlined above.

Neodymium doped magnesium oxide lithium niobate (Nd:MgO:$LiNbO_3$) is an optically anisotropic, negative uniaxial, solid-state laser material which combines the excellent gain properties of the neodymium ion with the non-linear and electro-optic properties of $LiNbO_3$. The material $LiNbO_3$ suffers from photorefractive damage [3], especially at shorter wavelengths [3], though this is ameliorated by the inclusion of around 5% magnesium oxide. The material suffers from fluorescence quenching so the active ion concentration is usually kept usually fairly low (< 0.5%). However despite the presence of fluorescence quenching the material exhibits good lasing characteristics with an upper state lifetime of around 100 μs for 0.2% neodymium concentration [3]. The principal lasing characteristics of Nd:MgO:$LiNbO_3$ for the polarisation exhibiting the highest optical gain (i.e. for lasing in a polarisation direction parallel to the crystal c-axis which we shall define as being the π-polarised direction) are shown in figure 2.1.1 in comparison with the principal characteristics of Nd doped YAG.

The wavelength of operation exhibiting the highest optical gain is located at 1.084 μm and is polarised in a direction parallel to the crystal c-axis. The fluorescence spectrum of this transition is shown below in figure 2.1.2. In the orthogonal, σ, polarisation gain

is observed at a slightly longer wavelength of 1.093 μm though with a stimulated emission cross-section approximately one fourth of that at 1.084 μm.

Material	$\sigma_{em.}$ (x 10 $^{-19}$ cm ^{2})	$\tau_{fluor.}$ (μs)	Active Ion Conc.
Nd:MgO:$LiNbO_3$	1.8 (π-polarised)	100	0.2 %
Nd:YAG	3.5	230	1.0 %

Figure 2.1.1: Principal Lasing Characteristics of Nd:MgO:$LiNbO_3$ (after [3]) and principal characteristics of Nd doped YAG

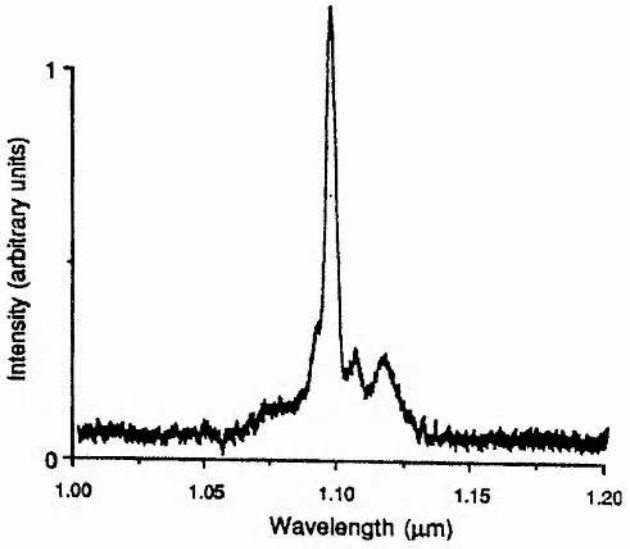

Figure 2.1.2: Fluorescence Spectrum for c-axis-polarised Emission

However the full-width, half-maximum linewidth of the 1.084 μm principal transition in Nd:MgO:$LiNbO_3$ at 3.5 nm is significantly larger than the 1.064 μm transition of the Nd^{3+} ion in the host material YAG [4] .

We obtained from Crystal Technology a batch of Nd:MgO:$LiNbO_3$ material with an active ion concentration of approximately 0.2%. The MgO dopant concentration was approximately 5%. With the above active ion concentration the peak absorption of the pump radiation was found to be 0.2 mm^{-1} at 806 nm. The absorption of the pump radiation for the pump polarised along the crystal c-axis may be seen below.

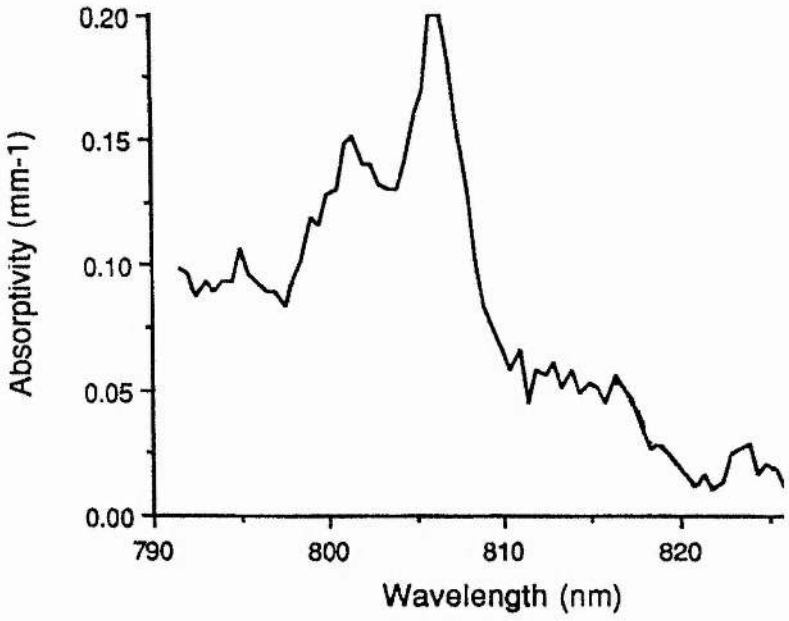

Figure 2.1.3: Pump Absorption in Nd:MgO:$LiNbO_3$ Crystal (0.2 % Nd)

Adopting the appropriate conventions pertaining to optically uniaxial crystals [5] the material was cut to provide a starting piece for propagation along the crystal y-axis [5] which would allow laser oscillation on the 1.084 μm, high gain, π-polarised line [3].

2.2 Crystallographic Orientation of Nd:MgO:$LiNbO_3$ Device and Analysis of the Linear Electro-optic Effect in $LiNbO_3$.

The purpose of this section is to describe the crystallographic orientation of the Nd:MgO:$LiNbO_3$ material as it is configured in a microchip format and then derive a value for the expected tuning sensitivity of the device using the electro-optic coefficients for the host material $LiNbO_3$. Before the analysis it will be useful to consider the orientation of our Nd:MgO:$LiNbO_3$ material. The figure below also relates the dielectric axes to the direction of propagation of the laser emission through the crystal and the directions of both high and low gain polarisation. In general in the configuration outlined in figure 2.2.1 two mutually-orthogonal linearly-polarised modes can exist. Each mode, because of the birefringence of the material, will experience a different velocity of propagation i.e. a different refractive index.

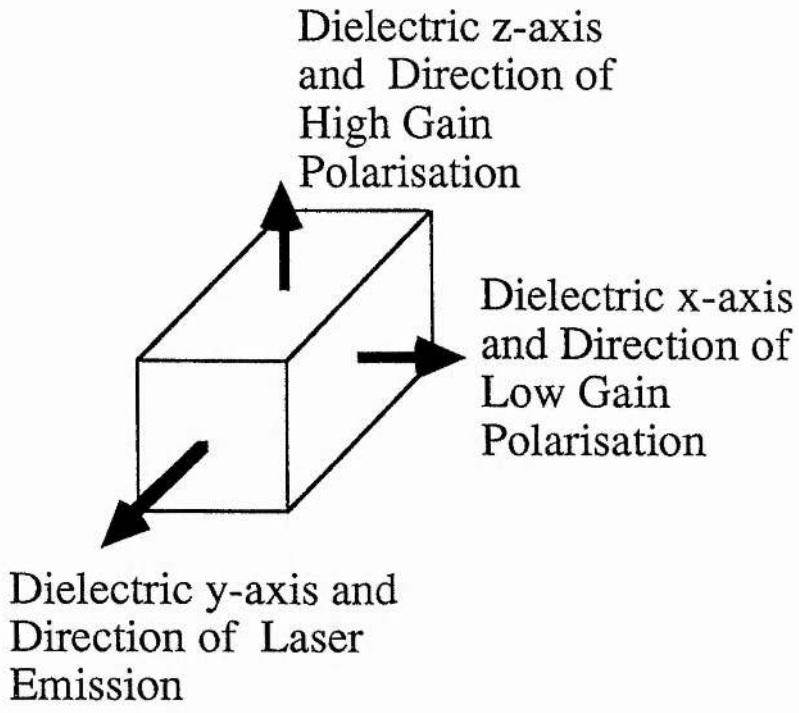

Figure 2.2.1: Crystallographic Orientation and Configuration of Nd:MgO:$LiNbO_3$ Microchip Laser.

The polarisation directions and associated refractive indices are best described by the index ellipsoid [5,6].

$$\frac{x^2}{n_x^2}+\frac{y^2}{n_y^2}+\frac{z^2}{n_z^2}=1 \qquad \text{Eqn 2.1}$$

where x, y, z are called the principal dielectric axes and are the directions along which **D** and **E** are parallel. The existence of different refractive indices for different rays polarised in different directions is a property known as birefringence. The index ellipsoid (Eqn. 2.1) describes fully the properties of propagation in a crystal and the simplest way to consider the effect of an applied electric field is to examine the changes in the constants $(1/n_x)^2$, $(1/n_y)^2$ and $(1/n_x)^2$ in equation 2.1.

In the presence of an applied electric field equation 2.1 is modified to

$$\left(\frac{x^2}{n_1^2}\right)+\left(\frac{y^2}{n_2^2}\right)+\left(\frac{z^2}{n_3^2}\right)+2\left(\frac{1}{n_4^2}\right)yz+$$
$$2\left(\frac{1}{n_5^2}\right)xz+2\left(\frac{1}{n_6^2}\right)xy=1 \qquad \text{Eqn.2.2}$$

With direct comparison with equation 2.1 and the assumption of zero electric field

$$\left(\frac{1}{n_1^2}\right)=\left(\frac{1}{n_x^2}\right)\left(\frac{1}{n_2^2}\right)=\left(\frac{1}{n_y^2}\right)\left(\frac{1}{n_3^2}\right)=\left(\frac{1}{n_z^2}\right)$$

and
$$\left(\frac{1}{n_4^2}\right)=\left(\frac{1}{n_5^2}\right)=\left(\frac{1}{n_6^2}\right)=0$$

It can be shown that [5,7] the linear change in the coefficients in equation 2.2 can be described by the equation

$$\Delta\left(\frac{1}{n^2}\right)=\sum_{j=1}^{3} r_{ij}E_j \qquad \text{Eqn. 2.3}$$

where the summation over j uses the convention

$$j=1=x;\ j=2=y:\ j=3=z$$

where x, y and z are the principal dielectric axes as outlined above and the applied electric field has components E_j, (E_x, E_y and E_z.) Equation 2.3 can best be expressed in

matrix form[5,6,7]
$$\begin{bmatrix} \Delta\left(\frac{1}{n^2}\right)_1 \\ \Delta\left(\frac{1}{n^2}\right)_2 \\ \Delta\left(\frac{1}{n^2}\right)_3 \\ \Delta\left(\frac{1}{n^2}\right)_4 \\ \Delta\left(\frac{1}{n^2}\right)_5 \\ \Delta\left(\frac{1}{n^2}\right)_6 \end{bmatrix} = \begin{bmatrix} r11 & r12 & r13 \\ \vdots & \ddots & \vdots \\ r63 & r62 & r63 \end{bmatrix} \begin{bmatrix} E_1 \\ E_2 \\ E_3 \end{bmatrix} \qquad \text{Eqn. 2.4}$$

where the 6x3 matrix with elements r_{ij} is called the electro-optic tensor [5,7]. The form of the electro-optic tensor for $LiNbO_3$ is shown below.

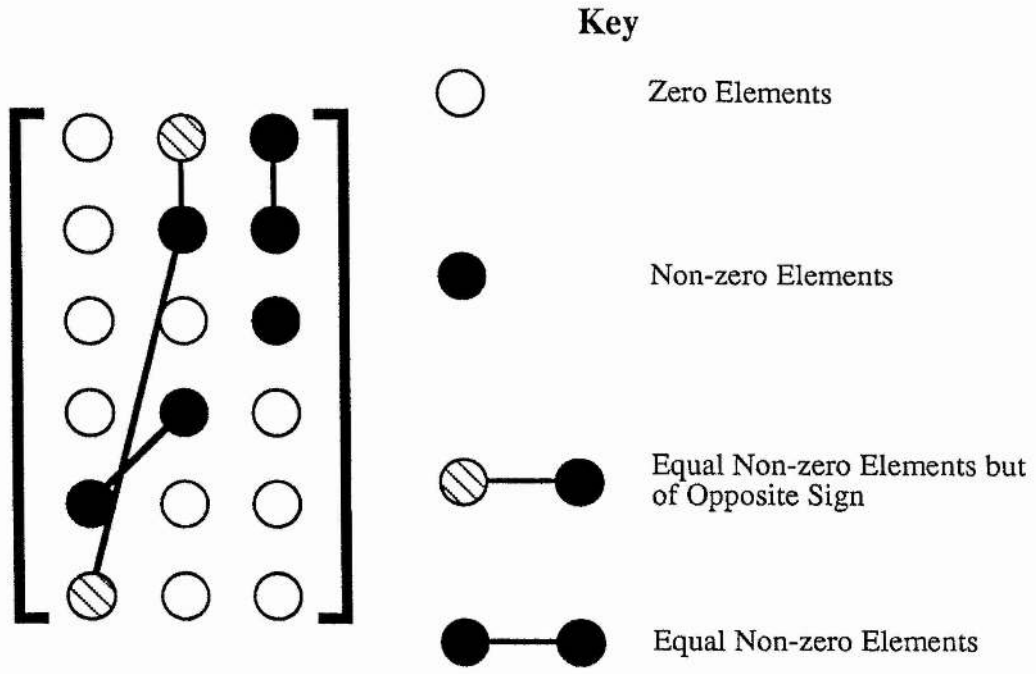

Figure 2.2.2: Form of the Electro-optic Tensor for $LiNbO_3$ (after [9]).

In general in electro-optic materials the majority of the r_{ij} elements are zero as indicated above. In $LiNbO_3$ the only non-zero elements are [6]

$$r_{33} = 30.8 \; ; \; r_{13} = 9.6 \; ; \; r_{22} = 6.8 \; ; \; r_{51} = 32.6 \;\; pmV^{-1}$$

and those linked as shown above in figure 2.2.2. Using equation 2.4 and assuming, firstly, that the electric field is applied only in the direction along the dielectric z-axis ($E_x = E_y = 0$) and secondly the only non-zero elements are the ones listed above we can obtain an electric field modified form of equation 2.1 i.e

$$\left(\frac{1}{n_o^2}\right)x^2 + \left(\frac{1}{n_o^2}\right)y^2 + \left(\frac{1}{n_e^2} + r_{33}E_z\right)z^2 = 1 \qquad \text{Eqn. 2.5}$$

where we now describe n_x and n_y as the ordinary refractive indices and n_z as the extraordinary refractive index so as to illustrate the inherent birefringence of the material. We will call a ray, travelling through the material, polarised along the

extraordinary axis the extraordinary ray and when polarised along the ordinary axis an ordinary ray. Consider the z^2 term in equation 2.5

$$\left(\frac{1}{n_e^2} + r_{33}E_z\right) \equiv \left(\frac{1}{n_e^2} + \Delta\left(\frac{1}{n_e^2}\right)\right)$$

$$\Rightarrow |r_{33}E_z| = \Delta\left(\frac{1}{n_e^2}\right) \qquad \text{Eqn. 2.6}$$

$$\Rightarrow |r_{33}E_z| = \frac{2\Delta n_e}{n_e^3}$$

from equation 2.6 we have a field dependent change in the extraordinary refractive index equal to

$$\Delta n_e = \frac{1}{2} n_e^3 r_{33} E_z \qquad \text{Eqn. 2.7}$$

It may be shown that a frequency shift $\Delta\upsilon$ in the longitudinal mode of operation is induced by a refractive index change within a laser resonator such that

$$\frac{\Delta\upsilon}{\upsilon} = \frac{\Delta n}{n} \qquad \text{Eqn. 2.8}$$

Therefore the frequency shift induced by an applied voltage V_z such that $E_z = V_z/d_z$ is

$$\Delta\upsilon = \frac{n_e^2 r_{33} V_z}{2d_z}\upsilon \qquad \text{Eqn. 2.9}$$

Where υ is the frequency of the ray polarised in the extraordinary direction .i.e.

$$\upsilon = \frac{c}{\lambda} \qquad \text{Eqn. 2.10}$$

where c is the speed of light, in vacuo, and λ is the free-space wavelength of the extraordinary ray. Substitution yields the following expression for the magnitude of the field induced frequency shift.

$$\Delta\upsilon = \frac{n_e^2 r_{33} V_z}{2\lambda d_z} c \qquad \text{Eqn. 2.11}$$

Taking n_e=2.2 [3] and r_{33}=30 pmV^{-1} [6] and λ=1.084 μm this yields a figure for the tuning sensitivity of

$$\Delta\upsilon = 10.4 \text{ MHz V}^{-1} \text{ mm}$$

At first sight the units of the tuning coefficient may seem slightly unfamiliar. However the units merely take into account the separation of the electrodes applying the electric field to the material. For example, if the electrode separation was 1 mm then the tuning sensitivity would be 10.4 MHz V^{-1} and so on.

2.3: Thermally Induced Guiding/Confinement of a Gaussian Eigenmode

The aim of this section is to outline two mechanisms by which a stable, lowest order, spatial eigenmode may be confined by a radially varying refractive index profile. The first situation to be discussed will be that of a geometrically stable duct [8,9]. The second example to be discussed will be that of a radially symmetric waveguide [9-11]. The thermally induced waveguide structure confinement mechanism is of particular importance as it has been proposed, by Zayhowski, as being the strongest mechanism present in defining the transverse mode of operation in Nd:YAG microchip lasers [12]. The physical properties of the Nd:MgO:$LiNbO_3$ are then compared with those of Nd:YAG so as to predict the most likely stability mechanism present in Nd:MgO:$LiNbO_3$.

Propagation in a geometrically stable duct depends on a radially varying refractive index profile of the form outlined below.

$$n(r)=n_0-kr^2 \qquad \text{Eqn. 2.12}$$

Where n(r) is the refractive index as a function of the radial coordinate

k is a constant defining the transverse dimensions of the duct

n_0 is the refractive index along the centre of the duct

It can be shown [13] that such a refractive index profile can "trap" a lowest order Gaussian eigenmode with a characteristic spot size given by.

$$\omega_0 = \frac{\lambda}{\pi\sqrt{k}} \qquad \text{Eqn. 2.13}$$

The physical processes occurring during confinement are straightforward. The total focussing effect along the length of the duct is sufficient to counteract the spreading, by diffraction, of the confined Gaussian beam described by ω_0 in equation 2.13. Therefore the stronger the focussing power of the duct, which is represented by a larger k value in equation 2.13 then the greater divergence of a tighter Gaussian eigenmode can be counteracted. This mechanism is expressed by equation 2.13 where the confined Gaussian spot size is inversely proportional to the root of k.

However it is worth noting that the approximations used in reaching equation 2.13 insist on a quadratic refractive index form of the type described by equation 2.12 [9-13] and that the dimensions of the confined mode (given by equation 3.5) are dependent on the wavelength of the beam.

In his study of pump power dependent transverse mode definition in Nd:YAG microchip lasers [12] Zayhowski observed that the irrespective of what the dimensions of the pump spot were (and hence the transverse dimensions of the refractive index change) the dimensions of the oscillating mode size were always larger by a factor of approximately three. Therefore the confined beam, if it were a trapped Gaussian eigenmode as outlined above, would be propagating in regions of the thermally induced refractive index change where the profile was not quadratic in nature. Therefore these observations indicated that the approximations used in determining 2.13 would no longer apply and that transverse mode definition in Nd:YAG microchip lasers is a more subtle and complex problem than Gaussian eigenmode confinement in a duct.

The refractive index profile induced in Nd:YAG microchip lasers in fact acts as a weak optical waveguide [9-10]. It can be shown [10-13] that all waveguides have only one guided mode that has no cut-off frequency (that is a free-space wavelength where the mode is unable to propagate in a particular spatial configuration) and also has dimensions larger than those of the guide itself [10,11]. This spatial mode of operation is designated the HE_{11} mode and is the lowest order mode of optical waveguides. In addition to having no cut-off frequency the HE_{11} mode is the only waveguide mode to have a single lobed, quasi-gaussian intensity profile [11]. Therefore Zayhowski, based on his experimental observations proposes that the spatial mode of operation in Nd:YAG microchip lasers is defined by a weakly guiding waveguide and is the HE_{11} guided mode. Zayhowski has also postulated that [12] the dimensions of the oscillating mode, defined by the waveguide, obey the relationship

$$\omega_{osc.} \propto P^{-\frac{1}{4}} \qquad \text{Eqn. 2.14}$$

Where $\omega_{osc.}$ is the oscillating mode size and P is the incident pump power. Zayhowski observed that the dimensions of the oscillating mode were also dependent on the average incident pump power rather than the peak incident pump power. Thermal guiding therefore has been shown, by Zayhowski, to be the strongest mechanism involved in the definition of the transverse mode of operation in Nd:YAG microchip lasers.

Nd:YAG microchip lasers are characterised by two features which are not dissimilar to those present in Nd:MgO:$LiNbO_3$. These features are, firstly, that the absorption of the pump power is relatively uniform throughout the length of the device due to the relatively low absorption coefficient for the pump [3]. Secondly, both host materials have positive dn/dT [12,14] which, in the environment described above, would result in a refractive index profile similar to the form shown in equation 2.12. It is highly likely therefore that, given similar pump conditions and reasonable optical parallelism

between the device surfaces, a very similar thermal mechanism is involved in transverse mode definition in Nd:MgO:$LiNbO_3$ microchip lasers.

2.4: Characterisation of the Laser-Diode-Array-Pumped, Electro-optically Tunable, Nd:MgO:$LiNbO_3$ Microchip Laser

2.4.1: Power Characteristics and Spatial mode of Operation

The y-cut Nd:MgO:$LiNbO_3$ material was sectioned so as to provide starting pieces with a crystallographic orientation as outlined in figure 2.2.1. These pieces were then carefully polished down to a nominal thickness of 700 μm to provide devices of high optical parallelism. The optical parallelism of the Nd:MgO:$LiNbO_3$ device was examined using a Fizeau interferometer as outlined below.

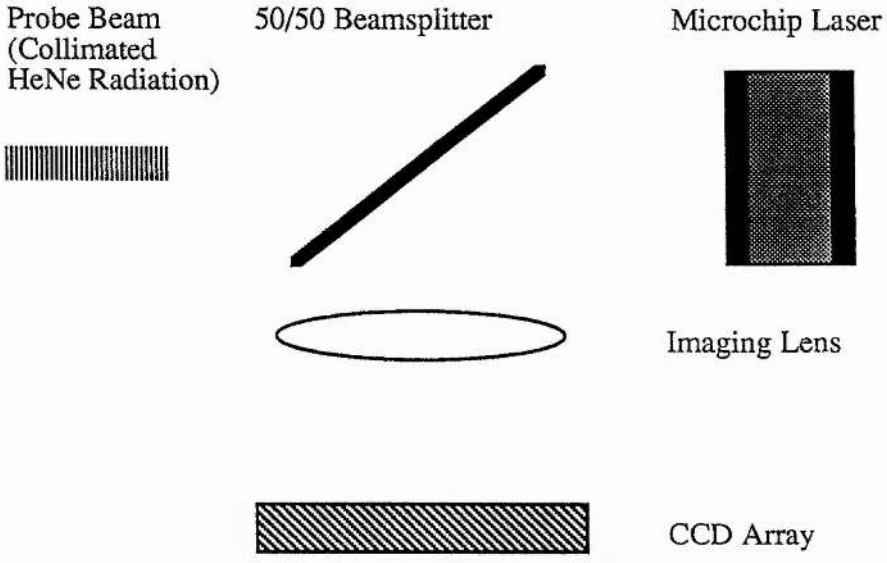

Figure 2.4.1: HeNe Based Interferometer for Examination of Optical Parallelism of Nd:MgO:$LiNbO_3$ Microchip Laser

The optical thickness of different points in a microchip laser is defined as being the product of the physical distance between the cavity defining mirrors and the refractive index of the gain material contained between the cavity mirrors. Ideally a microchip

laser should have excellent optical parallelism between the cavity mirrors at all points across the surface of the device. This clearly maximises the amount of the aperture of the device which may be pumped successfully and offers the best possible initial conditions for any pump power induced cavity stability mechanisms. Our Nd:MgO:$LiNbO_3$ device was examined in the HeNe based Fizeau interferometer [15] and, as can be seen from figure 2.4.1, the characterised device was quite far from this ideal.

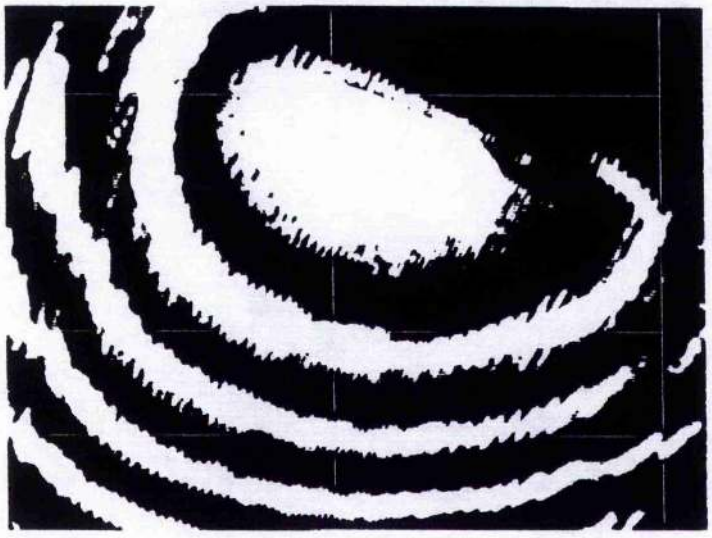

Figure 2.4.2: Equal Optical Thickness Fringes Between the Surfaces of the Characterised Nd:MgO:$LiNbO_3$ Microchip Laser.

However as can be seen from the above figure the device exhibited an area in which the parallelism of the device was reasonably good. This region is the large bright, nearly circular equal optical thickness fringe which can be seen at the top of the device. The effective radius of curvature of the area characterised by this bright fringe is large. In the direction corresponding to the Nd:MgO:$LiNbO_3$ c-axis the radius of curvature is 69 m and the orthogonal direction the radius of curvature is slightly smaller at 63 m. The device was pumped, longitudinally in the centre of this bright fringe and it was this area which, as expected, yielded the best performance. Pumping of the microchip laser away from the best area resulted in poorer output beam quality and a higher pump threshold.The input surface of the device was coated so as to be highly transmissive at the pump wavelength (R<10% @ 806 nm) and highly reflective at the lasing

wavelength (R>99.8% @ 1.084 μm). The output surface of the device was coated so as to be moderately reflective at the pump wavelength (R>70% @ 806 nm), so as to double pass the pump radiation in order to increase the overall efficiency of the device, and R=99.7% at the lasing wavelength.

During device design relatively low output coupling was chosen so as to ensure that in these short, low absorption (α_{peak}=0.2 mm^{-1}) regimes the incident pump powers needed to reach threshold could be attained by readily available laser diode pump sources. The characteristics of the finished device are summarised below in figure 2.4.2.

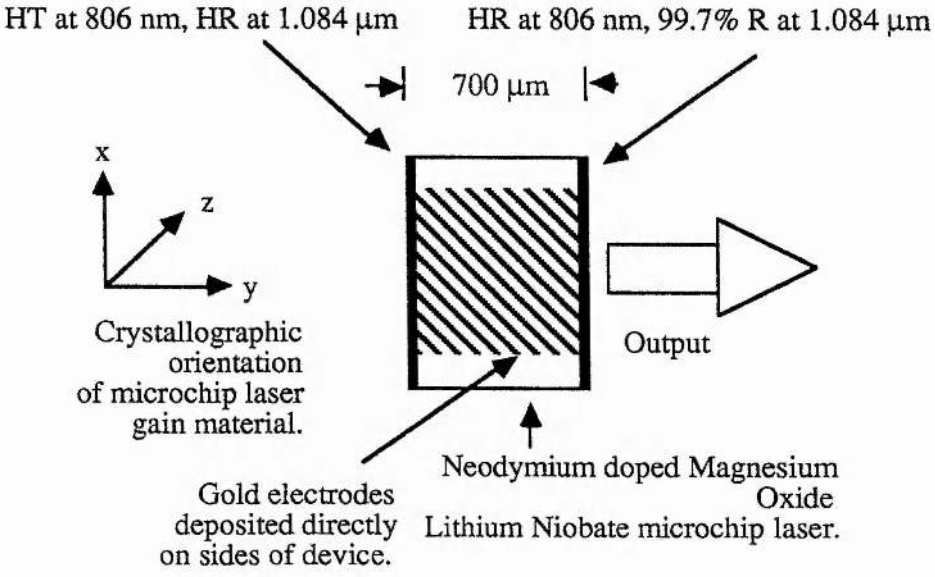

Figure 2.4.3: The Active Nd:MgO:$LiNbO_3$ Microchip Laser

The device was excited optically and longitudinally by a half-Watt laser diode array [16]. The active area of this high brightness device consisted of ten emitters and was approximately 100 μm long by 1 μm wide [16]. The full width half maximum operating bandwidth of the laser diode emission was found to be approximately 2 nm. The Peltier cooler, on which the laser diode was mounted, was used to temperature tune the centre of the emission to the peak of the absorption in Nd:MgO:$LiNbO_3$ at 806 nm. To facilitate characterisation of the Nd:MgO:$LiNbO_3$ microchip laser coupling optics were used to collect pump light from the laser diode and re-focus it onto the chip. The optics

used were chosen to mimic, at the input surface of the device, the pump power density produced at the open facet of the laser diode array. The pumping configuration may be seen below.

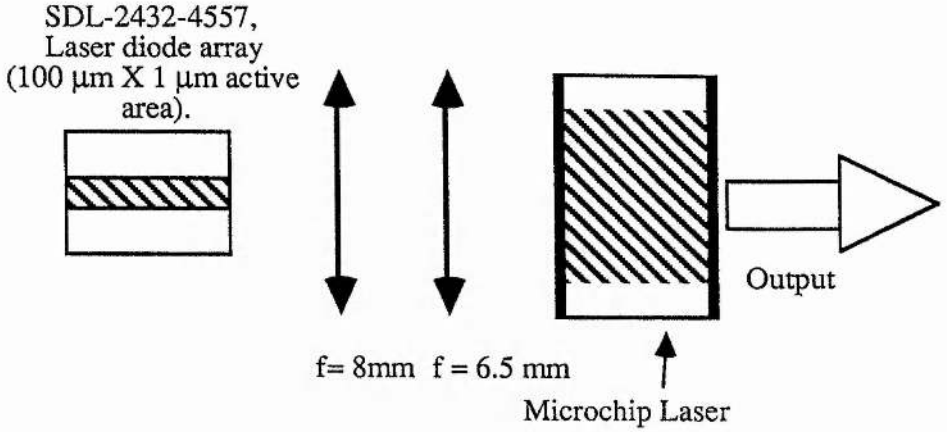

Figure 2.4.4: Coupling Optics Used and Longitudinal Pumping Scheme for Nd:MgO:$LiNbO_3$ Microchip Laser

Using an apertured, scanning photodiode the full width, half-maximum of the pump spot was found to be 110 μm in the plane parallel to the diode junction and 20 μm in the direction perpendicular to the junction. The pumping of the Nd:MgO:$LiNbO_3$ device was therefore very similar to positioning, with no intervening coupling optics, the microchip laser very close to the active area of the laser diode itself . Direct pumping of microchip lasers in this manner is called "butt"-coupling [4]. This phrase was first used by Zayhowski and co-workers [4]. The device was orientated such that the c-axis of the Nd:MgO:$LiNbO_3$ material was aligned to be parallel to the polarisation of the laser diode emission. This orientation ensured maximum absorption of the pump radiation [3,17-19]. The measured, peak absorption coefficient of the material (α=0.2 mm^{-1}) thus implied that in a double pass through the device approximately 25% of the incident pump power was absorbed in the gain material.

The input power/output power characteristics of the device may be seen in figure 2.4.4. The incident pump power threshold was 32 mW (8 mW absorbed power) and the slope efficiency was, in terms of incident power, 6.5 % (26 % in terms of absorbed power).

The maximum output power achieved was 13 mW. It must be noted that there was no difference in output power in taking the incident pump power from zero up to the maximum and the output power obtained in taking the incident pump power from the maximum used back down to zero.

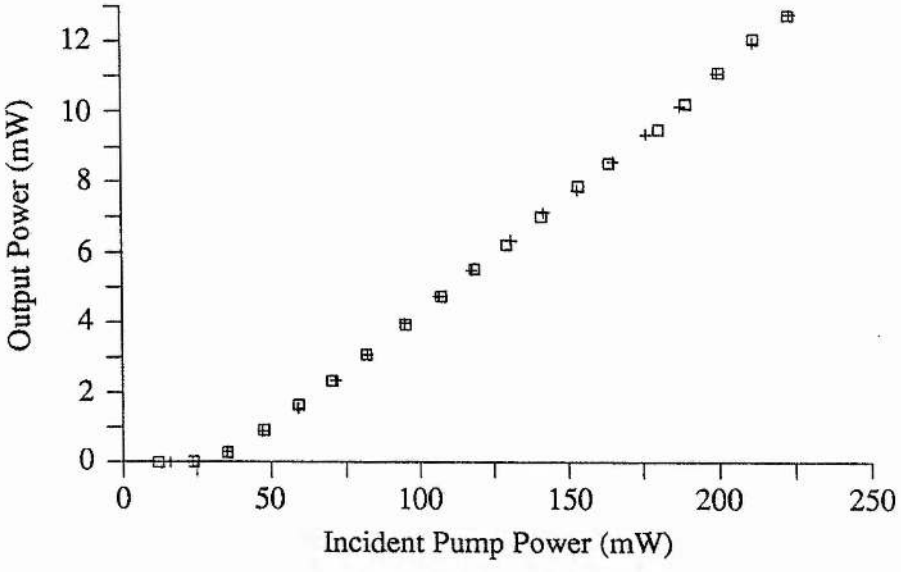

Figure 2.4.5: Power Characteristics of the Laser Diode Pumped Nd:MgO:LiNbO$_3$ Microchip Laser. Crosses-Input Power "Going Up", Squares-Input Power "Going Down" "

This lack of "hysteresis" between the two different output curves indicates the absence of any deleterious photorefractive effects [3,17-19]] in the Nd:MgO:LiNbO$_3$ material over the incident pump powers used. The output of the 1.084 μm emission was found to be polarised very strongly at all pump powers (>20:1) along the Nd:MgO:LiNbO$_3$ c-axis, or z-axis, in the direction of the highest optical gain [3,17-19]].

In addition to the 1.084 μm emission approximately 10 μW of non-phase-matched, green (542 nm) second harmonic emission was observed. The polarisation state of the generated green light was examined and found to be parallel to that of the 1.084 μm emission. A feasible route to phase match the second harmonic generation process in Nd:MgO:LiNbO$_3$ would be to exploit the birefringence of the material [3.5,6.14]]. This method was used by Fan et al. to produce phase matched second harmonic output [3]. Oscillation of the low gain 1.093 μm σ polarisation was forced by the insertion of a

Brewster angled plate within the cavity. The lasing fundamental and generated green were therefore in orthogonal polarisations and a type 1, non-critically phase matched, interaction [3] was used utilising temperature tuning of the host material birefringence . This method of phase matching however could not be used in monolithic Nd:MgO:$LiNbO_3$ devices where access to the cavity for polarisation selection is of course impossible.

The far-field intensity cross-section, as recorded by a CCD camera, of the 1.084 μm emission can be seen in figure 2.4.6.

Figure 2.4.6: Intensity Cross-section of 1.084 μm Output as seen in the Far-field for
(i) Upper Trace: 85 mW of Incident Pump Power
(ii) Lower Trace: 250 mW of Incident Pump Power

Both cross-sections have super-imposed upon them Gaussian fits (points). Clearly there is good agreement between the experimentally obtained intensity profile and that expected from theory. To examine the propagation characteristics of the 1.084 μm output beam the beam was focussed down using a single element lens of 100 mm focal length. An apertured, scanning photodiode was then used to locate and then measure the dimensions of the waist produced by the focussing lens. The divergence of the focussed beam was then calculated from the measured, far-field parameters of the focussed beam. At 85 mW and 250 mW of incident pump power there was to within the experimental uncertainties associated with the experimental technique very little difference between the divergence of the focussed output beam, as measured in the far-

field, and the divergence of the output beam that would be expected from the size of focussed waist. The corresponding M^2 value was found to be 1.1 +/. 9 %. The closely Gaussian intensity profile in the far-field (figure 2.4.6) and the near diffraction limited propagation characteristics of the output beam clearly pointed to the fact that the Nd:MgO:$LiNbO_3$ device, at all the incident pump powers used, was operating on a lowest order spatial mode.

With the knowledge that the output beam propagated in a near diffraction limited manner the far-field dimensions of the output beam were used to calculate the dimensions of the oscillating waist within the microresonator of the Nd:MgO:$LiNbO_3$ device. The oscillating beam waist was found to be dependent on the incident pump power as can be seen in figure 2.4.7. The size of the oscillating waist was found to be dependent on the inverse of the fourth root of the incident pump power as predicted by Zayhowski's model from Nd:YAG microchip lasers [12].

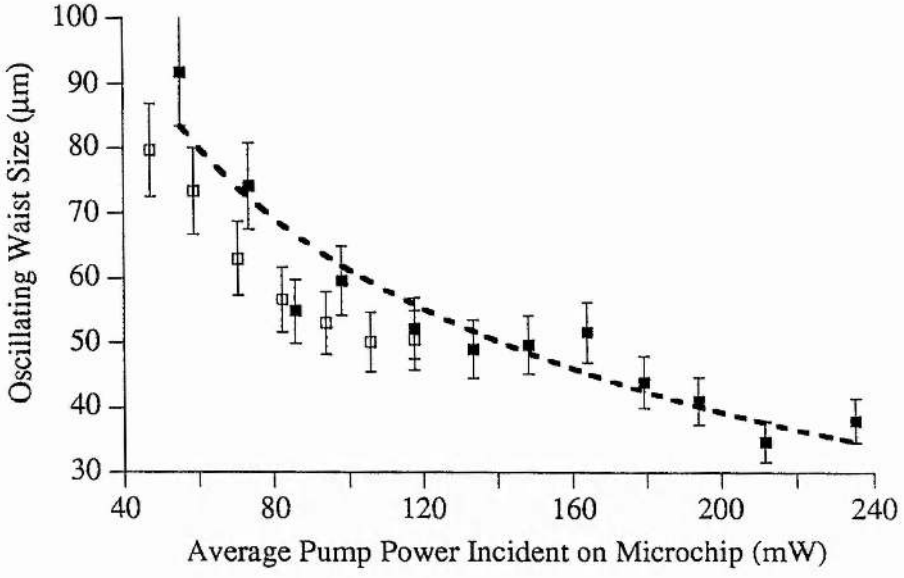

Figure 2.4.7: Fundamental Beam Waist Within Nd:MgO:$LiNbO_3$ Microchip Lasers for Filled Squares: Unchopped Pump Open Squares: Chopped Pump . Fit to Unchopped Pump Results is Power$^{-1/4}$

The proportionality, between the $P^{-1/4}$ factor and oscillating waist size, was linear though not direct and we attribute this to the existence of some effective initial curvature present in the device as outlined above. Another effect which has been

postulated by Harkness and Firth [21] as a possible stability mechanism in microchip lasers is gain guiding [21,22]. This is the effect by which the centre of a propagating Gaussian beam is amplified and the edges attenuated by a quadratically varying, radial gain profile so as to produce a fundamental mode size less than that expected by diffraction alone. Any gain related effects present will clearly have a much shorter time constant than any thermal guiding mechanisms. To ascertain the relative contributions, to cavity stability, of long and short time constants respectively the pump beam for the Nd:MgO:$LiNbO_3$ microchip laser was chopped with a 50% duty cycle at a 1kHz repetition rate. The oscillating fundamental waist size was then examined in this chopped pump beam regime. As can be seen in figure 2.4.7 the oscillating waist was found to be dependent on the average incident pump power.

If the definition of the transverse mode of operation was by short term, say gain related, effects alone then the size of the oscillating mode would be dependent on the peak pump intensity. However, as can be seen from the above figure, it is clear that, to within the experimental uncertainty associated with the measurements, the oscillating waist size is dependent on the average incident pump power. Therefore, in this relatively long pump pulse regime thermal effects are predominating over any shorter lived effects in defining the transverse mode of operation. This effect manifested itself in the peak pump power threshold of the device in the chopped regime. The device was pumped slightly away from the optimal area of the device. When the pump beam was chopped with a 50 % duty cycle at 1 kHz the peak pump power threshold of the Nd:MgO:$LiNbO_3$ device was found to have increased as can be seen in the figure 2.4.8 below.

It is worthwhile now summarising the results on the spatial properties of the output beam. It has been determined that

1. The 1.084 μm output of the device propagates in free space in a near diffraction limited manner with an experimentally determined M^2 [23] value of 1.1 +/. 9 %.

2. The far-field intensity cross-section, at all pump powers, has an approximately Gaussian shape.

3. The fundamental mode size within the resonator is linearly dependent on the inverse of the fourth root [12] of the incident pump power.

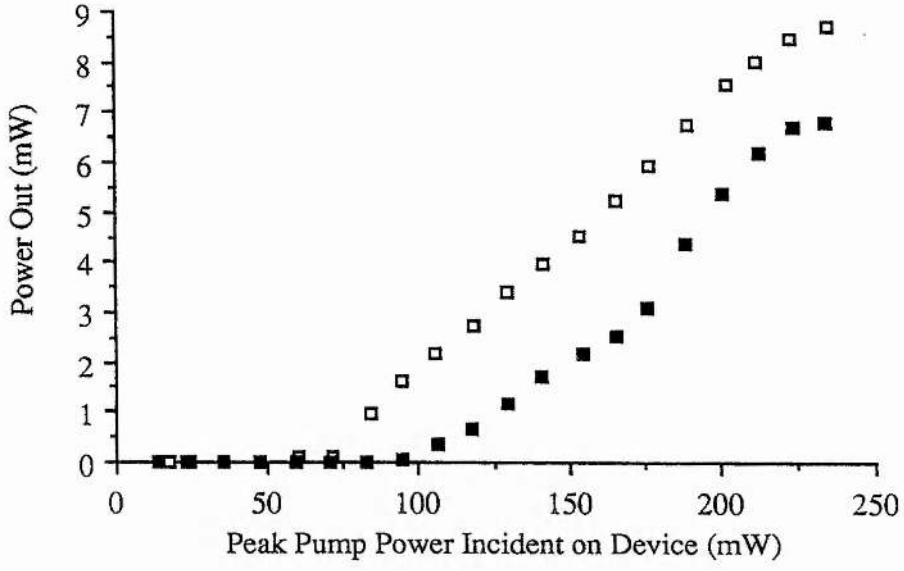

Figure 2.4.8: Peak Pump Power Threshold of Device With Chopped (Filled Squares) and Unchopped (Open Squares) Pump beam

4. In the definition of the transverse mode of operation relatively long time constant thermal effects are predominating over any shorter lived, gain related effects [12,21,22].

Pumping of the microchip laser in areas of non-ideal parallelism, such as the wedged area of the device, resulted in high threshold, poor spatial output characterised invariably by beams with a "comet like" appearance.

The above results, when one considers the positive dn/dT for $LiNbO_3$ and the relatively longitudinally uniform deposition of the incident pump power (α_{pump}=0.2 mm^{-1}) point strongly to the cavity stability mechanism in Nd:MgO:$LiNbO_3$ microchip lasers as being of the same, thermally induced, guided mode type as found in Nd:YAG microchip lasers [12].

2.4.2: Spectral Properties of Output and Electro-optical Tunability of Nd:MgO:$LiNbO_3$ Microchip Laser.

The output spectrum of the Nd:MgO:$LiNbO_3$ device was examined, using a scanning, plane parallel Fabry-Perot etalon and a 1 m "Monospek" spectrometer. Even just above threshold the device was operating on six adjacent longitudinal modes, separated by the free spectral range of the microchip cavity, centred around the peak of the high gain, π or c-polarised, 1.084 μm gain bandwidth [3,17-19]. The oscillating modes at P_{pump}= 130 mW (incident) can be seen in the transmission of the Fabry-Perot etalon in figure 2.4.9.

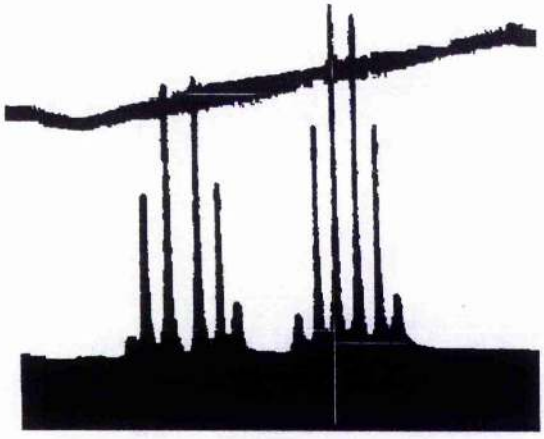

Figure 2.4.9: Oscillating Longitudinal Modes of Nd:MgO:$LiNbO_3$ Microchip Laser.

In the above figure the straight line above the mode groupings is the linear voltage applied to the piezo-driver required to scan the Fabry-Perot etalon. In the figure above two free spectral ranges of the etalon are shown. From the above figure the oscillating gain bandwidth of the device was measured to be 430 GHz. The oscillating axial modes were separated by 80 GHz thus implying an optical distance between the cavity mirrors of 680 μm.

Clearly the multi-longitudinal mode operation in this device will somewhat limit the utility of the device for many applications. However, an Nd:MgO:$LiNbO_3$ microchip laser could be made to be an inherently single-frequency device if the free spectral range of the cavity were reduced so as to ensure the existence of only one cavity mode

beneath the 1.084 μm gain bandwidth. This would entail reducing the thickness of the device to around one fifth of the value used here, i.e. down to approximately 140 μm. To compensate for the reduced absorption of the pump light, because of the much thinner crystal, greater concentrations of the active ion could be introduced into the material. An increase by a factor of five in the neodymium concentration to 1% would compensate for reduced thickness of the device. The upper state lifetime of the active ion would however be reduced by a factor of approximately two [24,25].

Tuning of a microchip laser, by mechanical means, has been accomplished by Zayhowski [26] and co-workers and the same investigator has reported on a composite material, laser diode pumped, electro-optically tunable microchip laser [27]. In the mechanically tuned device a piezo-electric transducer was used to compress the gain material thus modulating the optical length of the microchip cavity. Though this approach was plagued by strong mechanical resonances a tuning sensitivity of 0.3 $MHzV^{-1}$ was achieved over an applied voltage range of +/- 1kV. In the electro-optical tunable device reported on by Zayhowski a non-linear section of lithium tantalate [5,7] ($LiTaO_3$) was combined with an Nd:YAG gain section in a composite cavity configuration. This is in contrast to the single crystal, monolithic device reported on in this thesis where the optical gain and non-linear material are combined and are being exploited in the same material. The composite material device developed by Zayhowski exhibited, with an electrode spacing of approximately 1 mm, a tuning sensitivity of 12 $MHzV^{-1}$ and up to 30 GHz of frequency tuning was obtained without switching of the polarisation state of operation [4,27]. The acentric space group, stoichiometric material neodymium aluminium borate (NAB) [30] was also investigated as a candidate for a monolithic, electro-optically tunable microchip laser by Winzer et al.. Despite the application however of an electric field strength of 4.1 kV across a 1.2 mm electrode separation no electro-optically induced frequency shift could be detected in the laser output with their monochromator based set-up. Winzer and his co-workers attributed this to the relatively small magnitude of the electro-optic coefficient (0.6 pm V^{-1}) being exploited in the material and the relatively insensitivity of their experimental set-up

[29]. Tuning of a discrete output coupler, hybrid microchip laser has been accomplished by Zhou and Ferguson [30]. In their 1.32 μm laser-diode-pumped device fine translation of a discrete output coupler, mounted on a piezo-electric actuator was used to modulate the optical length of the cavity. Fifty eight GHz of continuous tuning was observed without polarisation switching [27,30].

In order to monitor the electro-optically induced tunability of an Nd:MgO:$LiNbO_3$ microchip laser a heterodyne experiment [31] between two laser diode array pumped Nd:MgO:$LiNbO_3$ devices was performed. One device was electrically connected to a voltage source providing a 120V peak to peak "sawtooth" at 10 Hz. As shown in section 2.2 this voltage was applied, via gold electrodes, transversely across the cavity axis to access the r_{33} non-linear coefficient in $LiNbO_3$. The remaining control device was left free-running with no applied voltage. Super imposition, to within the bandwidth of the detector (2 GHz), of one cavity mode from each device was achieved by modulation of the pump power applied to each device [32,33].

The frequency sweep of the electrically connected device was found to be 280 MHz. This frequency change corresponds to a tuning sensitivity of 8.9 $MHzV^{-1}mm$ when the electrode separation of 3.78 mm is taken into account, . Additional experiments using a 1 m monochromator indicated that this tuning rate was maintained at higher voltages with 1.7 GHz of tuning having been obtained [34,35]. The frequency sweep of the electrically connected device can be seen in the spectrum analyser printout below. The slight discrepancy between the theoretically calculated tuning sensitivity and that obtained in the heterodyning experiment may be perhaps due to edge effects between the gold electrodes lowering the electric field strength within parts of the crystal.

The passive stability of these devices is however an issue. Although less prone to disturbance than external mirror cavities containing air, pump power instability, ambient temperature fluctuations and positional/alignment instability may result in optical thickness changes within the device and thus frequency changes in the device output.

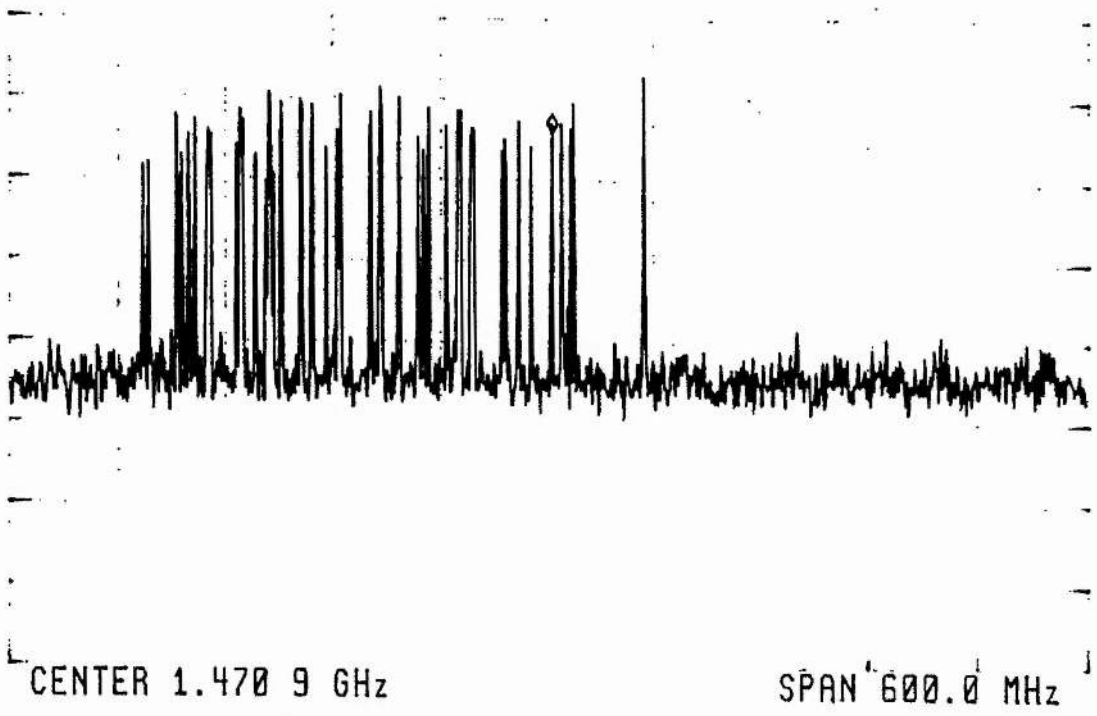

Figure 2.4.10: Frequency Sweep of the Electrically Connected Nd:MgO:$LiNbO_3$ Microchip Laser

Consider again equation 2.8

$$\frac{\Delta\upsilon}{\upsilon} = \frac{\Delta n}{n} \qquad \text{Eqn. 2.14}$$

Rearranging the above we find that

$$\Delta\upsilon = \frac{c\Delta n}{\lambda n} \qquad \text{Eqn. 2.15}$$

Where c is the speed of light in vacuo, n is the extraordinary refractive index, λ is the free space wavelength of operation and Δn_e is a slight change in the extraordinary refractive index. Substituting in the appropriate values we find that

$$\Delta\upsilon = 1.26 \times 10^{14}\, \Delta n_e \qquad \text{Eqn. 2.16}$$

In addition to any electric-field-induced change in the extraordinary refractive index of the material, ambient temperature fluctuations may alter the refractive index of the material and thus the frequency of operation. The rate of change of the extraordinary refractive index with temperature for $LiNbO_3$ is $1 \times 10^{-6}\ K^{-1}$ [14]. Assuming that

heating of the device would not change the physical length of the device this value would imply, using equation 2.15, a temperature sensitivity of 126 MHz K^{-1}. Clearly to avoid such long term drift in the frequency of operation of the device temperature stability of the device environment would be of importance. Similarly stability in the intensity of the pump source should be maximised for minimal fluctuations in the frequency of operation [32,33].

The voltage sawtooth applied to the electrically connected device was removed and the two laser diode pumped devices left free-running. Over a ten second interval (the same time interval as the measurement of frequency sweep) the passive frequency drift between the two devices was found to be 22.4 MHz. Taking this drift into account the tuning sensitivity of the Nd:MgO:$LiNbO_3$ microchip laser can be given as 8.9 $MHzV^{-1}mm$ +/- 8%. The frequency drift of the two devices relative to one another can be seen in the spectrum analyser printout below.

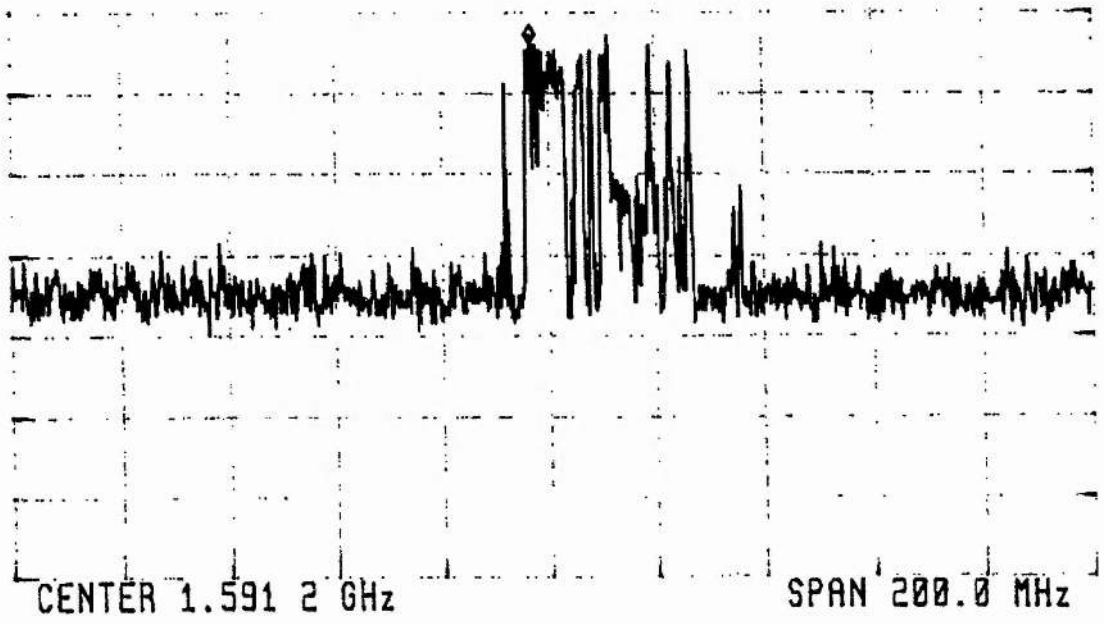

Figure 2.4.11: Passive Drift of Nd:MgO:$LiNbO_3$ Microchip Lasers in Heterodyne Experiment

2.5: Conclusions and Summary

A laser diode array pumped, electro-optically tunable microchip laser has been demonstrated and characterised.

The device operated in the lowest order spatial mode at all pump powers up to a maximum output power of 13 mW.

The definition of the transverse mode of operation was determined to be by thermal waveguiding within the device induced by the absorbed pump power. Electro-optic tuning of the oscillating cavity modes was achieved at a sensitivity of 8.9 +/. 8% MHz V^{-1} mm.

References

[1] J. M. Senior, "Optical Fiber Communications", Second Edition, Prentice Hall International Series in Optoelectronics, p. 702

[2] P. A. Schulz, Lincoln Laboratory Journal, **3**, No. 3, p. 463, (1990)

[3] T. Y. Fan, A. Cordova-Plaza, M. J. F., Digonnet, R. L. Byer and H. J. Shaw, J., Opt., Soc. Am., B, **3**, No. 1, p. 140 (1986)

[4] J. J. Zayhowski and A. Mooradian, Opt. Lett., **14**, p. 618, (1989)

[5] J. F. Nye, "Physical Properties of Crystals", Oxford University Press, Vol. 7, 1976, p. 235-275

[6] A. Yariv, "Quantum Electronics", Wiley, Third Edition, p.298-307

[7] I. P. Kaminow and E. H. Turner, Appl. Opt., **5**, No.10, p. 1612, (1966)

[8] A. Siegman, "Lasers", University Science Books, 1986, p. 588-589

[9] A. Yariv, "Quantum Electronics", Wiley, Third Edition, p.108

[10] E. Snitzer, J., Opt., Soc. Am., B, **51**, No. 5, p. 491, (1961)

[11] E. Snitzer and H. Osterberg, J., Opt., Soc. Am., B, **51**, No. 5, p. 499, (1961)

[12] J. J. Zayhowski, in O. S. A. Proceedings on Advanced Solid-State Lasers, H.P. Jenssen and G. Dube, eds., Vol. 13, (Optical Society of America, Washington D. C.)

[13] H. Kogelnik, Appl. Opt., **4**, No. 12, p. 1562, (1965)

[14] M. V. Hobden and J. Warner, Phys. Lett., **22**, no, 3, p. 243, (1966)

[15] W. H. Steel, "Interferometry", Cambridge University Press, 1967, p. 10,

[16] Spectra Diode Labs, San Jose, Ca., U.S.A., Laser Diode Operator's Manual, p. 17-24

[17] T. Y. Fan, A. Cordova-Plaza, M. J. F., Digonnet, R. L. Byer and H. J. Shaw, Opt. Lett., **13**, No.3, p. 209, (1988)

[18] S. J. Field, D. C. Hanna, D. P. Shepherd, A. C. Tropper, P. J. Chandler, P. D. Townsend and L. Zhang, Opt. Lett., **16**, No. 7, p. 481, (1991)

[19] A. Cordova-Plaza, M. J. F., Digonnet and H. J. Shaw, I.E.E.E. J. of Quant. Elect., **QE-23**, No. 2, p. 262, (1987)

[20] M. V. Hobden, J. of Appl. Phys., **38**, No. 11, p. 4365, (1965)

[21] G. K. Harkness and W. J. Firth, J. of Mod. Opt., **39**, No. 10, p. 2000, (1992)

[22] W.J. Firth, Opt. Comm., **22**, No.2, p. 226, (1977)

[23] A. Siegman, "Lasers", University Science Books, 1986, p. 867

[24] L. I. Ivleva, A. A. Kaminskii, Y. S. Kuz'minov and V. N. Shpakov, Sov. Phys Dokl., **13**, p. 1185, (1969)

[25] L. P. Kaminow and L. W. Stultz, I.E.E.E. J. of Quant. Elect., **QE-11**, p. 306, (1975)

[26] J. J. Zay howski, A. Mooradian, Opt. Lett., **14**, No.,1, (1989)

[27] J. J. Zayhowski, P. A. Schulz and S. R. Henion, Paper CThR4, Conference on Lasers and Electro-optics, (CLEO), 1993, Technical Digest Series, Vol. 11, Optical Society of America, Washington D. C., U.S.A., p. 484

[28] J.-P. Goedeburger, S. Gurib and H. Porte, I.E.E.E. J. of Quant. Elect., **QE-28**, No. 6, p. 1414, (1992)

[29] G. Winzer, P. G. Moeckel and W. W. Kruehler, I.E.E.E. J. of Quant. Elect., **QE-14**, No. 11, p. 840, (1978)

[30] F. Zhou and A. I. Ferguson, Electron. Lett., **26**, No. 7, p. 490, (1990)

[31] A. Yariv, "Quantum Electronics", Wiley, Third Edition, p.352, 361

[32] J. A. Keszenheimer, E. J. Balboni and J, J, Zayhowski, Opt. Lett., **17**, No. 9, p. 649, (1992)

[33] T. Taira, A Mukai, Y. Nozawa and T Kobayashi, Opt. Lett., **16**, No. 24, p. 1955, (1991)

[34] N. MacKinnon, C. J. Norrie and B. D. Sinclair, Paper CThS12, Conference on Lasers and Electro-optics, (CLEO), 1993, Technical Digest Series, Vol. 11, Optical Society of America, Washington D. C., U.S.A., p. 496

[35] N. MacKinnon, C. J. Norrie and B. D. Sinclair, J. Opt., Soc., Am., B, **11**, no. 3, p. 1, (1994)

Chapter 3: Cavity Stability Mechanisms and Operating Characteristics of a Lithium Neodymium Tetraphosphate, $LiNdP_4O_{12}$ (LNP), Microchip Laser Excited by a Ti:sapphire Laser.

Introduction

In this chapter we shall consider the pump power induced cavity stability mechanisms in a Ti:sapphire laser pumped, lithium neodymium tetraphosphate, $LiNdP_4O_{12}$, (hereafter LNP), microchip laser. Firstly, the previously published spectroscopic and thermal properties of the solid-state gain material LNP are discussed. Particular consideration is given to the thermal properties of the gain material and how these properties preclude the type of transverse mode definition described in the previous chapter. Secondly, the Ti:sapphire pumped LNP device is characterised in the terms of

i). Power characteristics

ii). Output beam quality as a function of pump power

iii). Output beam divergence as a function of pump power

and iv). Spectral characteristics of the output.

The LNP microchip laser is then examined using a Fizeau interferometer in order to map out the pump power induced optical path length changes within the device. The interferometrically observed optical path length changes are then compared with the observed pump power dependent beam divergence in terms of a simple resonator stability model. The observed optical thickness changes are then broken down into their constituent components so as to determine the prime factors contributing to cavity stability. Finally the contribution of short time constant, gain related effects to the LNP cavity stability mechanisms are considered.

3.1 Properties and Applications of Stoichiometric Laser Gain Materials

Lithium neodymium tetraphosphate is a solid-state gain material of the class known as the stoichiometrics[1-3,5-9,11,14,15,21,22]. Stoichiometric laser gain media are distinct from other solid-state gain media in that the active ion (in the main cases presented here the Nd^{3+} ion) is a chemical constituent of the material as opposed to being an impurity, or dopant, which is forced into the crystal matrix of a host material [1,2,4]. Consequently, the concentration of the active ion in stoichiometric materials is much higher than in doped materials. In stoichiometric laser media the active ion concentration ranges from 20 to 30 times that in 1 % doped Nd:YAG. Despite this high Nd^{3+} ion concentration the upper state lifetime of the active ion is reduced, in most stoichiometrics, by only a factor of approximately two as compared to the Nd^{3+} ion in YAG [4]. The reason for the absence of marked fluorescence quenching is as yet unclear but is thought to originate in the exact regularity of the Nd^{3+} ion spacing which is imposed by the stoichiometry of the gain material of which the Nd^{3+} ion is a chemical component [1,2].

The first stoichiometric laser material considered was neodymium pentaphosphate NdP_5O_{14} (hereafter NPP) and was examined by Danielmeyer and Weber [2]. NPP was also the first stoichiometric laser material to operate at room temperature. Following NPP a whole host of stoichiometric laser materials were to be developed in the nineteen seventies the most promising sub-group being the neodymium phosphates [1,2].

The table below summarises the chemical formulae, acronym and basic lasing characteristics of the principal transitions in the most common stoichiometric media developed to date.

The term "cube" laser was coined by Huber [1] to describe a very short piece of gain material (typically less than 1 mm in length) with dielectric coatings deposited directly onto near parallel, polished gain material surfaces. These prototype microchip lasers

utilised newly developed stoichiometric gain media as the laser crystal. The first such "cube" laser was fabricated from NPP and examined by Winzer [6].

Material	Acronym	N_0	λ_{lasing}	$\sigma_{em.}$	$\tau_{fluor.}$
NdP_5O_{14}	NPP	3.96	1.0512	2	115
$LiNdP_4O_{12}$	LNP	4.37	1.0477	3.23	120
$NaNdP_4O_{12}$	NNP	4.24	1.051	2.1	110
$KNdP_4O_{12}$	KNP	4.08	1.0515	1.5	100
$NdAl_3(BO_3)_4$	NAB	5.43	1.0635	8	19
$Y_3Al_5O_{12}:Nd^{3+}$ (1% Nd Conc.)	Nd:YAG	0.138	1.0641	3.47	230

Figure 3.1.1: Table of Lasing Properties of Principal Stoichiometric Gain Media in Comparison with Nd:YAG (after [3])

N_0 is the Active Ion Concentration and has Units x 10^{21} cm^{-3}
λ_{lasing} is the Principal Lasing Wavelength and is in Units μm
$\sigma_{em.}$ is the Stimulated Emission Cross-section of the Principal Lasing Transition and has Units x 10^{-19} cm^2
$\tau_{fluor.}$ is the Upper State Lifetime and is in Units of μs

Using an argon ion laser as the pump source for the device a maximum of 19 mW of 1 μm radiation was obtained from a 460 μm thick NPP device for 300 mW of incident pump light. However, the device operated on a number of axial and transverse modes [6]. Similar multi-mode operation in both the spatial and spectral regimes of operation was observed by Winzer in a neodymium aluminium borate (NAB) "cube" or microchip laser [7]. In this gain material thermal effects, which were attributed to the poor quality of the material, seriously inhibited the operation of the device with only quasi-C.W. pumping being possible. In addition to thermal problems affecting power performance a highly complex transverse mode of operation was observed [7]. LNP with its excellent gain properties [3,8] and reasonable growth characteristics attracted similar attention. LNP was first examined in a "cube" format by Kruehler et al [9]. However, only 1 mW

of multi-mode 1 μm output was observed for 30 mW of absorbed pump power using an argon ion laser pump source.

The advent of relatively inexpensive, high power, high brightness AlGaAs diode lasers operating in the spectral regime around 0.8 μm [10] combined with the ever present quest for increased miniaturisation gave new impetus to the examination of stoichiometrics as laser gain media. Some of the more recent work on microchip lasers utilising stoichiometric lasers was performed by Dixon et al [11]. Dixon and his co-workers produced what they termed "close-coupled" LNP microchip lasers. The close-coupled microchip lasers consisted simply of an active device placed over the open facet of a half-Watt laser diode array thus obviating the need for any intervening coupling optics. The close coupled device produced up to 60 mW of fundamental spatial mode radiation while operating on two axial modes [11]. Despite having an initial cavity configuration nominally on the boundary of cavity stability and also a pump beam with very poor spatial properties the close-coupled device examined by Dixon and his co-workers operated with a circular, near-diffraction limited output beam. This is in contrast to the behaviour of the original "cube" lasers outlined above perhaps because of improved material quality but also perhaps due to the more efficient pumping possible with 800 nm laser diodes [10,11]. The quantum efficiency of the lasing process improves from 50 % with argon ion laser pumping to 76 % with 800 nm pumping. Clearly a pump power induced cavity stability mechanism , associated with the new improved pumping regime, was involved in the refinement of the resonator characteristics of the close-coupled LNP device. As we have seen in chapter 2 the cavity stability in Nd:MgO:$LiNbO_3$ microchip lasers was induced thermally by the absorbed pump radiation producing a confining duct for the oscillating radiation. We shall see however below that in LNP the cavity stability mechanism, although induced by the incident pump power, is by somewhat different means.

3.2 Thermal and Spectroscopic Properties of Lithium Neodymium Tetraphosphate (LNP)

Thermal Properties of LNP

The thermal properties of a solid-state gain material have considerable impact on the properties and performance of a solid-state laser [12-14]. Optical path length changes (where optical path length is the product of physical separation and intervening refractive index) caused by deposition of excess heat from the incident pump power can degrade the spatial quality of the output beam and lower the maximum power obtainable from a solid-state laser. In a microchip laser, as we have seen in the previous chapter, such heating effects can help to define the spatial mode of operation. The thermal properties of LNP have been measured by Nakano [15] and are tabulated below.

Crystallographic Axes	a	b	c
Coefficients of Thermal Expansion (x 10^{-6} K^{-1})	7	13	9
dn/dT (x 10^{-6} K^{-1})	-1	-1	-4

Figure 3.2.1: Thermal Properties of LNP

The values of dn/dT and α were found to be dependent along which of the crystal axes they were measured. Nakano proposed that this anisotropy in the thermal properties of LNP originated in the anisotropy in the crystal structure itself [5,15].

The values for thermal expansion are comparable, along the a and c-axis, with those of the host material YAG while, more strikingly, the dn/dT for the material is negative. This negative dn/dT in LNP clearly precludes the existence of a confining, thermally induced, guide or duct [16,17] within the microchip laser as described in chapter 2. However, at this point it is worthwhile to note that during heating of the LNP material a positive optical path length change is always observed. The coefficients of thermal expansion are large enough such that the increase in physical length of the heated

material offsets the slight drop in the refractive index of the material to produce a net positive change in the optical thickness of the material [15].

Spectroscopic Properties of LNP Near 0.8 μm and 1.05 μm

The optical absorption near 0.8 μm and the fluorescence characteristics near 1.05 μm of LNP have been measured by Otsuka et al. [8]. The absorption spectrum of an a-cut platelet of LNP was measured using a spectrometer. The peak absorption cross-section was found to occur for pump radiation polarised in a direction parallel to the crystal LNP c-axis and was measured to be $\sigma_{abs.}=1.25 \times 10^{-19}$ cm^2 at a wavelength of $\lambda_{pump}=800.9$ nm. The absorption spectrum for c-polarised pump radiation may be seen below.

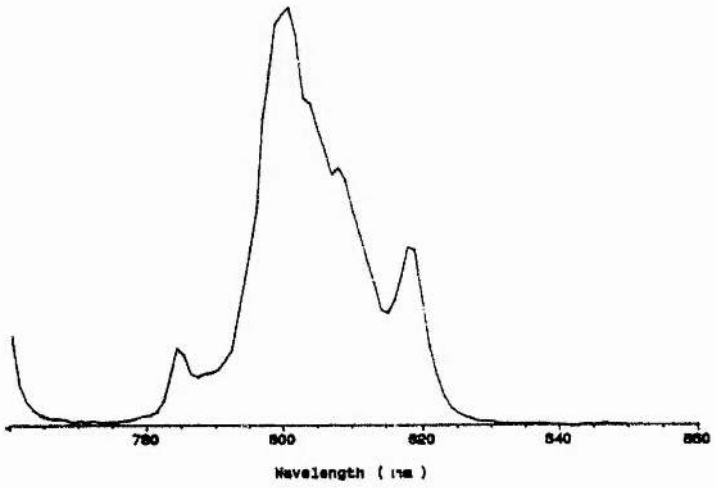

Figure 3.2.2: c-polarised Absorption Spectrum for LNP in the Vicinity of 0.8 μm (after [8])

The peak absorption cross-section in LNP is approximately the same as the peak absorption cross-section for Nd^{3+} in YAG [4,18]. Since in LNP the active ion concentration is 30 times that of 1 % Nd:YAG the approximately equal absorption cross-sections imply that the absorption of the pump radiation in LNP should be approximately 30 times the pump absorption in Nd:YAG. Otsuka and his co-workers measured in LNP an absorption coefficient of $\alpha=26$ mm^{-1} using a krypton ion laser pump source. This corresponds to a 1/e folding distance of 40 μm for the incident pump

power. Clearly then in an LNP microchip laser deposition of the pump power, of appropriate wavelength, would occur within a very short distance of the input surface of the device. In fact, absorption of the pump radiation would be virtually complete within 90 μm of the LNP material.

Emission Cross-Sections and Fluorescence Spectra of LNP

Otsuka and his co-workers found that the laser emission of their LNP lasers was always very strongly polarised along the c-axis of the gain material. Therefore, the measurements of the emission cross-sections and linewidths were made for the **E** vector polarised parallel to the crystal c-axis. The main fluorescence bands in LNP occur in the vicinity of 1.05 μm. This set of wavelengths of emission corresponds to transition from the $^4F_{3/2}$ manifold to the $^4I_{11/2}$ manifold in neodymium. The presence of two closely spaced levels in the $^4F_{3/2}$ manifold and six closely spaced levels in the lower manifold [8] gives rise to a number of emission lines around 1.05 μm. The fluorescence emission of LNP, polarised in the direction parallel to the LNP crystal c-axis is shown below.

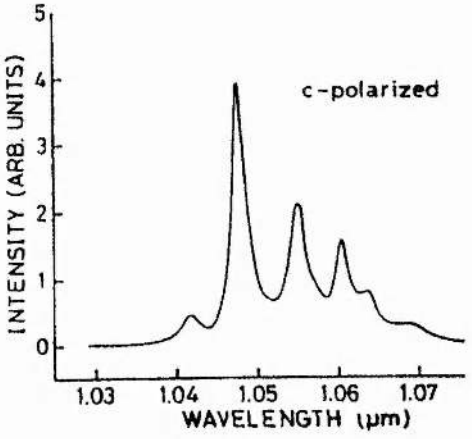

Figure 3.2.3: c-Polarised Fluorescence Spectrum in LNP (after [8])

The peak emission cross-section corresponding to the 1.047 μm transition was determined to be 5.1 x 10^{-19} cm^2. This value compares with 3.47 x 10^{-19} cm^2 for the principal transition in Nd:YAG. The fluorescence lifetime of the $^4F_{3/2}$ manifold was measured by Otsuka and his co-workers to be τ_f=120 μs [8]. The fluorescence spectra

for the electric field vector parallel to the crystal a and b axes are of similar form as that shown above but of much lower intensity. For fluorescence with **E** parallel to the crystal b axis the emission cross section at 1.05 μm is less than one quarter of that for the c-axis polarised fluorescence [8].

A useful comparison for solid-state gain materials is to consider the product of upper state lifetime and stimulated emission cross-section for the principal transition. This $\sigma_{em}.\tau_f$ product is simply an expression of how efficient the stimulated emission process is for a particular transition. The $\sigma_{em}.\tau_f$ product for LNP is set out below with the similar parameter for other common solid-state gain materials with emission near 1.05 μm.

Gain Material	**Class**	$\sigma_{em}.\tau_{fluor.}$ (x 10^{-23} cm^{-2} s)
Nd:YAG (1 % Nd^{3+})	Doped	8.0
Nd:YVO_4 [19] (1 % Nd^{3+})	Doped	9.0
Nd:YVO_4 [19] (2 % Nd^{3+})	Doped	5.0
Nd:S-VAP [20] (1 % Nd^{3+})	Doped	11.5
NAB	Stoichiometric	1.52
NPP	Stoichiometric	2.3
LNP	Stoichiometric	3.88

Figure 3.2.4: $\sigma_{em}\tau_f$ Product for LNP and Other Common Gain Materials

Therefore with an efficient four-level lasing regime for 1.05 μm in LNP coupled with such efficient absorption of the pump radiation LNP featured as a prime candidate for microchip laser applications and other ultra-compact microlaser configurations.

Section 3.3: Performance Characteristics of an LNP Microchip Laser Excited by a Ti:sapphire Laser.

Active Device Structure and Optical Parallelism

A series of LNP microchip lasers were fabricated for us by Virgo Optics . The characteristics of the specified device may be seen in the figure below.

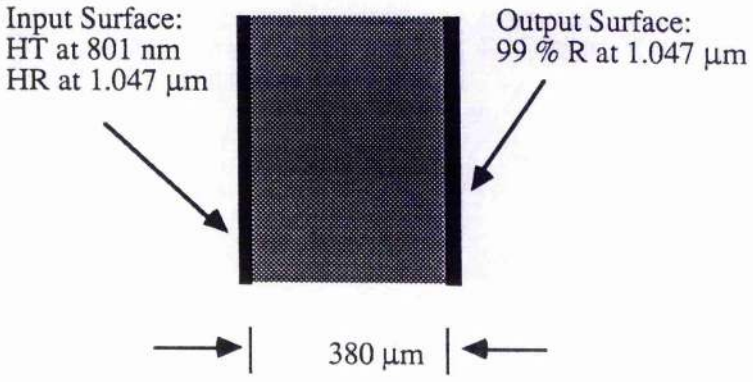

Figure 3.3.1: Coatings and Dimensions of LNP Microchip Laser

In the above diagram the surfaces designated as being highly reflecting (HR) were specified as being greater than 99.8% reflective. Correspondingly the surfaces designated as being highly transmitting (HT) were specified as being less than 10% reflective at the desired wavelength. Ideally, in order to maximise the area of the device aperture which may be utilised and to optimise the initial conditions for any pump power induced cavity mechanisms the mirrors deposited on the crystal surfaces of the microchip laser should be separated by equal optical thicknesses at all points. The active device was placed in a HeNe based Fizeau interferometer so as to produce fringes of equal optical thickness (or internal fringes) between the microchip laser mirrors. The configuration of the Fizeau interferometer may be seen in figure 2.4.1. The internal fringes present in the LNP microchip laser are shown below. The finished device, as shown in figure 3.3.2, was quite far from this ideal with what can be viewed as an effective wedge formed between the mirrored surfaces of the device. However, in the lower part of the crystal there is an area of reasonable local optical parallelism indicated in the above figure by a broad, bright fringe at the bottom of the crystal. Marked differences in the performance of the device were observed when the device was excited in areas of inferior parallelism. Typically the threshold of the device gradually increased

as the device was pumped in areas of increased mirror non-parallelism and the spatial quality of the output beam degraded noticeably [21,22].

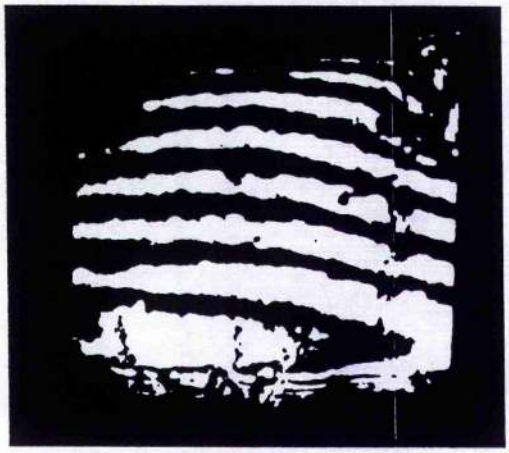

Figure 3.3.2: Equal Optical Thickness Fringes (Internal Fringes) Formed Between Microchip Laser Mirrors.. The Device Shown is 3 mm from Top to Bottom

Similar observations were made by Zayhowski in his studies on Nd:YAG microchip lasers [28]. The figure below shows a schematic representation of the output beam as observed in the LNP device when pumped in the upper third of the device aperture, away from the optimal area. The quality of the output beam from the best area in the device will be discussed in detail in the next sub-section of this chapter (**Output Beam Quality**).

Figure 3.3.3: Output Beam from Poor Area of Device

In this chapter we shall restrict our study of pump power induced cavity stability to the region of the device corresponding to the area of best parallelism between the cavity mirrors. This area yielded, as one would intuitively expect, the best lasing performance.

Pumping Configuration and Output Power Performance

The excitation configuration for the LNP device can be seen below.

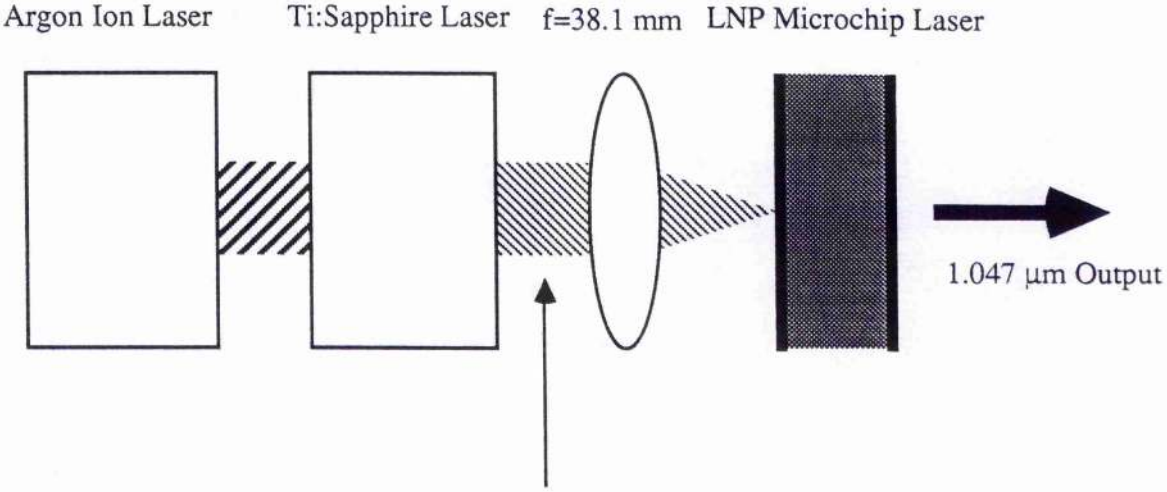

Figure 3.3.4: Pumping Scheme for Excitation of LNP Microchip Laser by a Ti:sapphire Laser

The standing wave Ti:sapphire pump laser was capable of producing up to half a Watt of 800 nm radiation with a specified linewidth of approximately 2 GHz. The pump laser was tuned to the absorption peak of LNP at λ_{pump}=800.9 nm. The absorption coefficient of this pump radiation in the correctly orientated LNP microchip laser was measured to be α=26 mm^{-1}. The pump light was focussed down using a 38 mm focal length lens to a measured $1/e^2$ half width of ω_{pump}=17 +/- 5 μm. An example of the performance of the Ti:sapphire pumped LNP microchip laser can be seen below in figure 3.3.5. With a pump power threshold of 12 mW and a slope efficiency of 45% the LNP microchip laser constitutes an efficient source of coherent laser radiation. Up to 20 mW of single frequency output was observed. Above this output power an adjacent longitudinal mode driven by the 1.055 μm transition [8,9,11] was excited in preference to longitudinal cavity modes under the principal gain bandwidth at 1.047 μm. Detuning of the pump laser away from peak absorption, and thus extension of the gain length within the material, led to decreased maximum single frequency output power although the overall

output power did not show such a strong dependence on the pump wavelength. The effect of gain length compression [23,24] on the mitigation of spatial hole-burning in a microchip laser and its interaction with the longitudinal mode spacing will be considered in detail in the next chapter.

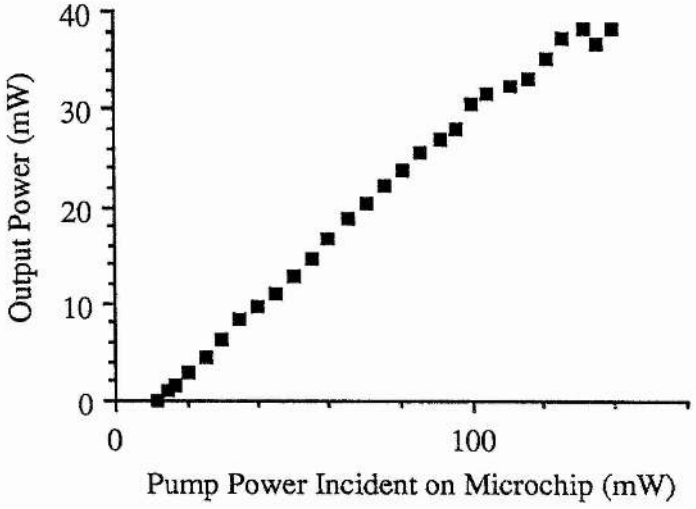

Figure 3.3.5: Power Performance of Ti:sapphire Laser Pumped LNP Microchip Laser

The output of the LNP microchip laser was very strongly polarised along the c-axis of the crystal [8,9,11].

Output Beam Quality

The output beam from the device was examined in the far-field and found to be circularly symmetric and Gaussian in cross-section at all pump powers. The far-field intensity cross-section of the output can be seen below in figure 3.3.6.

In order to verify that the output beam was indeed diffraction limited the output beam was passed through a single element lens of focal length f=200 mm and the waist produced by this lens was measured using an apertured photodiode. At 79 mW and 110 mW of incident pump power there was, within the experimental error associated with the procedure, no discrepancy between the divergence of the focussed output beam, as measured in the far-field, and that expected from the measured waist of the focussed

output beam. This experiment confirmed the near diffraction limited nature of the output beam and yielded a value of M^2=1.05 +/- 9 % for the output beam [25].

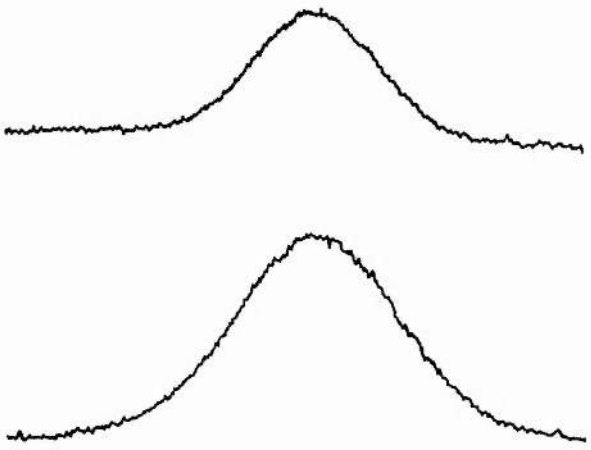

Figure 3.3.6: Far-field Intensity Cross-section of LNP Microchip Laser Output for (Top) 25 mW of Incident Pump Power (Bottom) 153 mW of Incident Pump Power

With the knowledge that the output beam of the device did indeed behave in a near diffraction limited manner the far-field properties of the beam were used to work back to a value for the fundamental beam waist within the microresonator of the LNP microchip laser. The fundamental mode size within the device was found to be dependent on the incident pump power as may be seen below in figure 3.3.7. Clearly from figure 3.3.7 it is evident that pump power deposition is inducing a change in the cavity geometry of the LNP microchip laser resonator. To investigate this dynamic cavity geometry the LNP microchip laser was placed in a Fizeau interferometer in order to map out the optical thickness changes between the cavity mirrors.

Section 3.4: Input Surface Deformation and Gaussian Eigenmode Confinement in a Ti:sapphire Laser Pumped LNP Microchip Laser.

In this section a simple model for pump power induced cavity stability in LNP microchip lasers is introduced. This model is then applied to observed optical path

length changes within the device and to externally observed surface deformation to examine the mechanism defining the spatial mode of operation.

As has been noted above the absorption associated with stoichiometric laser gain media is very strong [1,3,5-9,11,21,22] with almost total pump absorption within approximately 100 μm of entering the material. In the light of this very strong thermal

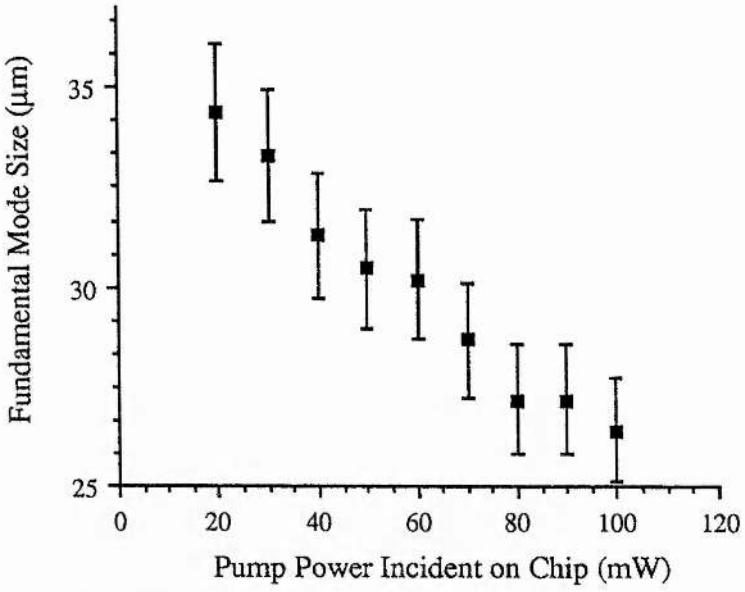

Figure 3.3.7: Pump Power Dependence of Fundamental Mode Size Within the LNP Microchip Laser.

loading on the input surface we shall postulate the following simple model of pump power induced cavity modification. We propose that the pump power heating effects can distort the input surface of the microchip such that the microresonator is modified from being nominally plano/plano to being approximately half-symmetric [26]. The figure 3.4.1 below shows the proposed pump power induced modification.

The LNP microchip laser was inserted into a Fizeau interferometer so as to examine and map out the optical path length changes between the device mirrors. Figure 2.4.1 outlines the interferometer used. These internal fringes of equal optical thickness represent the optical path length "seen" by the oscillating radiation. Therefore any

change in these internal fringes represented the sum of contributions from pumped surface and output surface deformation and any changes in refractive index in between.

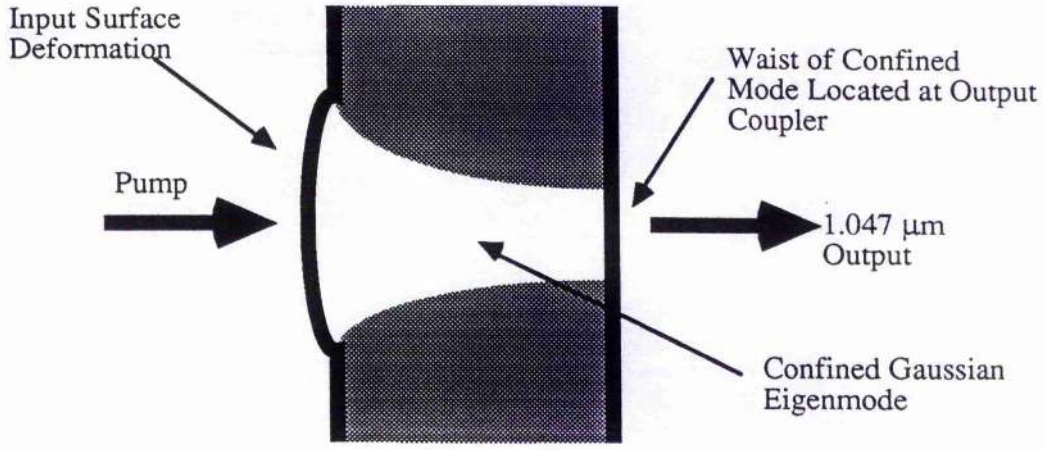

Figure 3.4.1: Approximate Half-Symmetric Modification of Microchip Laser Cavity

The focal length of the imaging lens and its position relative to the LNP microchip laser was chosen so as to magnify the image of the chip on to the CCD array such that one pixel element on the array was equivalent to 3 μm, spatially, across the aperture of the device.

In the view of our approximation of a half-symmetric model for the microchip laser resonator the internal optical path length changes were quantified and at first were assumed to be due to input surface deformation only. The refractive index of the LNP was assumed to have a constant value throughout and it was assumed that no contribution in optical path length change was due to any output coupler surface deformation.

The radius of curvature of a diffraction limited 1.047 μm beam at the input surface of the device, was calculated from the size of the fundamental waist as implied by the far-field divergence (see figure 3.3.6). (In accordance with the half-symmetric resonator model adopted the mode waist was assumed to be at the surface of the output coupler). The radius of curvature of the oscillating mode, at the pumped surface, was then

compared directly with the effective radius of curvature observed in the internal fringe structure. The effective radius of curvature observed in the internal fringe structure was measured over the calculated dimensions of the transverse mode at the input surface. The correspondence between these two values can be seen in the figure below.

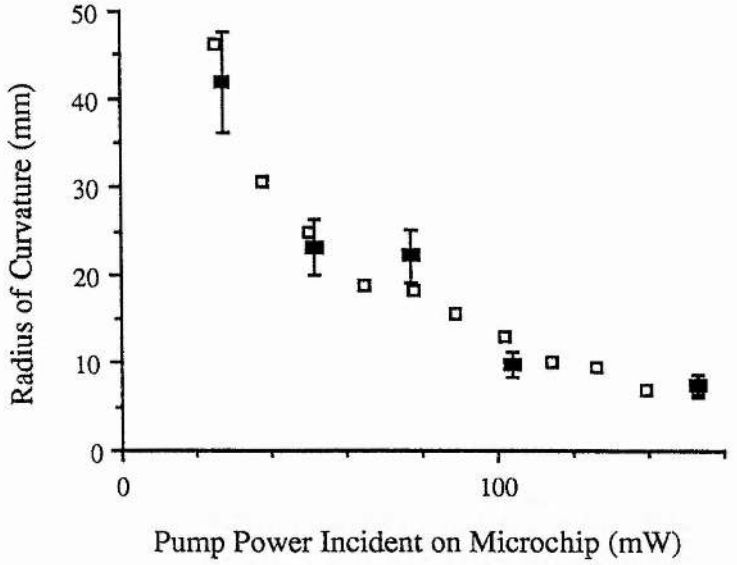

Figure 3.4.3: Radius of Curvature of the Input Surface of the Device as Measured by (i) Internal Fringe Structure (Filled Squares) (ii) Confined Mode Divergence (Open Squares)

The good agreement between the radius of curvature of the input surface, as measured by the internal fringe structure and that expected from the fundamental oscillating waist size points to the half-symmetric model we have adopted as being appropriate to the pump power induced LNP microresonator modification. In effect, the input surface deformation acts like an effective, stable confining or guiding mechanism as described in chapter 2 for Nd:MgO:$LiNbO_3$ microchip lasers. The radius of curvature of the input surface is powerful enough to counteract the spreading, by diffraction, of a confined, lowest order Gaussian eigenmode[16,17]. As in the distributed graded refractive index confinement mechanism [16,17] , the stronger the pumping of the material the smaller (more divergent) the eigenmode that can be "trapped" by the guiding mechanisms. However, unlike the distributed effects observed in Nd:MgO:$LiNbO_3$ microchip lasers

and Nd:YAG microchip lasers [28] in LNP confinement of the eigenmode comes from a more localised effect in the form of modification to the cavity geometry by input surface deformation and the refractive index profile within the device is of a type which would, without input surface curvature, prohibit stable confinement [16,17].

Having established, experimentally, that effective pump power induced curvature of the input surface of the device confines a stable Gaussian eigenmode the LNP microchip laser was placed in a modified Fizeau interferometer so as to establish the component parts of the observed deformation. The modified Fizeau incorporated a high quality optical flat in addition to the LNP microchip. The form of the more complex interferometer [27] may be seen below.

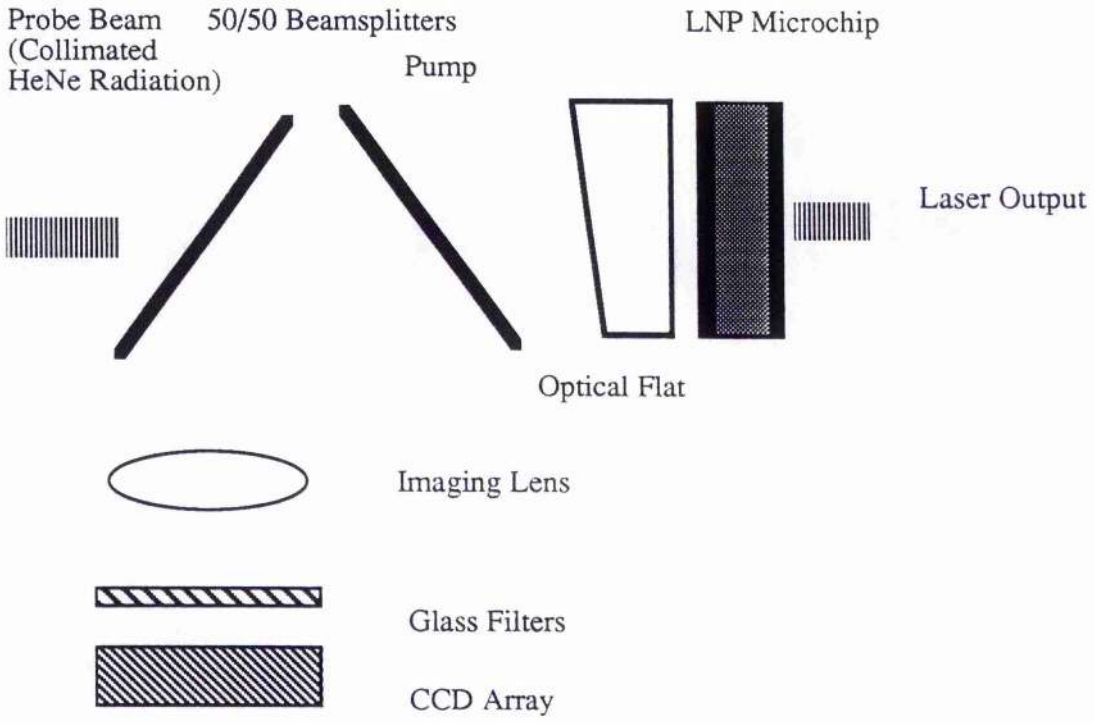

Figure 3.4.4: Modified Fizeau Interferometer for the Examination of Input Surface Deformation of LNP Microchip Laser

By choosing the polarisation of the HeNe laser appropriately the natural birefringence of LNP was used to minimise the effects of reflections from the unpumped surface forming prominent fringes between the flat and the unexamined surface. In the light of the assumption of input surface curvature being the main factor in producing a stable cavity

particular interest devolved on any changes in the input surface configuration of the device. The pump power induced modification of the input surface was measured by interfering 633 nm radiation reflected from the input surface of the device and a high quality optical flat. The negative dn/dT of LNP [15] was expected to act against cavity stability and any observed curvature of the input surface would be expected to be larger than that implied from the divergence of the confined eigenmode. The measured radii of curvature of the pumped surface can be seen in the figure below in comparison with the radii of curvature as calculated from the internal fringes and from the confined eigenmode waist.

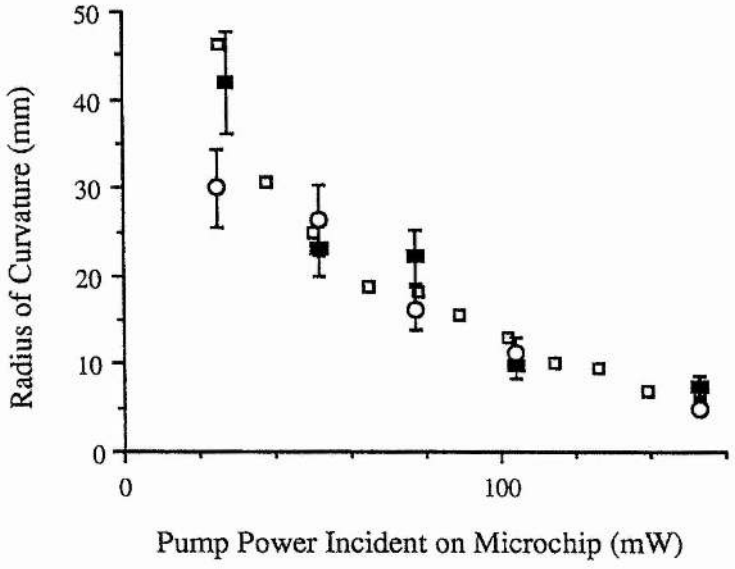

Figure 3.4.5: Radius of Curvature of the Pumped Surface as
(i) Directly Measured (Open Circles)
(ii) Measured from Internal Fringe Structure (Filled Squares)
(iii) Implied from Confined Mode Divergence (Open Squares)

Within the limits of the experimental errors associated with the procedure the curvature of the pumped surface was essentially the same as that seen in the internal fringe structure and that implied from the divergence of the oscillating mode. Using the most sensitive orientation of optical flat no measurable distortion of the output coupler surface could be detected at any of the incident pump powers used.

In chapter 2 the structure of a confining duct was examined and the need for a quadratic refractive index variation in the duct was stressed. Similarly the input surface deformation, over the dimensions of the oscillating mode, must approximate well to being a spherical surface otherwise confinement of a stable eigenmode would be impossible. The radius of curvature of the effective input surface is given by

$$R = \frac{D^2}{2\delta} \qquad \text{Eqn. 3.4.1}$$

Where R is the effective radius of curvature, D is the transverse dimensions of the oscillating mode at the input surface and δ is the observed physical height change of the input surface deformation from the centre. If we plot D^2 as a function of 2δ then the correlation between the two should be linear. From the figure below for 77 mW of pump it may be seen that the relation between D^2 and 2δ is linear. Therefore, over the dimensions of the oscillating mode the input surface deformation approximates very well to being a spherical surface.

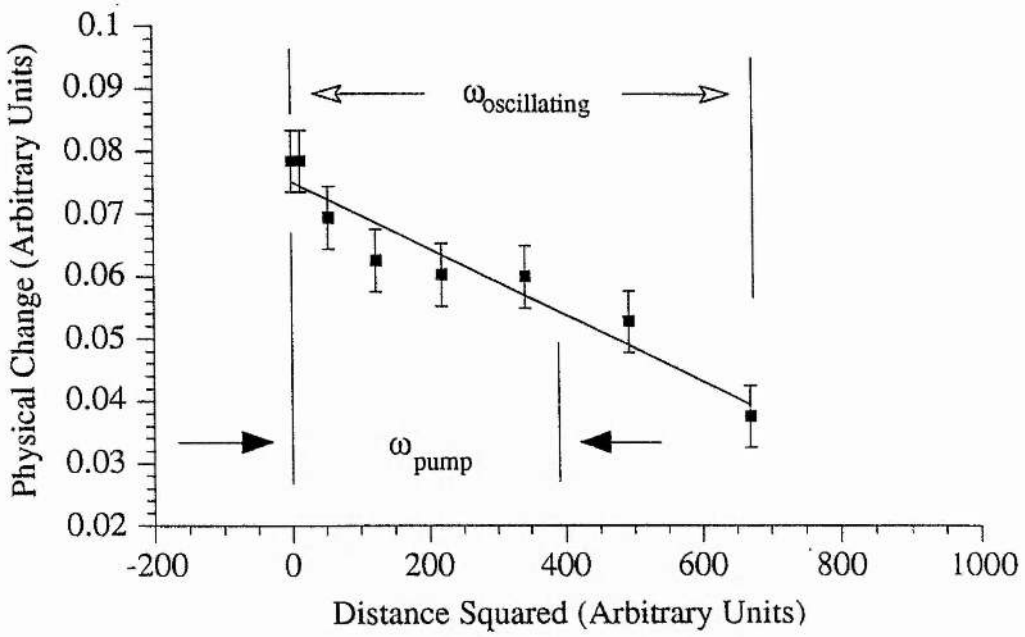

Figure 3.4.6: Sphericity of Input Surface Deformation (fit to points is linear)
ω_{pump} is the Pump Beam Radius
$\omega_{oscillating}$ is the Confined Gaussian Eigenmode Radius

Therefore the predominant contribution to the formation of a thermally induced effective confining mechanism in the LNP device is pump power induced deformation of the input surface. The refractive index change within the bulk of the material did not contribute actively to the stability of the microresonator. Output coupler deformation made no measurable contribution to the confinement of a stable eigenmode.

Contribution of Short Time Constant Effects to Cavity Stability

As was outlined in chapter 2 gain related effects , in addition to thermal effects, may contribute to cavity stability [29,30]. These gain related effects, which are associated with the upper state lifetime of the active ion, usually have a much shorter time constant than thermal effects which are usually associated with the properties of the host material itself. Gain guiding [30] is an effect with a short time constant, as was outlined in chapter 2. This is where preferential amplification of the centre of a Gaussian beam produces a mode size smaller than that expected by diffraction alone [29,30]. To ascertain the relative contributions of the short and long time constant effects the pump beam for the LNP microchip laser was chopped at 1 kHz with a 50% duty cycle. If definition of the transverse mode of operation were by short timescale, gain related effects then the confined mode size would be dependent on instantaneous power. Therefore there would be no difference in the mode size between the chopped pump beam and the unchopped pump beam. The dimensions of the diffraction limited output beam in the far-field were used to calculate the mode size within the device for the chopped and unchopped pump beam. The figure 3.4.7 below shows the fundamental mode size within the microchip laser as a function of average pump power for both cases.

The dependence of the confined eigenmode size on average power (figure 3.4.7) and not instantaneous power points, as was seen in Nd:MgO:$LiNbO_3$ microchip lasers, to the predominance of thermal effects over short time constant effects. To confirm this observation the same area of the device was pumped with a continuous wave pump and then with a chopped pump beam and the instantaneous power required to reach

threshold was measured. The rationale of this particular experiment was as follows. If the definition of the transverse mode of operation was solely due to the presence of optical gain then the threshold of the device would be dependent on the instantaneous pump power incident on the device. If the definition of the transverse mode of operation were dependent not only on the presence of optical gain but also the thermally induced formation of a confining duct to create a stable cavity then the peak power threshold would be different between the chopped and unchopped cases.

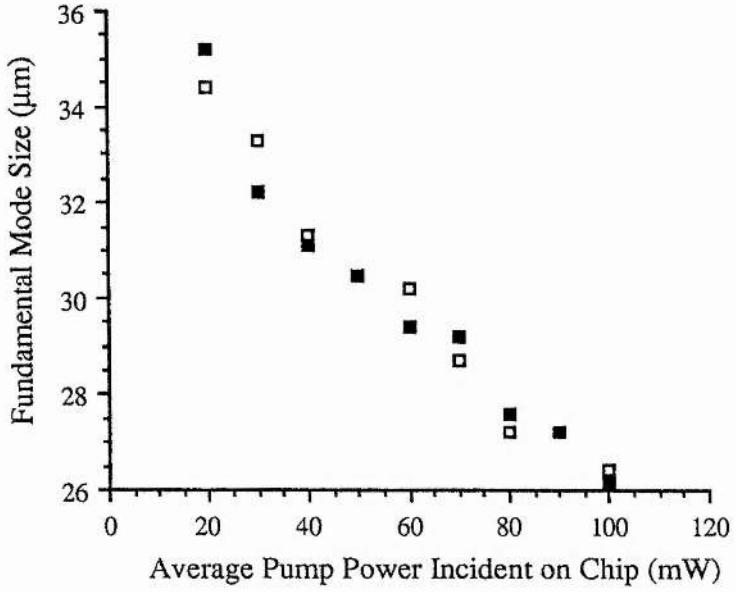

Figure 3.4.7: Dimensions of Oscillating Mode with Chopped (Open Squares) and Unchopped (Filled Squares) Pump Beam

The figure 3.4.8 below shows the threshold of the LNP microchip laser as a function of peak power incident on the device.

With pump beam chopped the instantaneous power threshold has increased significantly and clearly additional peak power is needed to create the correct thermal conditions for a stable microresonator. The pump spot was moved from the best area of the device in to the upper region where cavity mirror non-parallelism was more pronounced. The

above experiment was repeated and figure 3.4.9 below shows that the peak power threshold has increased by a factor of almost two.

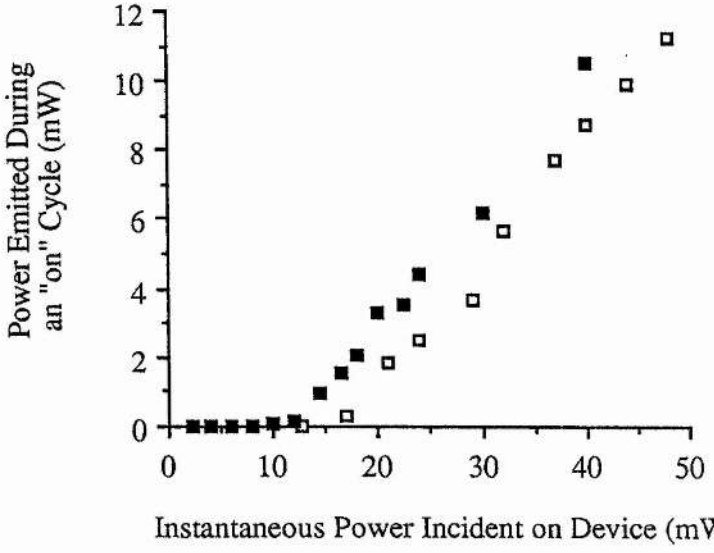

Figure 3.4.8: Instantaneous Pump Power Threshold of the LNP Microchip Laser for Chopped (Open Squares) and Unchopped (Filled Squares) Pump Beam

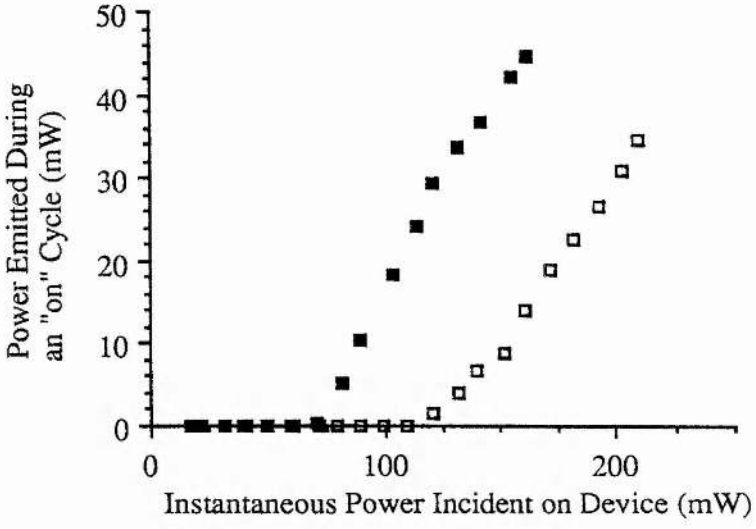

Figure 3.4.9: Instantaneous Pump Power Threshold of the LNP Microchip Laser for Chopped and Unchopped Pump Beam In Poorer Area of Crystal

The fact that the threshold of the device exhibits a strong dependence on the average pump power incident on the device and not a dependence on the instantaneous pump power suggests a long time constant thermally related cavity stability effect.

Section 3.5: Conclusions and Summary

The nature of the guiding mechanisms in LNP microchip lasers was deduced experimentally. The thermally dependent mechanisms rely on deposition of excess pump power with a very thin layer at the input surface of the device modifying the microresonator geometry. The microresonator changes from being nominally plane/parallel to being approximately half-symmetric. The pump power induced curvature of the input surface is sufficient to counteract the negative dn/dT of LNP and confine a stable, diffraction limited Gaussian eigenmode within the cavity. This cavity stability mechanism is in contrast to the less localised cavity stability mechanisms proposed for microchip lasers with low active ion concentrations and host materials with a positive dn/dT [28]. The size of the confined eigenmode in the Ti:sapphire laser pumped, LNP microchip laser was observed to be larger than the size of the pump spot producing the deformation of the input surface. Therefore the cavity stability mechanisms present in LNP should allow production of a good quality output beam from a poor quality pump beam.

The LNP microchip laser operated efficiently in the lowest order spatial mode at all pump powers with up to 20 mW of single frequency radiation being observed.

References

[1] G. Huber, Curr. Topics Mat. Sci., **4**, (1980), p.1

[2] H. P. Weber, Opt. and Quant. Electron., **7**, p. 431-442, (1975)

[3] P. Moeckel, Frequenz, **32**, p. 85, (1985)

[4] H. G. Danielmeyer and M. Blaette, Appl., Phys., **1**, p. 269-273, (1973)

[5] H. Koizumi, Acta Cryst., **B32**, p. 266, (1976)

[6] G. Winzer, P. G. Moeckel, R. Oberbacher and L. Vite, Appl. Phys, **11**, p.121-230, (1976)

[7] G. Winzer, P. G. Moeckel and L. Vite, I. E. E. E., J. Quant., Electron., **QE-14**, no. 11, p. 840, (1978)

[8] K. Otsuka, T. Yamada, M., Saruwatari and T. Kimura, I. E. E. E., J. Quant., Electron., **QE-11**, no. 11, p. 330, (1975)

[9] W. W. Kruehler, R. D. Plaettner and W. Stetter, Appl. Phys., **20**, p. 329-334, (1979)

[10] Spectra Diode Laboratories, San Jose, Ca., U.S.A., Laser Diode Operators Manual

[11] G. J. Dixon, L. S. Lingvay and R. H. Jarman, I. E. E. E. Photon. Tech. Lett., **1**, no. 5, p. 97, (1989)

[12] R. L. Townsend, C. M. Stickley and A. D. Maio, Appl. Phys. Lett., **7**, no. 4, p. 94-96, (1965)

[13] A. P. Veduta, A. M. Leontovich and V. N. Smorchkov, Sov. Phys. JETP, **21**, no. 1, p. 59-63, (1965)

[14] H. P. Weber and B. C. Tofield, I. E. E. E., J. Quant., Electron., **QE-11**, no. 7, p. 368-370, (1975)

[15] J. Nakano, J. Appl. Phys., **52**, no. 3, p.1239-1242, (1980)

[16] A. Siegman, "Lasers", University Science Books, (1986), p. 588-589

[17] A. Yariv, "Quantum Electronics", Wiley, Third Edition, p. 108

[18] J. J. Zayhowski and A Mooradian, Opt. Lett., **14**, p. 618, (1989)

[19] I.T.I. Electro-optics Corp., Los Angeles, Ca., U.S.A., Data sheet on Nd:YVO_4

[20] S. A. Payne, B. H. T. Chai, W. L. Kway, L. D. Deloach, L. K. Smith, G. Lutts, R. Peale, X. X. Zhang, G. D. Wilke and W. F. Krupke, Paper CPD12-1/24, Conference on Lasers and Electro-optics, (CLEO), 1993, Technical Digest Series, Vol. 11, Optical Society of America, Washington D. C., U. S. A., p.24

[21] N. MacKinnon and B. D. Sinclair, Opt. Comm., **94**, p. 281-288, (1992)

[22] N. MacKinnon, C. J. Norrie and B. D. Sinclair, European Quantum Electronics Conference, (EQUEC), Technical Digest, Paper PLWe32

[23] J. J. Zayhowski, I. E. E. E., J. Quant. Electron., **QE-26**, no. 12, p.2052-2057, (1990)

[24] J. J. Zayhowski, Opt. Lett., **15**, p. 431-433, (1990)

[25] A. Siegman, "Lasers", University Science Books, (1986), p. 867

[26] A. Siegman, "Lasers", University Science Books, (1986), p. 558-580

[27] W. H. Steel, "Interferometry", Cambridge University Press, (1967), p. 10

[28] J. J. Zayhowski, in Optical Society of America Proceedings on Advanced Solid-State Lasers, H. P. Jenssen and G. Dube, eds., Vol. 13, (Optical Society of America, Washington D. C., U.S.A.)

[29] G. K. Harkness and W. J. Firth, J. of Mod. Opt., **39**, no. 10, p. 2000, (1992)

[30] L. Casperson and A. Yariv, Appl. Phys. Lett., **12**, no. 10, p. 355-357, (1968)

Chapter 4: Operating Characteristics and Spectral Behaviour of a Laser-diode-array-pumped, Lithium Neodymium Tetraphosphate, $LiNdP_4O_{12}$, (LNP) Microchip Laser.

Introduction

In this chapter the principal operational characteristics of a laser diode pumped LNP microchip laser are briefly outlined. The single frequency modelling associated with microchip lasers, based on spatial dephasing of adjacent longitudinal modes, is then presented and adapted appropriately for application to the laser diode pumped LNP device. Particular consideration is then given to the observed spectral properties of the output from the LNP device and its variation with pump absorption within the gain material. The experimental results on the spectral behaviour of the device are then compared with those expected from the longitudinal mode dephasing model to ascertain the contribution of excited state migration to the single frequency properties of the LNP device.

4.1: A Laser-diode-array-pumped LNP Microchip Laser

The microchip laser pumped by the laser-diode-array was the same device as was described in the previous chapter. The characteristics of the microchip laser may be seen in figure 3.3.1 and in figure 3.3.2.. The device was excited longitudinally by a half-Watt laser diode array in a coupling optics configuration chosen to mimic, at the input surface of the device, the pump field produced at the open facet of the laser diode array [1]. The configuration of the coupling optics was exactly the same as that used in the excitation of the Nd:MgO:$LiNbO_3$ microchip laser described in chapter 2 and may be seen in figure 4.1.1. To monitor the absorption of the pump radiation within the LNP material a glass slide was placed between the 8 mm collimating lens and the 6.5 mm focussing lens. The small amount of the pump taken off was then focussed down on to a polished

but uncoated slice of LNP that was 250 μm thick. By examining the transmission of the incident pump through the control sample of LNP the pump absorption coefficient could be monitored continuously and thus fluctuations in the output spectrum of the laser diode could be detected.

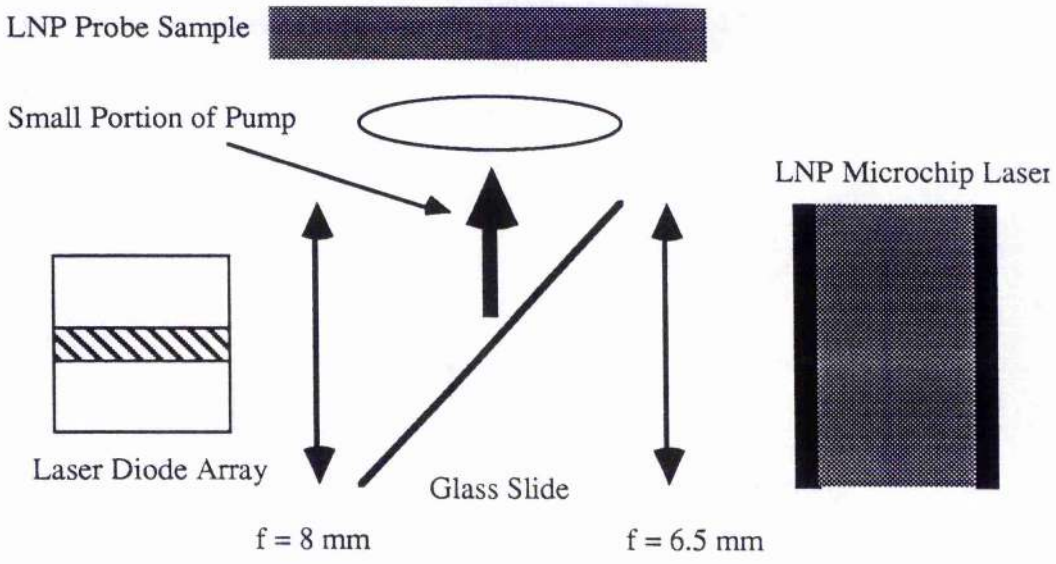

Figure 4.1.1: Longitudinal Excitation Scheme and Control LNP Sample for Laser-diode-array-pumped LNP Microchip Laser

The operational wavelength of the laser diode was temperature tuned to a maximum measured absorption coefficient of the pump radiation within the material of 18.9 mm^{-1} (as compared to 26 mm^{-1} with Ti:sapphire laser pump radiation [2]). The lower value for the absorption coefficient with the laser diode pump source was deemed to be due to the 2 nm emission bandwidth of the laser diode [1]. The pump spot produced near the front surface of the 6.5 mm lens was scanned using a large area photodiode apertured with a 5 μm pinhole. The pump spot was found to be approximately 100 μm, full width half maximum (F.W.H.M.), in the plane parallel to the junction of the laser diode and 30 μm F.W.H.M. in the plane perpendicular to the junction of the laser diode array. This compares with a measured Gaussian symmetrical pump spot size of 17 +/- 5 μm for Ti:sapphire laser pumping. The LNP microchip laser was translated such that the device was pumped by the laser diode in exactly the same region of high optical parallelism as

was exploited by using Ti:sapphire laser pumping. The power characteristics of the device may be seen below.

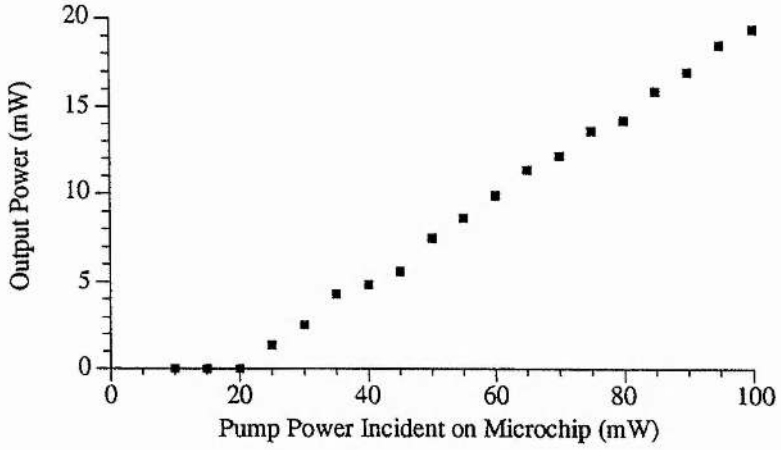

Figure 4.1.2: Power Characteristics of Laser-diode-array-pumped LNP Microchip Laser

With a slope efficiency of 24 % and an incident pump power threshold of 20 mW the diode pumped LNP device constituted a very compact and efficient source of coherent, near infra-red radiation. The lower slope efficiency and higher threshold of the laser diode pumped device, as compared with Ti:sapphire laser excitation, was deemed to be due to the larger gain volume associated with the larger laser diode pump spot and wider diode emission bandwidth. The effect of the larger gain volume is to lower the overlap between the mode and pump volume.

Following the method outlined in the beam quality section of the previous chapter the output beam of the device was found to propagate with an M^2 [3] value of 1.1 +/- 0.1 at all incident pump powers. At lower incident pump powers a slight ellipticity was however measurable in the waist of the output beam. For 25 mW of incident pump radiation the ratio of larger to smaller waists was 1.11. Doubling the pump power to 50 mW yielded a near circular beam with the waists ratio coming down to 1.06. Beyond this pump level no ellipticity in the output beam could be detected. The origin of the beam ellipticity may be due to the asymmetry of the pump spot inducing different radii of curvature on the input surface of the device at low pump powers. As the pump power

is increased the thermal spreading of the absorbed pump produces near equal curvature in both directions and, to within the limits of the experimental procedure, equal beam waists. When pumped at peak absorption the laser diode array pumped microchip laser produced approximately 14 mW of single frequency 1.047 μm radiation. As was observed with Ti:sapphire laser pumping of the device [2], multi-longitudinal mode operation was characterised by excitation of a cavity mode situated beneath the adjacent 1.055 μm gain bandwidth in preference to an adjacent mode beneath the principal 1.047 μm gain bandwidth [2,4]. The spectral behaviour of the device will be discussed in considerably more detail in section 4.3. As observed above with Ti:sapphire laser pumping the output of the LNP microchip laser was very strongly linearly polarised in a direction parallel to the crystal c-axis of the LNP material. The figure below summarises some of the main operating characteristics of the Ti:sapphire pumped and the laser diode pumped devices.

Operating Characteristic	**Ti:sapphire Pumped LNP Microchip**	**Laser Diode Pumped LNP Microchip**
Pump Spot Size(μm)	18	120 x 30
Peak Absorptivity (mm^{-1})	26	19
Slope Efficiency (%)	45	24
M^2	1.05	1.1
Maximum Single Frequency Power (mW)	20	14
Pump Power Threshold (mW)	12	20

Figure 4.1.3: Comparison of Ti:sapphire Pumped LNP Microchip Laser andDiode Pumped LNP Microchip Laser

4.2: Modelling of the Single Frequency Characteristics of Microchip Lasers

A microchip laser relies on having a large c/2nl axial mode spacing with respect to the solid-state material gain bandwidth in order to produce a compact laser device with

good single frequency characteristics. For commonly used solid-state gain media, such as Nd:YAG or Nd:YLF, the width of the principal gain bandwidth is usually of the order of 200-300 GHz [6,7,8] and a cavity length in the sub-millimetre range provides both an appropriately large intracavity mode spacing and sufficient pump absorption. The figure below outlines an imaginary situation where a cavity length is chosen so as to provide a large intracavity axial mode spacing with respect to the optical gain bandwidth.

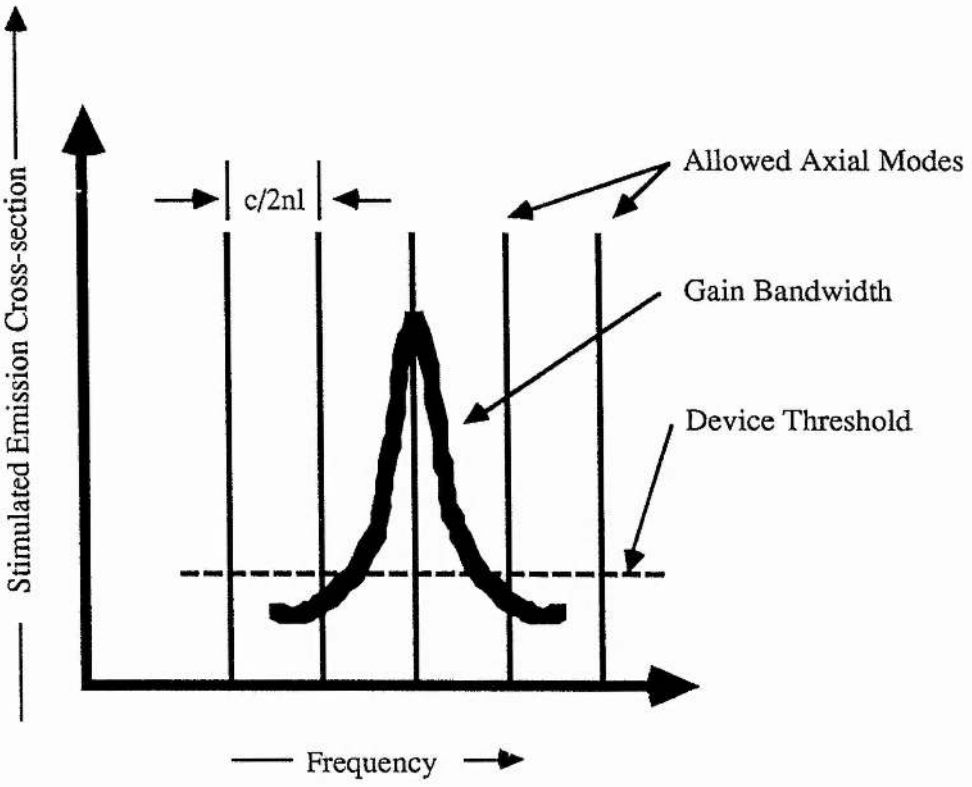

Figure 4.2.1: Interaction Between a Large c/2nl Axial Mode Spacing and an Emission Bandwidth

This technique, to eliminate multi-axial mode operation in a plano/plano linear cavity, was first successfully exploited by Stillman et al. in 1966 [9] in CdSe semiconductor material. By reducing the thickness of the CdSe down to approximately 20 μm the multi-axial mode operation seen in the thicker samples was eliminated. Since then [2-8] this technique has also been applied to great effect in optically pumped solid-state lasers thus forming the sub-group of solid-state lasers known as microchip lasers [6].

Several other methods of achieving high performance single frequency operation in solid state lasers have been utilised [10-14]. Among these approaches are those which have centred upon mitigation or indeed the elimination of the effects of the phenomenon, first investigated by Tang in 1963 [11], known as "spatial hole-burning". The first such method was investigated by Ehutov and Siegman [12] and was called the "twisted mode" technique. Intracavity waveplates were used to produce circularly polarised oscillation of the laser radiation within the gain medium. Consequently extraction of the inversion density within the gain medium was spatially uniform and the possibility of the formation of spatial anti-nodes in the inversion density eliminated [10,12]. Another widely used technique is to force travelling wave operation [13] of the laser radiation thus removing the possibility of the existence of spatial anti-nodes in the inversion density within the gain material. Clearly, the above techniques and others, though varied and highly effective in many applications, have the disadvantage of increased device complexity and cost and certainly do not have the extreme simplicity and mass-producibility of the microchip laser approach.

However, microchip lasers do have linear, standing wave cavities and clearly will, under the appropriate pump conditions, be susceptible to the effects of spatial hole burning. If a microchip laser is pumped sufficiently far above threshold then even longitudinal cavity modes situated on the edges of the gain profile may see enough gain to oscillate. The issue may be further complicated by the presence of additional transitions, located near to the principal transition, which may be sufficiently strong so as to drive axial cavity modes [2,4]. Clearly the exact behaviour of a microchip laser will depend on the spectroscopic properties of the gain material and the intra-cavity mode separation of the linear cavity. However, the situation may be summarised in the greatly simplified diagram below figure 4.2.2.

The single frequency properties of individual devices will, of course, vary depending on exactly what is the axial mode spacing of the cavity and what are the spectroscopic properties of the gain material. In addition to the differential stimulated emission cross-

section between two longitudinal modes they may also compete, spatially, for the same population inversion. If this spatial overlap between the two modes is significant then additional suppression, as compared to the situation where the gain material is uniformly pumped, of the second cavity mode may occur [14]. This limit on the single frequency behaviour of a linear, standing wave cavity imposed by spatial hole burning has been considered by many authors [15-20]. In particular Zayhowski has developed a model appropriate to microchip lasers based on the spatial dephasing of adjacent longitudinal modes [17,18].

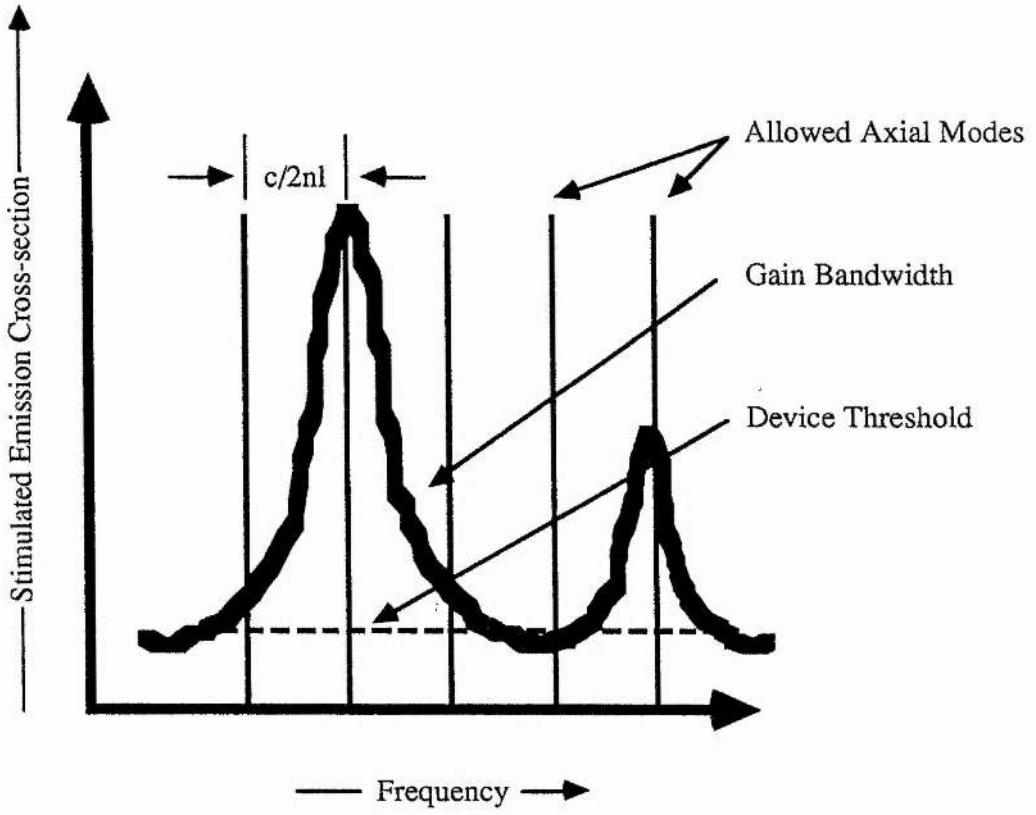

Figure 4.2.2: Interaction Between a More Complex Emission Band and a c/2nl Intra-cavity Mode Spacing

We shall now introduce this model in detail and subsequently adapt it appropriately to suit the conditions present in the laser diode pumped LNP microchip.

Consider a continuous wave laser made of a standing wave cavity of length l filled completely with a homogeneously broadened [17] gain medium. For the purpose of the

analysis we shall assume that the round trip loss within the cavity is relatively low such that a well defined standing wave field pattern is formed within the cavity. We shall also assume that the saturated inversion density is unaffected by any mechanisms leading to excited state migration [18,19-23] and that the oscillating radiation approximates to being a plane wave throughout the length of the device. Throughout the following discussion we shall also assume that the two longitudinal modes to be discussed see identical round trip losses ($\gamma_1=\gamma_2$). For lasers operating on two adjacent axial modes , under the same bandwidth, this is a valid approximation. Two such axial modes will be spaced relatively closely in frequency such that they will see identical reflectivity from the dielectric coatings used to define the cavity. Similarly, two adjacent axial modes operating under the same bandwidth are unlikely to terminate in different lower laser levels and consequently see different reabsorption losses.

The optical gain, Γ, seen by an oscillating mode may be given by integrating the product of the stimulated emission cross-section, the normalised mode intensity and the population inversion density profile with which the optical field is interacting [14]. For the first mode to oscillate this may be expressed as shown below.

$$\Gamma_1 = \sigma_1 \int_0^L \frac{N(z)I_1(z)dz}{I_1} \qquad \text{Eqn. 4.1}$$

The circulating intensity has the form

$$I_1(z) = 4I_1 \sin^2(k_1 z) \qquad \text{Eqn. 4.2}$$

where k_1 describes the wavenumberof the oscillating radiation. The inversion density N(z) is given by, in the presence of saturation

$$N(z) = \frac{N_0(z)}{1+\frac{I_1(z)}{I_{sat.}}} \qquad \text{Eqn. 4.3}$$

$N_0(z)$ is the inversion in the absence of saturation and is proportional to the local pump rate, I(z) is the oscillating mode intensity as a function of distance and $I_{sat.}$ is the

saturation intensity [24,25] of the solid-state gain medium at the frequency ω_1. The first mode to oscillate (mode 1) will be the axial mode with the highest cross-section for stimulated emission. This oscillating mode will saturate the population inversion reducing the gain available to a second mode. The saturated optical gain as expressed by equation 4.1 will then saturate to unity. Therefore a second axial mode must see in order to oscillate, integrated over the length of the gain medium, an equal value of saturated optical gain as that seen by the already oscillating first mode assuming identical round trip losses for both modes ($\gamma_1=\gamma_2$) .

The condition for single frequency operation then becomes

$$\sigma_2 \int_0^L \frac{N(z)I_2(z)dz}{I_2} < \sigma_1 \int_0^L \frac{N(z)I_1(z)dz}{I_1} \qquad \text{Eqn. 4.4}$$

As may be seen from the above equation the gain available to the possible secondary axial mode is altered by the saturated population distribution produced by the oscillating initial mode. Therefore to assess the amount of gain seen by the secondary mode we must consider the spatial overlap of the two intensity patterns produced by modes one and two.

For the sake of simplicity we shall assume for the moment that the inversion density in the solid-state gain material is uniform spatially. If the phase difference between the two patterns tends to zero radians then the two patterns are increasingly overlapped and consequently are increasingly accessing the same regions of inversion and in this case the first mode to lase will, if the overlap is perfect, efficiently deplete the gain for the second mode. Therefore the second mode will never reach threshold. If the standing wave maxima of one mode line up with the nodes of the other then the two modes will be depleting completely different regions of gain and this situation is clearly the most favourable environment for the oscillation of a second mode.

However, the above description of the overlap of the two sinusoids must be modified when considering the physical situation present in a microchip laser. The microresonator

formed by the two mirrors stipulates that both standing wave patterns must have nodes at both the input and output mirrors. This situation may be represented by the schematic below

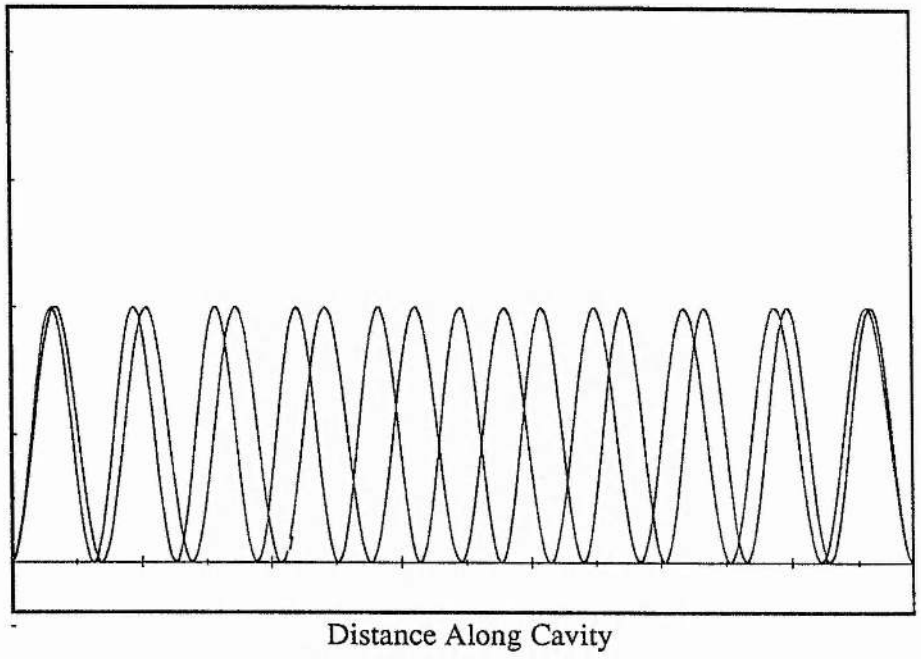

Figure 4.2.3: Spatial Overlap of Intensity Patterns of Two Longitudinal Modes in a Microchip Laser

As may be seen from the above figure it is evident that the two patterns go through regions of alternate overlap and dephasing. Consequently the spatial overlap of the two modes must be integrated along the length of the cavity. We may represent therefore the spatial overlap of two sinusoidal intensity patterns with phase difference η over a distance l by the equation below.

$$\varsigma = \int_0^L \cos\eta dz \qquad \text{Eqn. 4.5}$$

At this point we can introduce what Zayhowski has called the correlation factor [17,18] which expresses the spatial overlap between the inversion profile $N_0(z)$ and the intensity patterns associated with both oscillating cavity modes.

$$\psi(1,2) = \int_0^L N_0(z)\cos\eta dz \qquad \text{Eqn. 4.6}$$

The correlation factor can be normalised with respect to the cavity length and the total inversion density, $\langle N_0 \rangle$.

$$\langle \psi(1,2) \rangle \equiv \frac{1}{L\langle N_0 \rangle} \int_0^L N_0(z) \cos \eta dz \qquad \text{Eqn. 4.7}$$

where

$$\langle N_0 \rangle = \frac{1}{L} \int_0^L N_0(z) dz \qquad \text{Eqn. 4.8}$$

is the total amount of inversion present, before saturation, integrated throughout the length of the gain material. The normalised correlation coefficient is therefore the spatially available integrated gain that is common to both longitudinal modes.

The single mode condition expressed in equation 4.4 can now be re-expressed as below

$$\langle N_0 \rangle \langle \zeta(1,2) N_{Th.} \qquad \text{Eqn 4.9}$$

Where $\langle N_0 \rangle$ is given by equation 4.8. $N_{Th.}$ is the spatially averaged inversion density required to reach threshold [17,18] and $\zeta(1,2)$ is the ratio of maximum single mode inversion density to the threshold inversion density. The factor $\zeta(1,2)$ is a function of the relative stimulated emission cross-sections of modes one and two which is expressed in the factor $\beta(1,2)=\sigma_1/\sigma_2$ in the equation below. $\zeta(1,2)$ is also a function of the relative overlap of the two longitudinal modes as expressed by the normalised overlap integral $\langle \psi(1,2) \rangle$ (equation 4.6).

$$\zeta(1,2) = \left[\frac{\beta(1,2) - \langle \psi(1,2) \rangle}{(1 - \langle \psi(1,2) \rangle)^2} \right] [2\beta(1,2) - 1 - \langle \psi(1,2) \rangle] \qquad \text{Eqn. 4.10}$$

For the microchip laser under discussion the correlation factor $\langle \psi(1,2) \rangle$ may be solved analytically. The full derivation is covered in appendix A. The correlation factor $\langle \psi(1,m) \rangle$ between the principal axial mode one (that is the first mode to oscillate) and the m th axial mode to oscillate for a microchip laser of length L, refractive index n and absorption coefficient α is given by

$$\langle \psi(1,m) \rangle = \frac{1}{\left(1+\left(\frac{2\pi(m-1)}{\alpha L}\right)^2\right)} \qquad \text{Eqn. 4.11}$$

The ratio of the two stimulated emission cross section, β (1,2), is given, assuming a Lorentzian [26] lineshape for the gain bandwidth of half-width λ_{half} is given by.

$$\beta(1,2) = 1+\left[\frac{\Delta m \lambda_0^2}{2nL\lambda_{half}}\right]^2 \qquad \text{Eqn. 4.12}$$

In the absence of any non-linear effects, such as the presence of an intensity dependent output coupling, [27] the ratio of maximum single mode inversion density to threshold density is directly equivalent to the quantity $P_{pump}/P_{threshold}$. Therefore knowing the pump power threshold and slope efficiency of a solid-state microchip laser it may be possible to predict the single frequency behaviour of the device.

Spatial Dephasing in Conditions of Gain Length Compression

As was briefly mentioned above additional suppression of adjacent longitudinal modes may be achieved by localising the available gain to one end of the cavity. In solid-state lasers with external mirrors this may be accomplished by putting the gain material near the input mirror [14]. In microchip lasers this may be accomplished by utilising gain media with relatively large absorption coefficients such that the available inversion decays very quickly within the medium [14,18-20]. Equation 4.10 and 4.11 exhibit a marked dependence on the absorption coefficient and the effect of gain length compression may be envisaged by considering the physical basis behind the normalised correlation coefficient $\langle \psi(1,2) \rangle$. The normalised correlation coefficient expresses the gain seen by the second mode as obtained from the saturated population inversion. As was outlined above regions of spatial mismatch between the field patterns of modes one and two provide the appropriate gain for mode 2. However if rapid exponential decay of the gain coincides with the spatial overlap between modes one and two then the gain available to the second mode will be reduced as compared to the situation if the gain

material were more spatially uniformly pumped. Consider the case below where a uniform population density has been saturated by a principal axial mode to produce a saturated inversion which is interacting with a second mode standing wave pattern. In the case shown below the gain material is uniformly pumped.

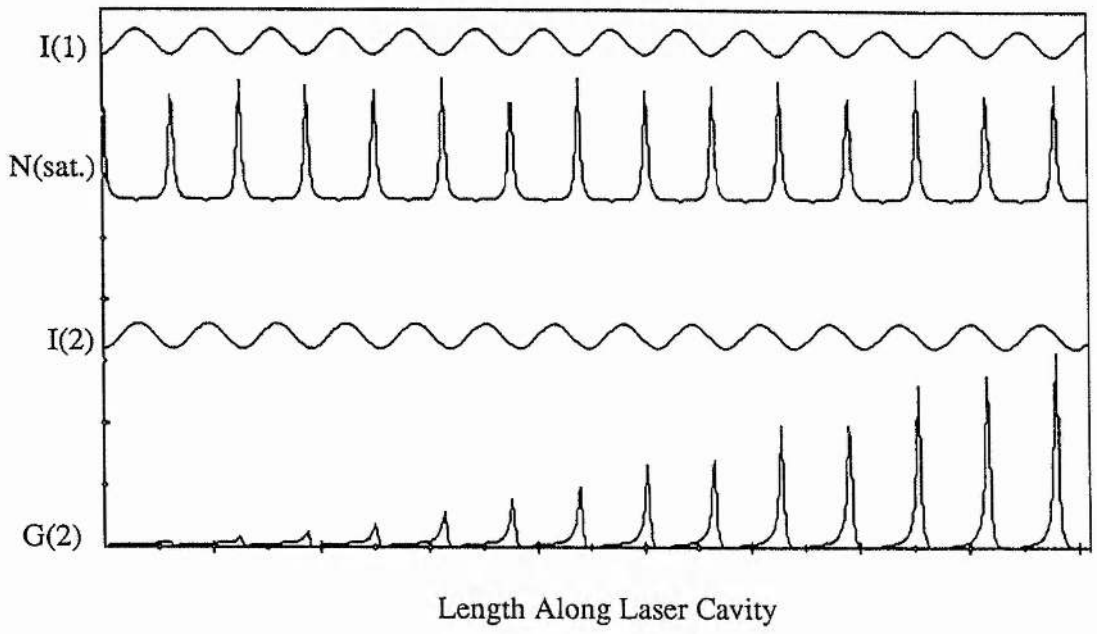

Figure 4.2.4: Integrated Gain Along Cavity from Spatially Modified Inversion Density
I(1): Standing Wave Field Pattern of First Axial Mode
N(sat.): Saturated Modified Inversion Density in the Presence of First Axial Mode
I(2): Standing Wave Field Pattern of Second Axial Mode
G(2): Gain of Second Mode as a Function of Position Along Laser Medium

In the above figure the gain as a function of position for the second mode was calculated simply by multiplying the saturated inversion profile as produced by mode one with the field pattern associated with mode two. This increasing overlap between the undepleted inversion and the secondary mode is evident to the right of the above figure. From above it may be seen that the total optical gain available to the second mode is obtained by integrating the bottom curve over the length of the cavity. Consider now the very similar case below where this time excitation of the laser material is not uniform spatially but instead the inversion decays from its initial value N_0 at a rate given by the equation below.

$$N(z) = N_0 \exp(-\alpha z) \qquad \text{Eqn. 4.13}$$

Where α is the absorption coefficient of the pump light within the material and z is the length along the active medium. In some solid-state laser media, such as LNP [2,4,5], the value of α may be as high as 26 mm^{-1} for a correctly polarised, single frequency pump source of the appropriate wavelength [2,22,28]. This would give a 1/e folding distance of the gain within the material of 38 μm which is of the order of a few tens of optical cycles at 1 μm. In some doped materials such as 3 % Nd:YVO_4 the absorption coefficient may be as high as 11.1 mm^{-1} [29]. In the figure below the periodicity of the standing wave patterns is the same as in figure 4.2.4 but the exponential decay of the inversion is shown.

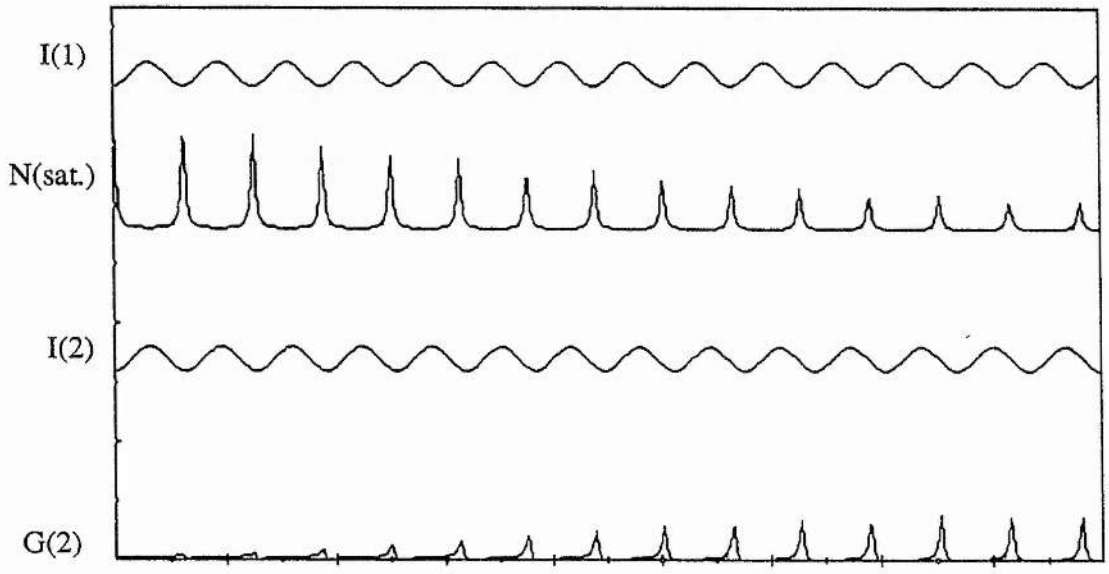

Figure 4.2.5: Integrated Gain from Spatially Modified Inversion Density
I(1): Standing Wave Field Pattern of First Axial Mode
N(sat.): Exponentially Decaying Saturated Inversion Density in the Presence of First Axial Mode
I(2): Standing Wave Field Pattern of Second Axial Mode
G(2): Gain of Second Mode as a Function of Position Along Laser Medium

As may be seen in comparison with figure 4.2.4 the available gain as integrated along the length of the laser medium has been reduced by the effective compression of the gain length within the cavity. In both figures although the units describing the inversion

density, optical field intensity and optical gain have been taken to be arbitrary the relation between the y-axes in both figures is identical so as to allow a valid comparison of the differential gain between the two differing situations. It is worth while at this juncture to apply the spatial dephasing model outlined above to a real microchip laser so as to gauge the effects both of the increased frequency separation of adjacent longitudinal modes and increasing gain length reduction.

The solid-state material neodymium doped yttrium vanadate (Nd:YVO_4) [29,30] provides perhaps the best combination of spectroscopic features for application to the model described above. Unlike the case with LNP the modelling of the single frequency properties is not complicated by the existence of additional transitions spaced closely to the principal transition at 1.064 μm. Additionally the absorption properties of Nd:YVO_4 are such that, similarly to LNP, a wide range of gain lengths may be possible in the material. The properties of Nd:YVO_4 are covered in more detail in the chapter 5. As has been mentioned above a wide range of gain lengths are possible in Nd:YVO_4 with an active ion concentration of 3% absorption coefficients as high as 11 mm^{-1} for a π-polarised λ=809 nm pump may be attained. The half width of the 1.064 μm transition in Nd:YVO_4 is 0.5 nm [18]. We shall assume that with appropriate detuning of the pump absorption coefficients from 1 to 11 mm^{-1} may be accessed and that no pump light is reflected from the output coupler. Any double-passing of the pump light, which is a common technique to increase the overall efficiency of some low-absorption solid-state materials, would clearly modify the inversion distribution away from a form of equation 4.13. In this context we shall also assume that the first cavity mode to be excited is at the peak of the gain bandwidth and the next axial mode to be excited is the one separated from the principal mode by the free spectral range of the cavity. To complete the definition of the situation we shall also assume an interaction with only the one Lorentzian gain peak at 1.064 μm. The factor $\zeta(1,2)$ for the microchip laser under consideration is shown below as a function of cavity length for two values of absorption coefficient. The absorption coefficient α=11 mm^{-1} corresponds to a 1/e folding distance for the undepleted inversion of 90 μm while the α=1 mm^{-1} coefficient corresponds to a

folding distance of 1 mm. We shall also assume that the threshold of the device does not change with increasing cavity length. This approximation may not be strictly correct in a laser material exhibiting significant scattering losses and there may be changes in the lasing threshold due to a change in the size of the thermally guided eigenmode.

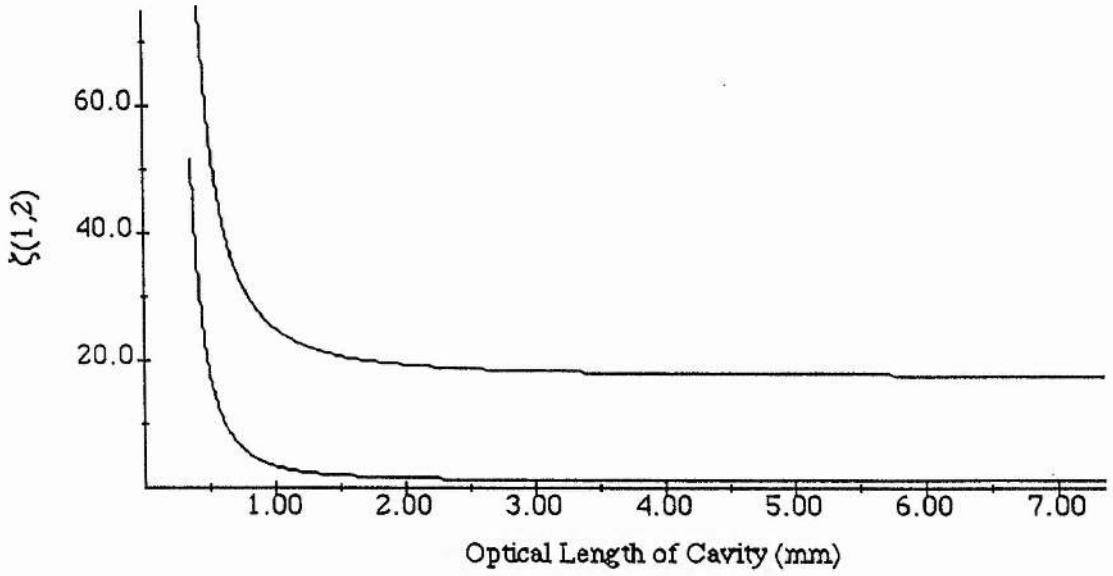

Figure 4.2.6: $\zeta(1,2)$ for Nd:YVO_4 Microchip Laser
(Upper Curve: α=11 mm^{-1})
(Lower Curve α=1 mm^{-1})

The first feature of the above graph is the significant offset between the two curves. In both the cases presented above the spatial overlap as a function of cavity length of modes one and two and also the discrimination factor, $\beta(1,2)$, as a function of cavity length between the two modes is the same for α=11 mm^{-1} or α=1 mm^{-1}. This corresponds therefore to enhanced single frequency operation of the Nd:YVO_4 device in the situation where the inversion is strongly localised at the input surface of the device. Examining figure 4.2.3 it is evident that at the input surface of the device modes one and two have a standing wave anti-node. Both axial modes therefore are significantly overlapped within the shorter gain length at α=11 mm^{-1} and are consequently competing spatially for the same population inversion. In the short gain length, high absorption situation the second possible axial mode is less able to deplete the saturated gain than in

the low absorption, long gain length environment. This situation is shown graphically in figure 4.2.5.

This particular situation, where the cavity length of a solid-state laser is many times the absorption depth within the material has been considered by Kintz and Baer [14]. In their Nd:YVO_4 laser a thin piece of gain material was located at the input surface of an external mirror cavity. The spatial overlap, integrated along the gain length, of the possible axial modes was sufficient such that the device operated up to 15 times threshold in a single axial mode.

The second important feature of figure 4.2.6 is the dependence of $\zeta(1,2)$ on the optical length of the cavity. As the optical length of the cavity increases beyond 2 mm the decreasing intracavity mode separation is defining a discrimination factor which is tending towards one. In this region therefore the single frequency properties of the device are essentially defined by the amount of localisation of the available gain. As the intracavity mode spacing increases sufficiently then the discrimination factor between the two modes begins to fall such that the situation shown diagramatically in figure 4.2.1 occurs and the single frequency performance of the device improves markedly for optical cavity lengths less than 1 mm.

Section 4.3: Single Frequency Operating Characteristics and Modelling of LNP Microchip Laser

The LNP microchip laser was set up in exactly the same coupling optics configuration as in figure 4.1.1. By measuring the transmission of pump radiation through the probe sample it was possible to make accurate measurements of the pump absorption coefficient within the material during operation of the microchip laser. Temperature tuning of the centre wavelength of the laser diode made it possible to access a whole range of absorption coefficients simply by altering the set-point temperature control on the Peltier cooler for the laser diode. The variation of pump absorption coefficient with Peltier cooler temperature may be seen below.

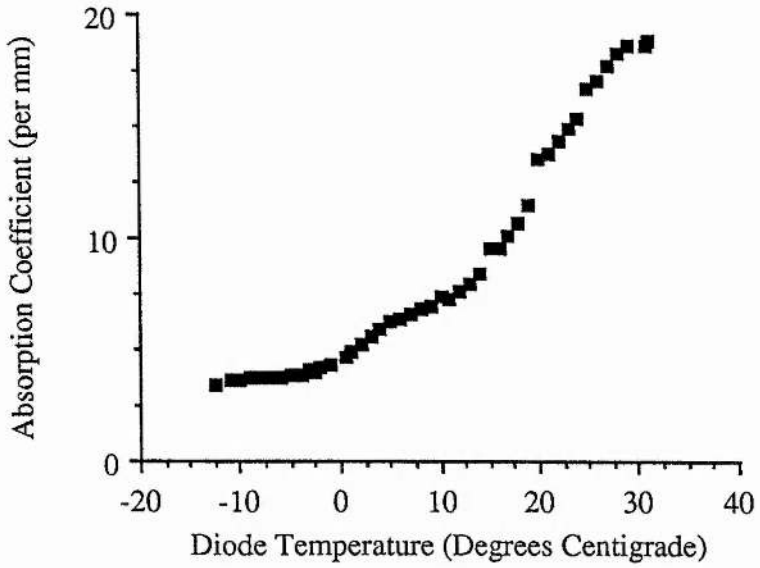

Figure 4.3.1: Absorption Coefficient of Pump as a Function of Laser Diode Temperature

As may be seen from the above curve a range of gain lengths could be easily accessed from approximately 3 mm^{-1} right up to the maximum absorption coefficient of 18.8 mm^{-1} (1/e folding distance of 50 μm). The microchip laser was pumped in the area of the device corresponding to the best optical parallelism between the surfaces. At all the values of absorption coefficients used the microchip maintained its near diffraction limited spatial performance at all incident pump powers. At all absorption coefficients the output beam was very strongly polarised in a direction corresponding to the c-axis direction, high gain polarisation operation in LNP. The output of the device was split such that the spectral purity of the beam could be monitored both with a scanning, plane-parallel Fabry-Perot etalon and a one metre "Monospek" monochromator simultaneously. As the absorption coefficient of the pump light was changed the single frequency behaviour of the device changed markedly but the multi-frequency behaviour was characterised, at all absorption coefficients, by the excitation of an axial mode situated under the nearby 1.055 μm gain bandwidth instead of an axial mode under the principal gain bandwidth [2,4]. This observed preferential excitation of a "far-away"

cavity mode need not conflict with the spatial dephasing model outlined above. The axial mode under the 1.055 μm gain bandwidth is the first axial mode which experiences sufficient dephasing over the gain length from the 1.047 μm mode and has a sufficiently large stimulated emission cross-section to see enough gain in order to oscillate [17-20,28]. For the purpose of our analysis the correlation factor (equation 4.11) will give the correct contribution to the mode's gain from spatial dephasing and the fact that the axial mode is under an adjacent transition may be taken into account by measuring from the fluorescence profile directly the relative ratios of σ_1/σ_2 and substituting in this value for $\beta(1,2)$ directly into 4.10 instead of using equation 4.12. We shall now consider the observed single frequency behaviour of the device as applied to the spatial dephasing model outlined above.

The thickness of the LNP device was measured to be 380 μm which gave an axial c/2nl mode spacing of 250 GHz. Assuming the axial mode under the principal gain bandwidth (1.047 μm) was located at the peak value of stimulated emission coefficient the axial mode driven by the 1.055 μm transition would be the thirteenth longitudinal mode from the principal mode ($\Delta m=12$). From the c-polarised fluorescence profile of LNP [28] the ratio of the two stimulated emission coefficients was found empirically to be $\beta(1,13)=1.88$ with both modes located at their respective gain peaks. For the purpose of the analysis it was assumed that both longitudinal modes experienced the same round-trip losses ($\gamma_1=\gamma_{13}$). However , as shall be seen later, some of the discrepancies between the predicted single frequency behaviour of the device and that observed experimentally may be explained by modification of $\beta(1,13)$ to include a loss differential between the two modes due to re-absorption. The single frequency behaviour of the device as modelled according to equation 4.10 and that observed experimentally may be seen below.

For each change in the absorption coefficient the device threshold was re-measured separately so as to include the fact that the device threshold was observed to be absorption coefficient dependent.

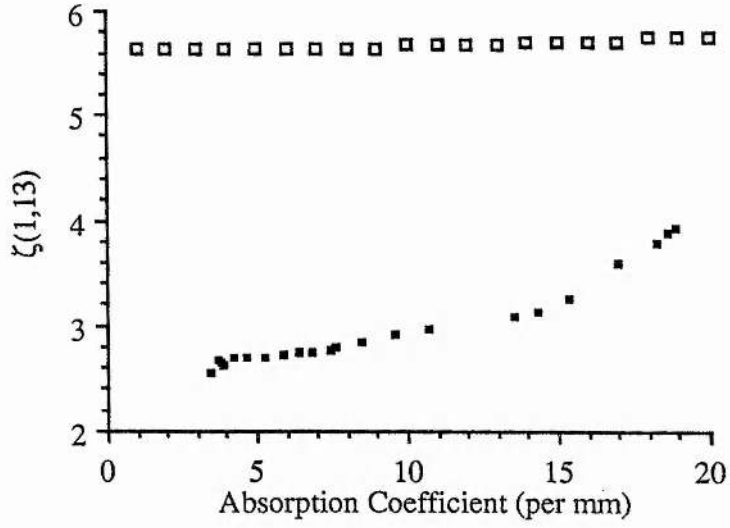

Figure 4.3.2: Single Frequency Characteristics, ($\zeta(1,13)$), of the LNP Microchip Laser as a Function of Absorption Coefficient
(Large Open Squares: Modelled Behaviour with $\beta(1,13)=1.88$)
(Small Filled Squares: Observed Behaviour)

As may be seen from figure 4.3.2 above the device operated at a maximum of four times above threshold before the onset of multi-longitudinal mode operation. The corresponding maximum single frequency power observed was 14 mW. As is implied from equation 4.10 the single frequency behaviour performance degraded with increasing gain length (decreasing absorption coefficient). In figure 4.3.2 the highest absorption coefficient corresponds to a 1/e folding distance of the gain of 50 μm. For the lowest measured absorption coefficient the same distance is approximately 320 μm. However the form of the two curves on figure 4.3.2 are markedly different. Firstly there is the offset between the modelled results and the experimental results and secondly, across the range of absorption coefficients examined, the modelled results are almost linear while the observed results show a considerable improvement over what would be expected theoretically. In section 4.2. and in the modelling applied to the LNP device it was assumed that both longitudinal modes experienced the same round-trip losses such that $\beta(1,13)=\sigma_1/\sigma_{13}$. It may be shown by incorporating the round trip losses into the single mode criterion (equation 4.4) a more rigorous definition of the discrimination

factor is $\beta(1,13)=\sigma_1\gamma_{13}/\sigma_2\gamma_1$ where γ_{13} and γ_1 are the round-trip losses for modes one and thirteen respectively. It is fairly common in most solid state lasers that the frequency difference between the two longitudinal modes may only be of the order of a few tens of GHz and each longitudinal mode is driven by the same transition. However as was observed with the LNP microchip laser the device was operating on two longitudinal modes each driven by a separate transition. Therefore the two longitudinal modes may experience different reabsorption losses due to a thermally excited population in the lower laser level associated with each transition [31-36]. Thermally dependent reabsorption losses are however not generally associated with the operation of neodymium lasers at 1 μm the existence of a thermally populated lower laser level being more of a difficulty in the operation of the 0.946 μm transition in neodymium containing materials [34-36]. However the neodymium containing material under examination (LNP) is a stoichiometric laser material which has an active ion concentration thirty times that of 1% Nd:YAG [2,4,5,28]. Consequently the lower laser levels in LNP at the 1.047 μm and 1.055 μm transitions may contain significant thermal populations.

As was outlined in section 3.2 of chapter 3 the three c-polarised transitions around 1.05 μm have the same upper laser level. Therefore the lower laser level for the 1.047 μm mode is closer to the ground state than that for the 1.055 μm mode. Consequently, for any given temperature, the thermally excited lower laser level population (and hence the reabsorption loss) will be higher for the 1.047 μm mode than for the 1.055 μm mode. This would have the effect of altering the discrimination factor so as to lower $\zeta(1,13)$. Using the Boltzmann relation [27] and the value for reabsorption loss at 1.047 μm in LNP as calculated by Otsuka [32,33] we can make an estimate as to what the loss differential, introduced by reabsorption, is between the two modes. The loss ratio between the two longitudinal modes (mode number 1 is the axial mode driven by the 1.047 μm transition and mode 13 is the mode driven by the 1.055 μm transition) may be expressed as,.

$$\frac{\gamma_{13}}{\gamma_1} = \frac{\text{O.C. + Reabsorption Losses (Mode 13)}}{\text{O.C. + Reabsorption Losses (Mode 1)}} \quad \text{Equation 4.14}$$

where O.C. is the specified output coupling loss seen by both modes. The output coupling as seen by both modes was 1 %. The round-trip reduction in amplitude of the oscillating radiation for mode n may be expressed as.

$$I_n = I_{0,n} \exp[-2\alpha_n L] \qquad \text{Eqn. 4.15}$$

where I_n is the intensity of mode n after one round trip, L is the length of the cavity and α_n is the reabsorption coefficient for mode n which is defined as being,

$$\alpha_n = N_n \sigma_n \qquad \text{Eqn. 4.16}$$

where N_n is the thermally excited lower laser level population and σ_n is the reabsorption cross section which we shall assume as being equal to the stimulated emission cross-section for the appropriate transition [28]. Taking Otsuka's measurement of the reabsorption coefficient as being α_1=0.007 mm^{-1} it is possible to manipulate equation 4.16 for modes one and 13 as shown below.

$$\alpha_{13} = \frac{N_{13}\sigma_{13}}{N_1\sigma_1}\alpha_1 \qquad \text{Eqn. 4.17}$$

Using the Boltzmann relation and the known values of stimulated emission cross-section it may be shown that the loss ratio between the two modes is equal to 0.8. Therefore the discrimination factor between the 1.047 μm axial mode (mode 1) and the 1.055 μm axial mode (mode 13) at T=300 K is modified below as shown.

$$\beta^*(1,13) = \frac{\sigma_1}{\sigma_{13}} \frac{\gamma_{13}}{\gamma_1} = 1.47 \qquad \text{Eqn. 4.18}$$

The effect of the inclusion of a reabsorption loss differential is to shift down the modelled values of $\zeta(1,13)$ to approximately the levels experimentally observed. In figure 4.3.3 three different operating temperatures for the device are shown. However,

as may be seen in figure 4.3.3 the form of the observed results is still markedly different form the modelled results.

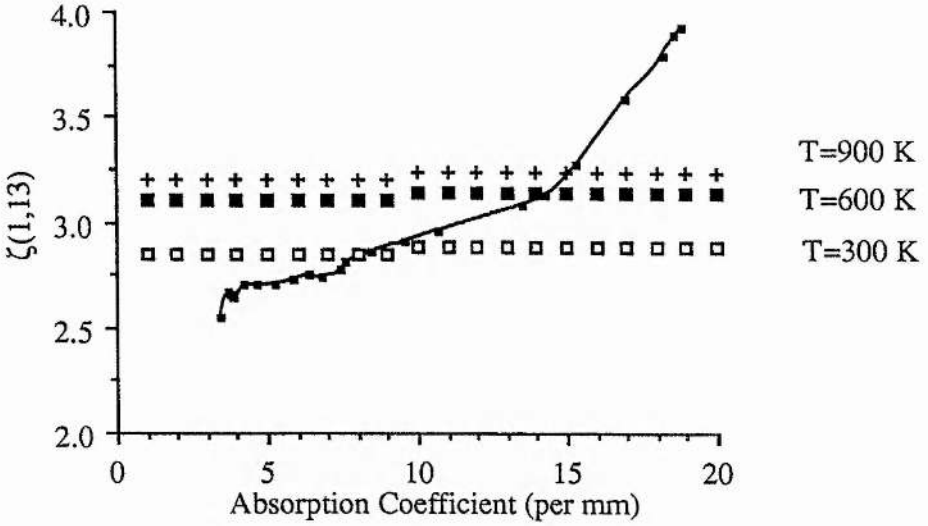

Figure 4.3.3: Single Frequency Characteristics, ($\zeta(1,13)$), of the LNP Microchip Laser as a Function of Absorption Coefficient Including Modified Discrimination Factor. (Small Filled Squares with Interpolation): Experimental Results (Open Squares): Modelled Behaviour at T=300 K, $\beta^*(1,13)=1.47$ (Larger Filled Squares): Modelled Behaviour at T=600 K, $\beta^*(1,13)=1.52$ (Crosses): Modelled Behaviour at T=900 K, $\beta^*(1,13)=1.54$

With decreasing gain lengths at high absorption coefficients the increased thermal loading occurring as the pumped volume becomes smaller may change the value of the reabsorption loss. From the Boltzmann relation it is evident that any increase in temperature would tend to reduce the thermally excited population differential between the two modes. This would lead to a reduced loss differential and the modified discrimination factor, $\beta^*(1,13)$, would tend towards the value given by the ratio of the stimulated emission cross sections. However as may be seen from figure 4.3.3 markedly significant rises in operating temperature are required even for a modest reduction in the differential loss between the two modes.

The remaining possible explanation for the better than predicted single frequency performance of the device is the possibility that migration of excited states is present in the material at increased excitation densities. The effect of excited state migration in the

suppression of spatial hole burning has been considered qualitatively by other authors. [18,20-22]. Excited state migration lowers the magnitude of the spatial inhomogeneity in a saturated inversion profile as excited states migrate from spatial gain anti-nodes to regions where they may be effectively depleted by the first oscillating mode. If excited state migration is present then the effect is to increase the observed values for the $\zeta(1,13)$ factor. A pump density dependent excited state migration mechanism in LNP has been observed by Otsuka and Kubodera [22,23]. They postulate that this mechanism is an Auger-type recombination process [20-23,38] where two excited ions in close proximity interact such that the energy of one excited ion is lost. Clearly the higher the pump power density the higher the excited ion density and the higher probability of two excited ionsbeing in close proximity. The mechanism by which this process occurs in neodymium is outlined in the simplified partial energy level diagram below.

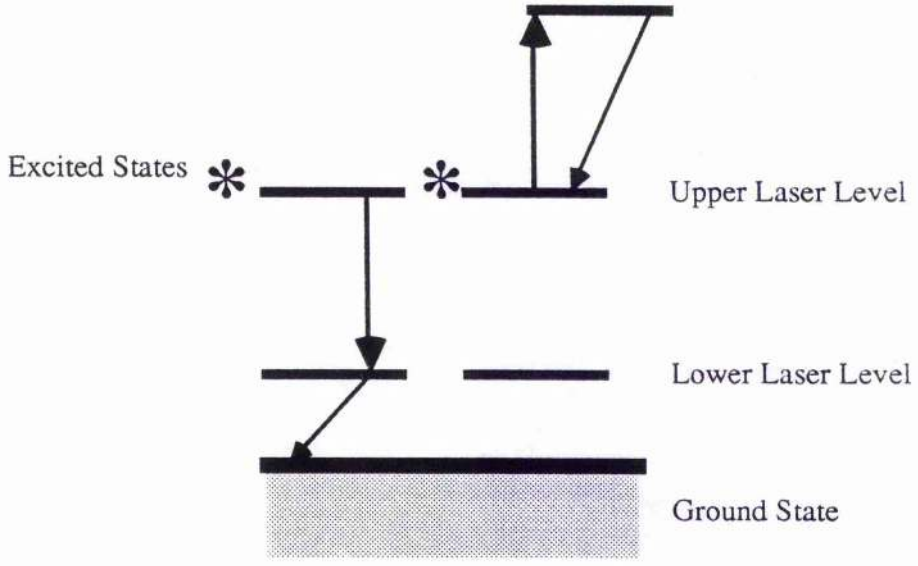

Figure 4.3.4: Auger-Type Recombination of Excited States in the Nd^{3+} Ion
(Thick, Straight Arrows: Lasing Transitions)
(Thin, Slanted Arrows: Non-radiative Transitions)
The Hatching Indicates the Ground State Manifold

In neodymium the two states are $^4F_{3/2}$ excited states which combine to create one excited state in the $^2G1_{9/2}$ level which relaxes non-radiatively into the $^4F_{3/2}$ level again. This effect however will reduce the gain present in a solid-state laser as the energy of one exciton is lost in the recombination process as is borne out by figure 4.3.4. One

particular effect, in LNP, which has been described by Otsuka is the effect of Auger-type recombination on relaxation oscillation decay [20-23,39,40]. According to the standard rate equation analysis in the small-signal regime the spiking train from a single frequency, solid-state laser should follow the relation.

$$I(t) \propto \exp(-t/\tau_d)\sin\omega t \qquad \text{Eqn. 4.19}$$

τ_d is a damping constant describing the exponential decay of the train of pulses of angular frequency ω. The damping constant is given by [39,40].

$$\tau_d = \frac{2\tau_f}{w} \qquad \text{Eqn. 4.20}$$

t_f is the upper state lifetime of the material (120 μs for LNP [28]) and w is the number of times above threshold at which the laser is being pumped. The diffusion of excited states by means of Auger-type recombination increases the gain available to the first mode above that provided by pump excitation. Therefore the pump rate for the first mode is increased by the effective injection of excited states from regions where the inversion is undepleted and is manifested in an envelope around the spiking train which decays more rapidly than the basic rate equation analysis would suggest. In light of experimental results and the elimination of the effect of a reabsorption loss differential we postulate that pump excitation dependent Auger-type recombination was responsible for the observed increased single frequency performance of the LNP microchip laser. To verify this assertion the single frequency spiking behaviour of the LNP microchip laser in the small-signal regime was examined as a function of pump density. The pump density within the material was altered by variation of pump absorption coefficient. The relaxation oscillations were induced by applying a square wave pump pulse from the laser diode with a 50% duty cycle at 1kHz. The figure below shows two typical single frequency relaxation oscillation trains from the device. The upper trace was obtained with the pump tuned so as to access the maximum absorption coefficient of 17.5 mm^{-1} the lower trace was at an absorption coefficient of 6.5 mm^{-1}. For both traces the pumping factor was kept at w=2.1. This ensured single frequency operation of the

device at both absorption coefficients without which it would be impossible to employ the standard rate equation analysis to the spiking train.

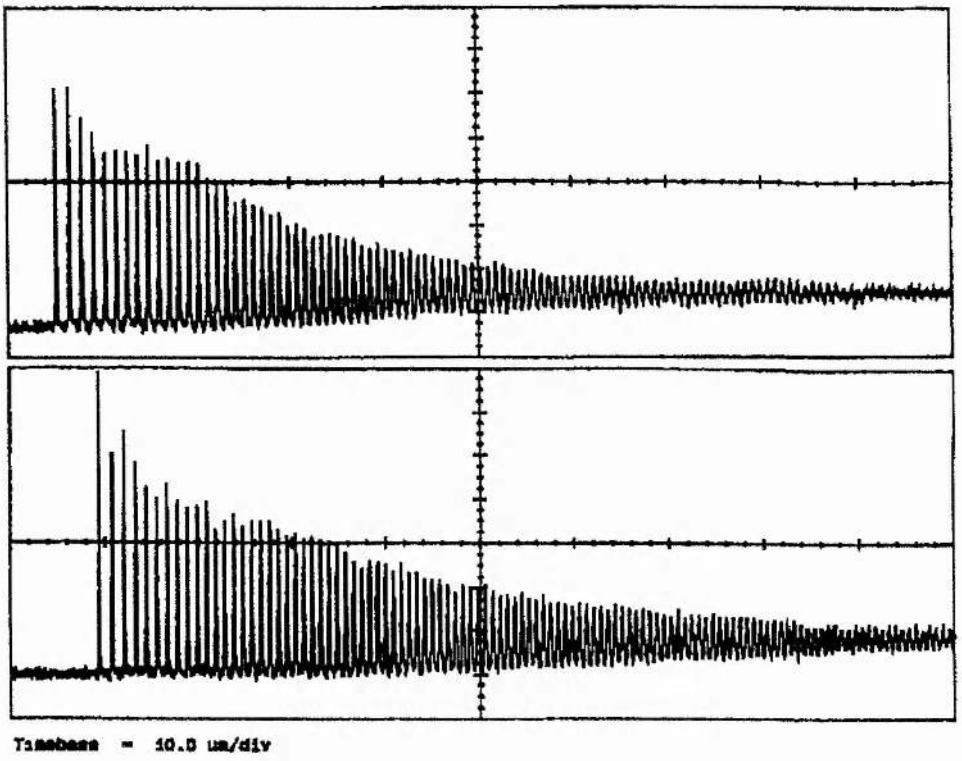

Figure 4.3.5: Relaxation Oscillation Train from Pump Modulated LNP Microchip Laser
(Top Trace: w=2.1, α=17.5 mm^{-1})
(Bottom Trace: w=2.1, α=6.5 mm^{-1})

From the above curves a differential in the damping constant for each train may be seen. For the low absorption case (the lower trace) the value of the constant is τ_d=35 μs. For the high absorption case (the upper trace) the envelope surrounding the spike train decays with a damping constant of τ_d=25 μs.

The excitation density was then varied by altering the pump absorption coefficient over a much wider range of values. It was assumed that the injection of excited states by Auger-type recombination had no effect on the pump rate being used. The standard rate equation analysis was then used to calculate a value for the apparently quenched fluorescence of the material according to equation 4.20.

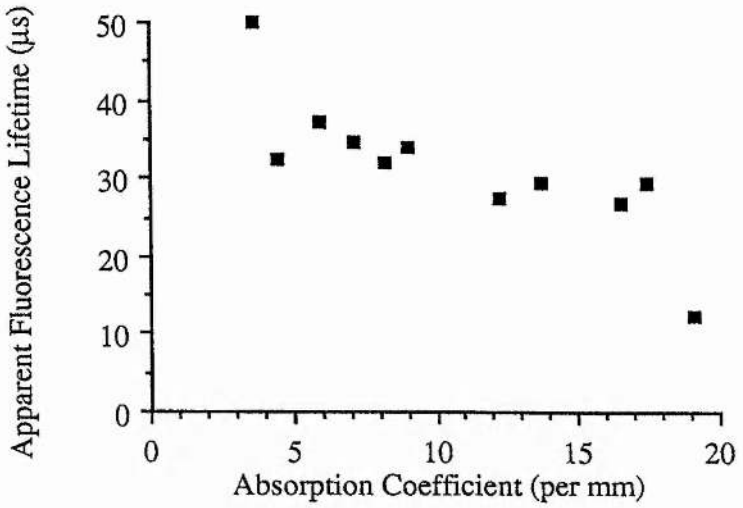

Figure 4.3.6: Apparently Quenched Fluorescence from Decay of Spiking Train in an LNP Microchip Laser as a Function of Gain Length.

From the above figure it is evident that the modification of the pumping rate by excited state migration is increasing with higher pump densities. This would explain the discrepancy between the modelled single frequency behaviour of the device and that observed experimentally as shown in figure 4.3.3. We propose therefore that a pump density dependent, Auger-type recombination process is suppressing the spatial inhomogeneity in the saturated gain profile such that the gain available to the second possible lasing mode in the LNP device is reduced. Therefore the single frequency characteristics of the device are improved over what the calculation of the $\zeta(1,13)$ factor , based on spatial dephasing alone, would imply.

Section 4.4: Conclusions and Summary

A laser diode pumped LNP microchip was demonstrated and characterised. The device produced a maximum of 14 mW of fundamental spatial mode (M^2=1.1) 1.047 μm radiation. The use of a temperature tunable laser diode pump source facilitated the examination of the single frequency characteristics of the device at a variety of gain lengths. Multi-longitudinal mode operation of the device was characterised by excitation of an axial mode under the principal gain bandwidth at 1.047 μm and preferential excitation of an axial mode driven by the adjacent 1.055 μm transition. The

experimental results were then compared with what would be expected from a model based on spatial dephasing of axial modes throughout the gain length. The improvement between the observed results and those expected could not be accounted for by the presence of a temperature dependent reabsorption loss differential between the two modes. The improvement in the single frequency behaviour of the device was therefore postulated as being due to a pump density dependent energy migration process similar to Auger recombination. Further evidence for the existence of a pump density dependent energy migration process was found in the existence of increased damping at shorter gain lengths of the relaxation oscillation train from the LNP microchip laser.

References

[1] Spectra Diode Laboratories, San Jose, Ca., U.S.A., Laser Diode Operators Manual, 1993

[2] N. MacKinnon and B. D. Sinclair, Opt. Comm., **94**, p. 281-288, (1992)

[3] A. Siegman, "Lasers", University Science Books, (1986), p.867

[4] G. J. Dixon, L. S. Lingvay and R. H. Jarman, I.E.E.E. Photon. Tech. Lett., **1**, no. 5, p. 97, (1989)

[5] W. W. Kruehler, R. D. Plaettner and W. Stetter, Appl. Phys., **20**, p. 329-334

[6] J. J. Zayhowski and A. Mooradian, Opt. Lett., **14**, p. 618, (1989)

[7] P. A. Leilabady, D. W. Anthon and P. O. Gullicksen, Paper CM16, Conference on Laser and Electro-optics, (CLEO), 1992, Technical Series Digest, Vol. 11, Optical Society of America, Washington D. C., U. S. A., p. 58

[8] D. W. Anthon, A. T. Eggleston, G. R. Ristau, Paper CM14, Conference on Laser and Electro-optics, (CLEO), 1992, Technical Series Digest, Vol. 11, Optical Society of America, Washington D. C., U. S. A., p. 60

[9] G. E. Stillman, M. D. Sirkis, J. A. Rossi, M. R. Johnson and N. Holonyak, Appl. Phys, **9**, no.7, p.268, (1966)

[10] P. W. Smith, Proc. I.E.E.E., **60**, no.4, p. 422, (1972)

[11] C. L. Tang, H. Statz and G. DeMars, J. of Appl. Phys, **34**, no. 6, p. 2289, (1963)

[12] V. Ehutov and A. E. Siegman, Appl. Opt., **4**, no. 4, p. 142, (1965)

[13] T. Kane and R. Byer, Opt. Lett., **10**, p. 65, (1985)

[14] G. J. Kintz and T. Baer, I.E.E.E. J. of Quant. Electron., **QE-26**, no. 9, p. 1457, (1990)

[15] H. G. Danielmeyer, J. of Appl. Phys, **42**, no. 8, p. 3125, (1971)

[16] T. Kimura, K. Otsuka and M. Saruwatari, I.E.E.E. J. of Quant. Electron., **QE-7**, no. 6, p. 225, (1971)

[17] J. J. Zayhowski, Opt. Lett., **15**, no. 8, p. 431, (1990)

[18] J. J. Zayhowski, I.E.E.E. J. of Quant. Electron., **QE-26**, no. 12, p. 2052, (1990)

[19] L. W. Casperson, Appl. Opt., **19**, no. 3, p. 422, (1980)

[20] H. G. Danielmeyer and M. Blaette, Appl. Phys, **1**, p. 274, (1973)

[21] K. Otsuka, I.E.E.E. J. of Quant. Electron., **QE-13**, no. 7, p. 520, (1977)

[22] K. Otsuka and K. Kubodera, I.E.E.E. J. of Quant. Electron., **QE-16**, no. 4, p. 419, (1980)

[23] K. Otsuka and K. Kubodera, I.E.E.E. J. of Quant. Electron., **QE-16**, no. 5, p. 538, p. 538, (1980)

[24] A. Siegman, "Lasers", University Science Books, (1986), p. 292

[25] A. Yariv, "Quantum Electronics", Third Ed., Wiley, (1989), p. 176

[26] O. Svelto, "Principles of Lasers", Plenum Press, (1976), p. 54

[27] A. Yariv, "Quantum Electronics", Third Ed., Wiley, (1989), p. 402

[28] K. Otsuka, T. Yamada, M. Sarawatari and T. Kimura, I.E.E.E. J. of Quant. Electron., **QE-11**, no. 7, p. 330, (1975)

[29] N. MacKinnon and B. D. Sinclair, Opt. Comm., **95**, no. 1, (1994)

[30] T. Sasaki, T. Kojima, A Yokotani, O. Oguri and S. Nakai, Opt. Lett., **16**, p. 1665, (1991)

[31] W. P. Risk, J. of Opt. Soc. of Am. B, **5**, no. 7, p. 1412, (1988)

[32] K. Otsuka and T. Yamada, Opt. Comm., **17**, no. 1, p. 24, (1976)

[33] K. Otsuka, I.E.E.E. J. of Quant. Electron., **QE-17**, no. 6, p. 49, (1978)

[34] J. Hong, B. D. Sinclair, W. Sibbett and M. H. Dunn, Appl. Opt., **31**, no. 9, p. 1318, (1992)

[35] R. W. Wallace and S. E. Harris, Appl. Phys. Lett., **15**, no. 4, p. 111, (1969)

[36] T. Y. Fan and R. L. Byer, Opt. Lett., **12**, p. 809, (1987)

[37] O. Svelto, "Principles of Lasers", Plenum Press, (1976), p. 5,62

[38] J. S. Blakemore, "Solid-State Physics", Second Edition, Cambridge, p. 384-386, 391, (1985)

[39] R. Dunsmuir, J. of Electron. Control, **10**, p. 453, (1963)

[40] A. Siegman, "Lasers", University Science Books, (1986), p. 963

Chapter 5: A Laser Diode Array Pumped, Composite Material Microchip Laser for Frequency Up-conversion

Introduction

The composite material frequency doubled microchip laser was originally conceived at St. Andrerws, as an extension of the microchip laser concept into the realm of non-linear optics and miniature, visible solid-state lasers. The frequency doubled device was envisaged as consisting of a thin slice of gain material in intimate optical contact with a thin slice of non-linear material for frequency up-conversion. The implementation of this concept, which has since yielded a uniquely compact source of 100 mW of green radiation, will be discussed in this chapter. Firstly, the properties of the chosen gain material neodymium-doped yttrium orthovanadate (Nd:YVO_4) will be outlined with special emphasis on the suitability of this material for diode pumping configurations and its advantages over neodymium doped yttrium aluminium garnet (Nd:YAG) and neodymium-doped yttrium lithium fluoride (Nd:YLF) in this respect. Then the rationale behind the selection of potassium titanyl phosphate (KTP) as the frequency doubling crystal will be explained as will the frequency doubling and physical properties of the material which make it eminently suitable for this device concept. The method of fabrication of the composite cavity will then be outlined. The completed device is then fully characterised when pumped by a half-Watt laser diode array via coupling optics. The characteristics of the device when pumped directly from the facet of the half-Watt array are then discussed in the context of excitation using higher brightness laser diode arrays.

Section 5.1: Properties of Neodymium Doped Yttrium Orthovanadate (Nd:YVO_4)

Neodymium-doped yttrium orthovanadate, hereafter Nd:YVO_4, was first identified as a possible laser material in 1967 by O' Connor [1] who observed a stimulated emission cross-section at 1.064 μm significantly larger than that in neodymium doped yttrium

aluminium garnet, Nd:YAG, and also achieved pulsed lasing of the 1.064 μm line in Nd:YVO_4 at 90 K. However, formidable growth problems associated with the material seriously inhibited further, more detailed, studies until the early seventies when DeShazer et al. [2,3] developed improved growth techniques for Nd:YVO_4 thus allowing the first comprehensive spectroscopic characterisation. The work performed by DeShazer and his co-workers clearly identified Nd:YVO_4 as a highly promising candidate for selection as a solid-state gain material. Further improvements in growth techniques for Nd:YVO_4 coupled with the advent of laser diode pumping of solid-state media has stimulated great interest in Nd:YVO_4, with its higher gain and broader absorption, as a more attractive replacement for Nd:YAG in low and medium power lasers.

It is useful now to consider the lasing and thermal characteristics of Nd:YVO_4 in comparison with Nd:YAG and neodymium doped yttrium lithium fluoride (Nd:YLF). In particular the implications of replacing Nd:YAG with Nd:YVO_4 in commonly used laser devices will be discussed as will the suitability of each material for diode pumped applications.

From figure 5.1.1 below it is worthwhile to note the following features of Nd:YVO_4 which make it a strong contender for applications in which Nd:YAG may already dominate.

(i) The emission and pumping wavelengths of Nd:YVO_4 are very similar to those of Nd:YAG. Consequently, YVO_4 may directly replace YAG in current laser systems without need for replacement of existing laser diodes as pump sources or non-linear crystals for up-conversion or intensity modulation. The advantages of the synergy between Nd:YAG and Nd:YVO_4 is further extended when the volume production of optics, coated for implementation in 1.064 μm systems, is considered.

(ii) The emission of Nd:YVO_4 is very strongly linearly polarised along the crystal c-axis which may facilitate efficient frequency conversion or intensity modulation of the

$Nd:YVO_4$ laser output without the need for additional intracavity elements to force linear polarisation within the cavity. Similarly the strongly linear polarisation of the output is desirable for many extra-cavity modulation or doubling processes.

Physical Characteristic	**$Nd:YVO_4$**	**Nd:YAG**	**Nd:YLF**
Crystal Class	uniaxial	isotropic	uniaxial
Doping Limit (at. %)	3	1.6	2
Lasing Wavelength of Principal Transition (nm)	1064.3	1064.2	1047
Polarised Emission	yes	no	yes
Linewidth of Principal Transition (nm) (Full-width Half-maximum)	0.8	0.6	1.21
Radiative Lifetime (μs)	115 (1% doping) 50 (3% doping)	255 (1% doping)	520 (1% doping)
$\sigma_{em}.\tau_f$ Product (10^{-23} cm^2 s)	17.94 (1 % Doping) 7.8 (3 % Doping)	8.0 (1 % Doping)	9.7 (1 % Doping)
Pump Wavelength (nm)	808.6	807.5	793
Full-width Half-maximum of Absorption Band (nm)	8	1	3
Peak Absorption Coefficient (mm^{-1})	3 (1% doping) 11.1 (3% doping)	1 (1% doping)	1 (1% doping)
Sign of dn/dT	Positive	Positive	Negative
Thermal Conductivity (Wm^{-1} K)	5.2	10	4.3

Figure 5.1.1: Properties of $Nd:YVO_4$ in Comparison with Nd:YAG and Nd:YLF (after [4])

(iii) The width of the absorption band of Nd:YVO_4 about the pump wavelength is much larger than in YAG which reduces the constraints set upon the temperature stabilisation of the laser diode pump source.

(iv) In this respect, as may be seen from the data for the high doped Nd:YVO_4, much higher absorption coefficients may be exploited than in Nd:YAG or in Nd:YLF. Not only will this lead to an overall increase in the efficiency of the device for a given pump source but also, as was seen in the previous chapter, improves the single frequency characteristics of a device of a fixed intracavity mode spacing.

(v) As may be seen for the $\sigma_{em}.\tau_f$ product, which has been used as a figure of merit to express the optical gain present in a solid-state laser material [5], Nd:YVO_4, even in the presence of fluorescence quenching [6] at higher active ion concentrations, exhibits a larger optical gain than Nd:YAG or Nd:YLF.

(vi) In addition to the properties listed above Nd:YVO_4 has a very clean π-polarised emission spectrum in the vicinity of 1.064 μm.

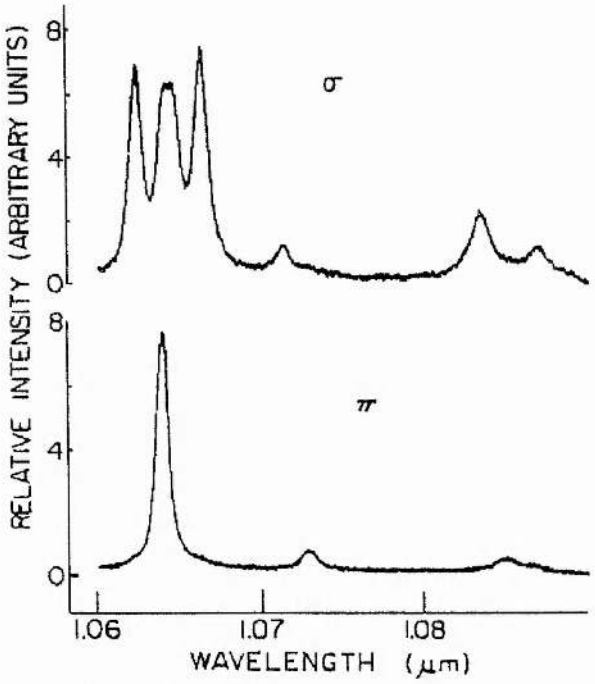

Figure 5.1.2: π and σ-polarised Fluorescence Spectra of Nd:YVO_4 in the Vicinity of 1.064 μm (after [2])

The Fluorescence Spectra for the σ-polarised Emission (Top Curve) is on an

Intensity Scale One Fifth of That for the π-polarised Emission (Bottom Curve)

This is in contrast to Nd:YAG which has a transition at 1.061 μm of comparable strength to the more familiar transition located at 1.064 μm [2]. In a Nd:YAG 1.064 μm microchip laser particular care has to be taken in selecting the cavity length to ensure that one longitudinal mode of the device is at the peak of the principal transition while other axial modes straddle the secondary peak.

Considering in detail the mechanical and spectroscopic properties of the three materials it is evident that Nd:YVO_4 does have a slightly lower thermal conductivity than would be desired but this may be compensated for by more aggressive heat sinking techniques for higher power lasers. However like Nd:YAG the dn/dT quantity is positive and, knowing that a positive dn/dT can support the appropriate cavity stability mechanisms [7,8], this makes Nd:YVO_4 an immediate candidate for configuration as a microchip laser. Nd:YLF on the other hand exhibits a negative dn/dT combined with relatively longitudinally uniform pump power deposition which has not been proven as a regime where pump induced cavity stability would be exhibited in a microchip laser format over a wide range of pump powers [7-10].

Section 5.2: Criteria for Selection of Frequency Doubling Material for Composite Material Microchip Laser

In the design consideration of the composite material doubled microchip laser the following criteria were identified as pertinent to the selection of an appropriate doubling crystal for the chosen gain material.

(i) The non-linear material should have firstly a suitably large non-linear coefficient and sufficient birefringence to facilitate phase matching for the envisaged frequency upconversion. Secondly, the material should exhibit excellent transparency at the appropriate wavelengths.

(ii) The material should be configured such that phase matching would be critical by either a type I or type II interaction [11-20]. Despite the advantages of non-critically phase-matched-doubling (hereafter NCPM) techniques [19], namely access to a reasonably high non-linear coefficient without walk-off between the propagating fundamental and second harmonic [19,20] the issues involved with NCPM can be significant. The use of the non-linear material magnesium doped lithium niobate ($MgO:LiNbO_3$) is a case in point. The use of type I NCPM magnesium doped lithium niobate allows access to a non-linear coefficient of $|d_{31}| = 4.7$ pm V^{-1} but may only phase-match 1.064 μm radiation appropriately at an elevated crystal temperature of approximately 110 ^{0}C. Clearly not only is this cumbersome to achieve in practice but the elevated operating temperature of the intimately contacted gain material may lead to undesirable increases in reabsorption losses in the material due to a finite lower laser level population [21-23] .

(iii) If the use of NCPM techniques is undesirable then the non-linear material, in whatever the chosen critically phase-matching configuration should have as small a walk-off angle as possible. This would ensure that for the pump induced confined eigenmode waist significant reductions in conversion into the second harmonic due to walk-off would be avoided.

(iv) The non-linear material as configured should have a wide temperature bandwidth for the phase matching process so as to make the frequency upconverted output power of the device as insensitive as possible to ambient temperature fluctuations and transference of pump induced heating effects in the gain material. Similarly the acceptance angle of the phase matching process should be as large as possible so as to minimise the criticality in the cutting of the raw material at the correct angle. In addition a wide angular acceptance bandwidth means that if during polishing of the material, after it has been cut appropriately, any change in the angle of propagation through the material results in the smallest possible reduction of second harmonic output.

(v) The frequency-doubling crystal should have excellent mechanical and physical properties. Especially the material should be non-hygroscopic and be readily workable so as to produce a piece of comparable optical parallelism to that present in the gain material. Additionally the material should exhibit an appropriately high damage threshold to allow application in this intra-cavity frequency doubled application where the material may be subjected to high circulating optical field densities.

(vi) The chosen doubling crystal exhibiting the best combination of the above properties must be readily available at low cost in the desired orientation, ultimately, in volume quantities commensurate with future "OEM" applications for the frequency doubled device in mind. Preferably the material should already have a proven track record with frequency upconversion of 1.064 μm radiation from larger neodymium lasers.

Considering the above restrictions on the choice of the non-linear doubling material the doubling crystal finally chosen for implementation in the frequency doubled microchip laser was the ubiquitous potassium titanyl phosphate ($KTiOPO_4$ or KTP) angle-cut so as to allow a type II second harmonic generation process near room temperature.

Section 5.3: Frequency Doubling and Physical Properties of Potassium Titanyl Phosphate (KTP)

During the immediate aftermath of the invention of the laser considerable interest devolved on the development of crystals exhibiting second order optical non-linearity for the manipulation of the newly discovered laser radiation. The class of materials which were seen to be the most promising and technically feasible group were the oxygen-octohedra ferroelectrics including KTP [11-20]. Additional members of this class included $LiNbO_3$, $KNbO_3$, LIO_3 amongst others [11-20]. Most of the technical difficulties associated with the growth of KTP were overcome in the mid-nineteen seventies at Airtron and duPont de Nemours and since then KTP has virtually superseded all the earlier doubling crystals in doubling 1.064 μm radiation from low and

medium power neodymium lasers. In addition to second harmonic generation of 1 μm radiation KTP has also been widely used as the non-linear element in various sum-frequency and parametric interactions over the its entire transparency range from 0.35 μm to 4.5 μm.

Potassium titanyl phosphate is a biaxial [15,16,19,20] crystal belonging to the orthorhombic point group mm2 [20] with lattice parameters a=1.2814 nm, b=0.6404 nm and c=1.0616 nm. The set of piezoelectric axes X,Y and Z may be related easily to the crystallographic axes in this class of material [24]. The three mutually perpendicular crystallographic axes a, b, and c transfer directly to the piezoelectric axes X, Y and Z respectively. It has been shown that the refractive indices of KTP permit both type I and type II second harmonic generation interactions of 1.064 μm fundamental radiation [14-16,19,20]. Specifically, the conditions for phase matching in the two interactions possible and the corresponding effective non-linear coefficients have been examined by both Ito et al. [14] and Yao and Fahlen [20]. The expressions for the effective non-linear coefficient, $d_{eff.}$, in the two possible interactions are,

$$d_{eff.}(\text{type I}) = \frac{1}{2}\left[(d_{15} - d_{24})\ \sin 2\theta \sin 2\phi\right] \qquad \text{Eqn. 5.1}$$

$$d_{eff.}(\text{type II}) = (d_{24} - d_{15})\ \sin 2\theta \sin 2\phi - \left(d_{15}\sin^2\phi + d_{24}\cos^2\phi\right)\ \sin\theta \qquad \text{Eqn. 5.2}$$

In the above equations the angle ϕ is the angle between the direction of propagation of the fundamental ray and the X axis of the KTP. The angle θ is the angle between the fundamental ray propagation direction and the Z axis. The effective non-linear coefficient, $d_{eff.}$, for type I SHG (second harmonic generation) of 1.064 μm radiation is much smaller than that for a type II interaction. The maximum value for $d_{eff.}$ for the type I SHG case is approximately one seventh of the maximum for the type II interaction [19,20]. However, the lower wavelength limit over which a type II SHG interaction may be exploited is dictated by the birefringence of the material and is

approximately 0.99 μm [20]. This excludes therefore doubling of short wavelength laser sources with KTP in this configuration.

The appropriate propagation angle in the KTP X-Y plane for the fundamental 1.064 μm radiation, relative to the KTP X-axis, has been computed to be 23.3^0 [16,19,20]. This direction of propagation utilises the largest possible value of effective non-linear coefficient which, as calculated from the known values present in the second order non-linear polarisability tensor by Fan et al. [20], is 7.5 pm V^{-1}. The orientation of the KTP doubling crystal used is shown in the figure below.

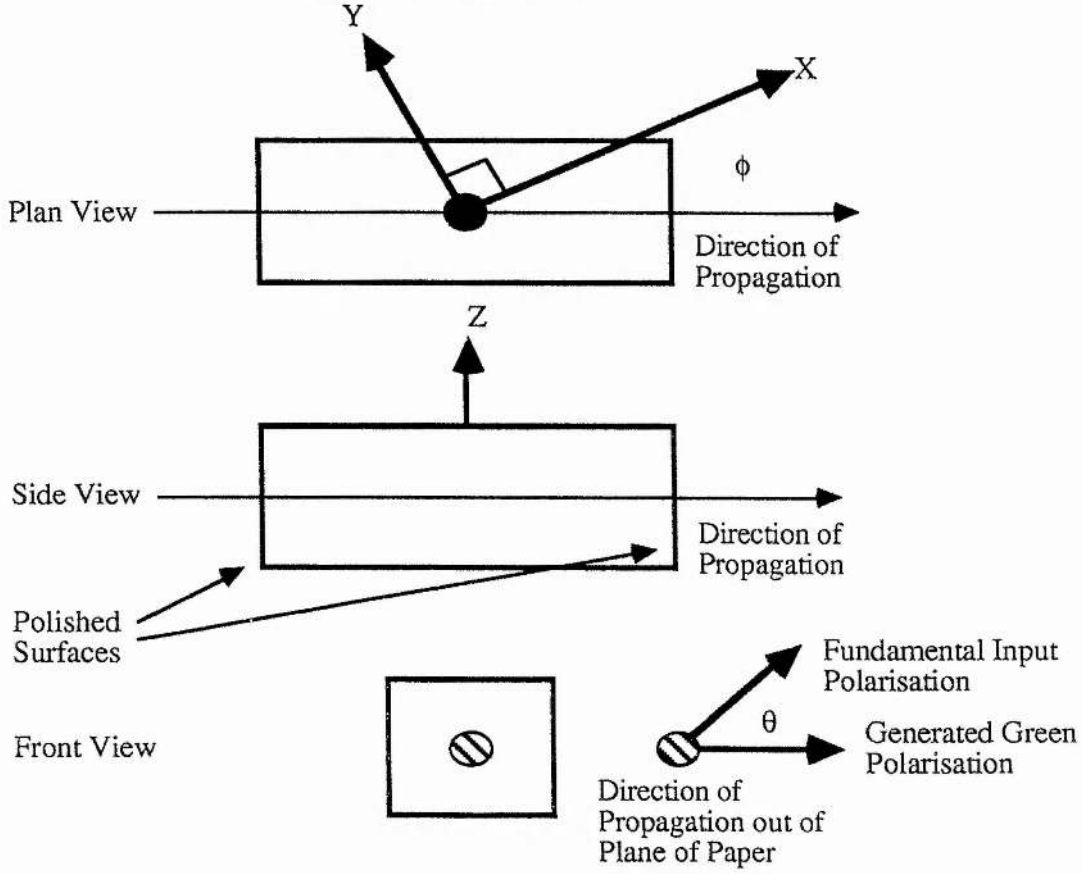

Figure 5.3.1: Orientation of KTP Material for Doubling of 1.064 μm Radiation

Piezoelectric Axes are Listed as X, Y and Z,
The Angle Between the Input Fundamental Polarisation and
Generated Green Polarisation is $\theta=45^0$
The Angle Between the Direction of Propagation of the Fundamental and
the KTP x axis is $\phi=23.3^0$

Despite being a widely used material for frequency doubling the currently accepted values for the non-linear coefficients present in the second order polarisability tensor are still a subject of controversy for KTP [19,20]. To ascertain the definitive value of $d_{eff.}$ for the SHG process at 1.064 μm in KTP and other materials Eckardt et al. [19] performed a set of rigorous SHG experiments. The effective non-linear coefficient for the SHG process in KTP as obtained from these absolute measurements yielded a value of $d_{eff.}$ = 3.2 pm V^{-1} +/- 6%. This experimental value for $d_{eff.}$ for KTP is approximately half that expected as calculated from the currently accepted values present in the non-linear polarisability tensor . The main properties of KTP are listed below in comparison with some comparable materials used in SHG of 1.064 μm radiation. In the table below the effective non-linear coefficient listed is for second harmonic conversion of 1.064 μm fundamental radiation. In the selection of materials below KTP is the only biaxial crystal the rest being uniaxial [12,13,15,19,20]. MgO:$LiNbO_3$ is the only material that is temperature tuned to T=110^{0}C to achieve phase-matching the rest being angle-tuned for phase-matching at room temperature.

Material	**Crystal Class**	**SHG Inter-action**	**Phase-match Angle (Degrees)**	**$\|d_{eff.}\|$ (pm/V)**	**Walk-off Angle (Degrees)**
KTP	Biaxial	Type II	23.3	3.2	0.22
KDP	Uniaxial	Type I	41.2	0.32	1.6
KD*P	Uniaxial	Type I	36.6	0.37	1.45
BaB_2O_4	Uniaxial	Type I	22.8	1.94	3.19
LiO_3	Uniaxial	Type I	30.2	4.1	4.3
MgO:$LiNbO_3$ (5% MgO)	Uniaxial	Type I	90 T=110^{0}C	4.7	0

Figure 5.3.2: Properties of KTP Relative to Comparable Materials for SHG of 1.064 μm Radiation (after [12])

The above figure shows succinctly the advantages of KTP as the frequency doubling material for this application. The table below expresses a figure of merit, $\delta=(d_{eff.})^2/n^3$, for each of the angle-tuned materials listed above. Clearly what is desired in this application is an angle-tuned non-linear material with a reasonably high effective non-linear coefficient with the lowest possible value of walk-off. The figure of merit used here is simply the product of the effective non-linear coefficient, squared, divided by the refractive index cubed and is indicative of the conversion efficiency of each material.

Material	Figure of Merit, δ, $(pm/V)^2$
KTP	1.91
KDP	0.7
KD*P	0.72
BaB_2O_4	1.03
LiO_3	0.95

Figure 5.3.3: Figure of Merit, δ, for KTP and Comparable Non-linear Materials

In addition to the properties outlined above the temperature bandwidth for the SHG process in KTP is 25 ^{0}C cm which is 4 times that for KD*P and MgO:$LiNbO_3$ [12].

Section 5.4: Fabrication of Composite Material Microchip Laser Cavity

The composite cavity device was fabricated from an etalon of solid-state laser material , which provided optical gain at 1.064 μm, bonded using index matching fluid to a non-linear element to provide frequency up-conversion into the visible. The active ion concentration of the a-axis cut Nd:YVO_4 gain material was chosen to be nominally 3 % so as to allow both efficient pump absorption and ensure as rapid as possible decay of the gain along the cavity axis. As was shown in the previous chapter this short gain length would increase the spatial competition between longitudinal modes for the same population inversion. Ideally, the optimum length for the Nd:YVO_4 gain material would be no more than that giving approximately 90 % pump absorption. For the 3 % material

obtained from ITI Electro-optics Corp. the absorption coefficient for c-polarised pumping with a laser diode array was found to be α=11 mm^{-1} which would imply a near total pump absorption over 300 μm. However it was not feasible to produce such thin etalons of Nd:YVO_4 gain material to the degree of optical parallelism required and the length of the gain section fabricated was 0.5 mm. The parallelism of the finished etalon of Nd:YVO_4 gain material is shown below. The interferogram shown below was obtained using the Fizeau interferometer as used in chapter 2 and chapter 3 (see figure 2.4.1). As may be seen from the interferogram the Nd:YVO_4 gain material exhibited an area of good parallelism in the upper right hand part of the crystal aperture. Both surfaces of the Nd:YVO_4 gain material were polished to laser quality standards. The Nd:YVO_4 gain material was coated on one side so as to be as highly reflecting as possible at the fundamental wavelength (> 99.8 % R @ 1.064 μm) and as transmissive as possible at the second harmonic wavelength (< 10 % R @ 532 nm).

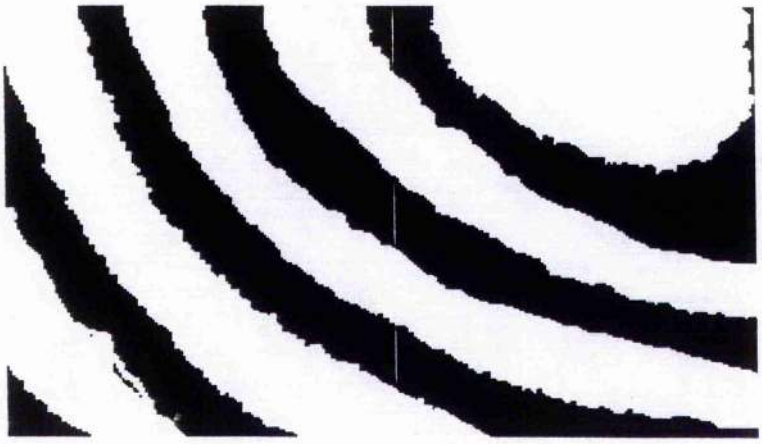

Figure 5.4.1: Optical Parallelism of Nd:YVO_4 Gain Material The Crystal c-axis is Parallel to the Long Axis Which in the Above Figure is 4 mm Long the Other Being 3 mm.

In addition to the desire for increased pump to output efficiency and better spectral characteristics the relatively high concentration Nd:YVO_4 gain material was chosen to optimise the conversion into the second harmonic. It may be shown that the amount of conversion into the second harmonic in a frequency doubling material is inversely proportional to the area of the fundamental beam [25]. For 3 % material the 1/e folding distance for the pump decay is 91 μm at peak absorption as opposed to 330 μm for

nominal 1 % doping in YVO_4 and 1 mm for 1 % Nd^{3+} in YAG [26]. Therefore the thermally induced refractive index profile in the gain material will be more localised both longitudinally and transversely for the high doped Nd:YVO_4 gain material than for the low doped material. Therefore the size of the confined eigenmode will be smaller in the 3 % material than in the 1 % material thus yielding more efficient conversion into the second harmonic within the non-linear material. Sasaki et al. [27] in their study of laser-diode-array-pumped Nd:YVO_4 semi-monolithic devices observed a reduction of one half in the oscillating mode size between nominal 1 % material and nominal 2.02 % material. The issue of what exactly are the pump dependent transverse mode definition processes in Nd:YVO_4 is still unresolved. A Nd:YVO_4 microchip laser exhibits operating features common with two other microchip lasers. The first is that in common with Nd:YAG Nd:YVO_4 has a positive dn/dT [4]. Therefore a thermally induced waveguide may be responsible for confining a lowest order spatial mode as in Nd:YAG microchip lasers [7,8]. The other feature of Nd:YVO_4, as has been mentioned above, is its strong pump absorption [26]. The peak figure of 11 mm^{-1} for the absorption in Nd:YVO_4 is not dissimilar to the peak figure of 18 mm^{-1} for diode pumping of lithium neodymium tetraphosphate (LNP) [28]. The cavity stability mechanisms present in Nd:YVO_4 may therefore, by analogy with the LNP stability mechanisms, rely on an element of input surface curvature to create a geometrically stable cavity. The reliance on input surface curvature in Nd:YVO_4 microchip lasers may also possibly increase with increasing absorption coefficients. In practice it is highly likely therefore that the actual stability mechanisms present are a blend of both input surface curvature and a more distributed positive duct depending on the localisation of the pump radiation.

The selected frequency doubling material, KTP, was chosen to be nominally 2 mm thick. The first reason was the desire to fabricate a monolithic cavity of a length which would be stable under the as yet unknown cavity stability regime. The second reason was to produce a device which would produce coherent green radiation but still be reasonably insensitive to ambient temperature fluctuations. From the listed value of the temperature bandwidth for the SHG process in KTP [12] the expected temperature rise

needed to reduce the amount of green power by 50 %, for a given fundamental power, would be 125 degrees for the 2 mm KTP piece and 250 degrees for the 1 mm piece. Although the temperature of the Nd:YVO_4 gain material during operation is hard to gauge and it will transfer some of its heat to the KTP via heat flow through the index matching fluid the device as a whole will not experience ambient temperature fluctuations of this order in the laboratory. The final stricture on the length of the KTP material was the need to keep the length of the cavity down so as to obtain reasonably good spectral purity in the device output. The guide for the selection of the KTP length was the modelling done in chapter four on a microchip laser's performance as a function of cavity length and absorption coefficient. This modelling is presented in figure 4.2.6 and as may be seen from this figure a cavity length of the order of 2 mm still yields a reasonable value of $\zeta(1,2)$ but was expected to provide reasonable amounts of second harmonic conversion.

All the KTP etalons were fabricated to the same exacting parallelism specifications as the Nd:YVO_4 pieces. The parallelism of the nominally 2 mm thick piece is shown in figure 5.4.2.

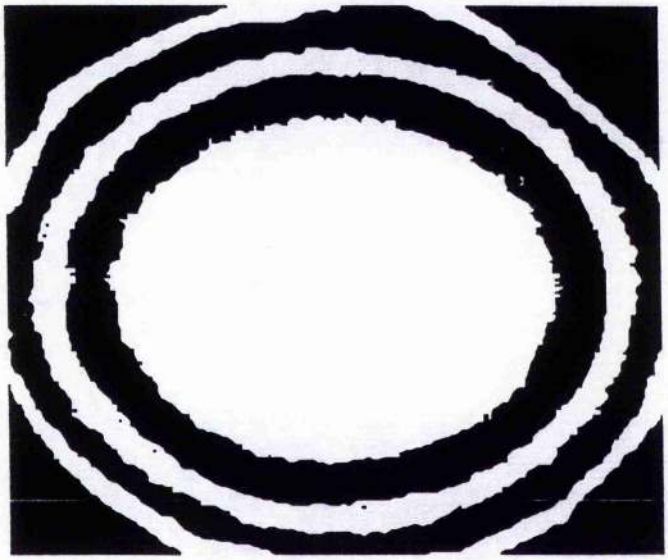

Figure 5.4.2.: Optical Parallelism of Nominally 2 mm Thick KTP Piece. The Piece Shown Above has an Aperture 5 mm by 5 mm in Cross-section. The Fundamental Beam Propagates into the Plane of the Paper with a Polarisation Direction 45 Degrees to the KTP Edges.

As may be seen from figure 5.4.2 the 2 mm KTP etalon exhibited an area of excellent parallelism in the middle of the crystal aperture. The remaining KTP pieces were worked to a similarly high standard. The KTP was coated on one side to as to be highly reflecting at the lasing wavelength (> 99.8 % R @ 1.064 μm) and highly transmissive at the second harmonic wavelength (< 10 % R @ 532 nm). In addition to being highly transmissive at the second harmonic the output surface of the device was specified to have a low reflectivity (<10 % R) at 1.32 μm. This was to ensure that the possibility of parasitic lasing at this longer wavelength was eliminated.

As was outlined above refractive index matching fluid was used between the uncoated surfaces both to bond the two constituent pieces of the device together and reduce multi-cavity effects between the input and output surfaces of the device and both uncoated surfaces. Initially a wide selection of iodo-bromo aromatic hydrocarbon index-matching fluids were purchased with values as high as 1.8 for the refractive index were obtainable using these fluids. This high value for the index matching was obviously much closer to the refractive index both of the Nd:YVO_4 gain material (n=2.2) and the KTP (n=1.75). However these fluids possessed a number of notably disadvantageous properties.

The first major disadvantage was the volatility of some of the high index fluids which evaporated after a few minutes leaving a reddish brown residue on the surfaces of the two components of the device. This instability clearly was a major handicap in the construction of the device. Another deleterious property of these fluids was their strong absorption at the lasing wavelength. The effects of this were twofold. Firstly, with a significant amount of the fluid between the uncoated surfaces lasing was suppressed completely. This could be compensated for to a certain extent by compressing the constituent parts of the device together so as to minimise the amount of fluid present between the uncoated surfaces but the localised heating of the fluid caused by this slight absorbance effectively introduced a weak negative lens within the cavity. This is highly undesirable especially in a microresonator dependent on pump induced stability mechanisms and where everything is done during device fabrication to ensure the best

possible parallelism between the resonator surfaces. The iodo-bromo aromatic hydrocarbons in addition to being not viscous enough to enable the two components to be stuck together permanently were also difficult to handle being an irritant to the skin and when inhaled.

The properties of these unsuitable index matching fluids clearly gave direction to the choice of a more suitable substance. The fluid selected to replace the iodo-bromo aromatic hydrocarbons was a refractive index oil consisting of halogenated long chain hydrocarbons. The fluid was extremely viscous and sticky enough such that the two pieces of the device could be stuck together firmly. The fluid was easy to handle and optically transparent over the appropriate wavelength range. The only disadvantage of this fluid was its relatively low refractive index of 1.41. This value of refractive index meant that on the Nd:YVO_4 gain material/fluid interface there was a residual Fresnel reflectivity of approximately 5 %. Similarly on the fluid/KTP surface there was a Fresnel reflectivity of approximately 2 %. This residual reflectivity would therefore make the fluid interface a weak etalon within the device. However the working advantages of this oil over the other available products outweighed this drawback.

During fabrication of the device a Fizeau interferometer [29] was used to both align the uncoated surfaces of the device to etalon tolerances and ensure that the best area of parallelism on the Nd:YVO_4 gain material was lined up with the best area on the KTP crystal. The c-axis of the Nd:YVO_4 gain material, which is the direction of the polarised emission of the Nd:YVO_4, was aligned appropriately with the axes of the KTP as outlined in figure 5.4.2 and figure 5.3.1. A small amount of the index matching fluid was then placed on one of the two uncoated surfaces. The two constituent parts of the device were then compressed together while every effort was made to maintain the best possible parallelism between the two uncoated surfaces. It was possible to ensure during assembly near perfect optical parallelism across the aperture of the Nd:YVO_4 gain material such that the parallelism between the input and output surfaces of the device was essentially limited by the optical parallelism of the constituent parts of the device.

Figure 5.4.3 below illustrates the structure of the composite material microchip laser consisting of a 500 μm thick Nd:YVO_4 gain section and a 2 mm thick KTP section.

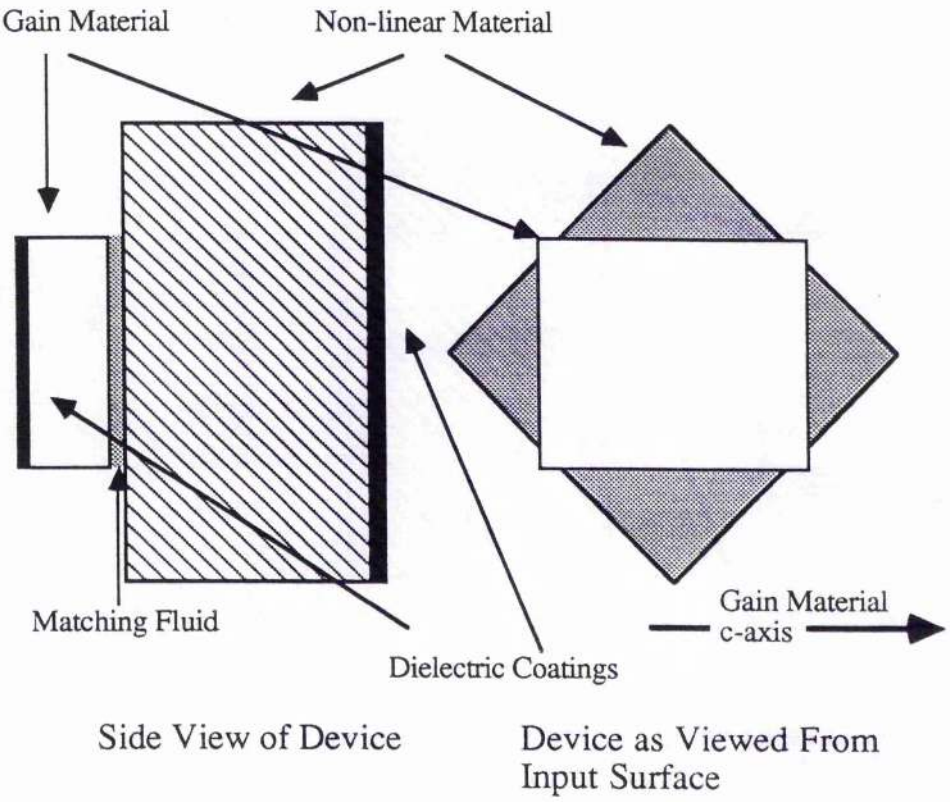

Figure 5.4.3: Structure of Composite Material Microchip Laser

Section 5.5: Characterisation of a Low Pump Power, Lens Coupled Nd:YVO_4/KTP Composite Material Device

Power Performance and Spatial Mode of Operation of Device

A composite material device identical to that shown in figure 5.4.3 was fabricated. The device was excited via coupling optics using a half-Watt SDL-2352-H1 laser diode array. The emitting area of the laser diode was 100 μm x 1 μm. The configuration of the coupling optics was identical to that utilised for diode pumping of the Nd:MgO:$LiNbO_3$ and LNP microchip lasers and may be seen in figure 5.5.1 below.

The spot size produced at the input surface of the composite material device was measured using an apertured scanning photodiode and found to be 120 μm (F.W.H.M.)

in the plane parallel to the laser diode junction and 30 μm (F.W.H.M.) in the plane perpendicular to the laser diode junction. The pumping configuration for the composite device was therefore analogous to coupling of the device closely to the open facet of the laser diode itself. In order to access the strong absorption present in Nd:YVO_4 the Nd:YVO_4 gain material was orientated such that the crystal c-axis was parallel to plane of polarisation of the laser diode emission. The laser diode emission was temperature tuned to the absorption peak in Nd:YVO_4 near 809 nm [4]. The peak absoption coefficient of the nominally 3 % doped material was measured to be 11 mm^{-1}. Therefore over the 0.5 mm length of gain material (which represents approximately four and a half absorption depths) absorption of the incient pump was virtually total.

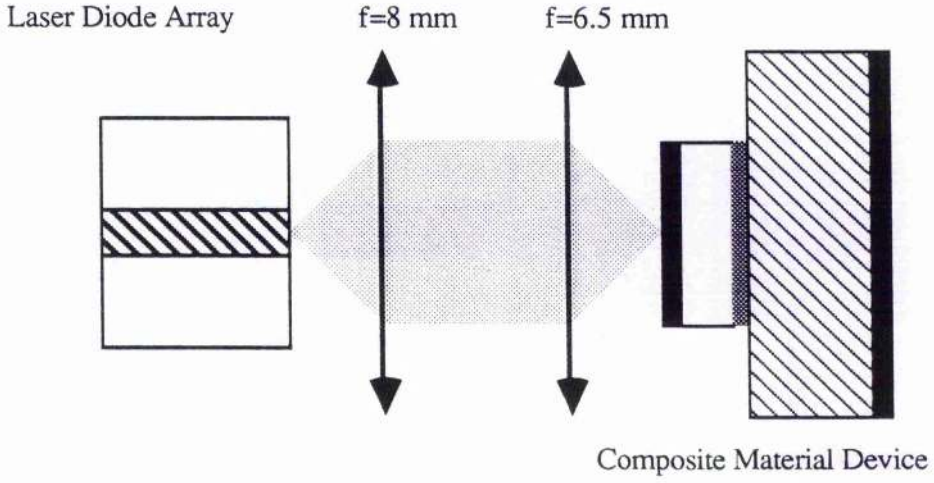

Figure 5.5.1: Pumping Configuration for Frequency Doubled Microchip Laser

The power performance of this low pump power lens coupled device using which initial studies on the behaviour of the composite device were performed may be seen in figure 5.5.2 below.

As may be seen from the figure 5.5.2 the generated green power was more than exceeded by the 1.064 μm power leaking through the highly reflecting coatings. The reflectivity of the coatings on the output surface of the KTP had been measured by the manufacturers to be 99.92 % at 1.064 μm. Therefore the amount of fundamental power leaking through these highly reflective coatings indicates the existence of a large value

of circulating fundamental power (up to 25 W). This value of circulating fundamental flux is therefore indicative of the low parasitic losses within the cavity. The closely linear relation between the fundamental output power and incident pump power also clearly demonstrates that in this pump power regime the non-linear output coupling into the green, as provided by the 2 mm thick KTP element, is relatively low. However the 6 mW of C.W. green output power achieved at approximately 150 mW of incident pump power represented a respectable conversion efficiency of approximately 4 %. The significantly higher green powers achieved utilising "close-coupling" of the device and higher pump powers via coupling optics will be discussed in a forthcoming section of this chapter.

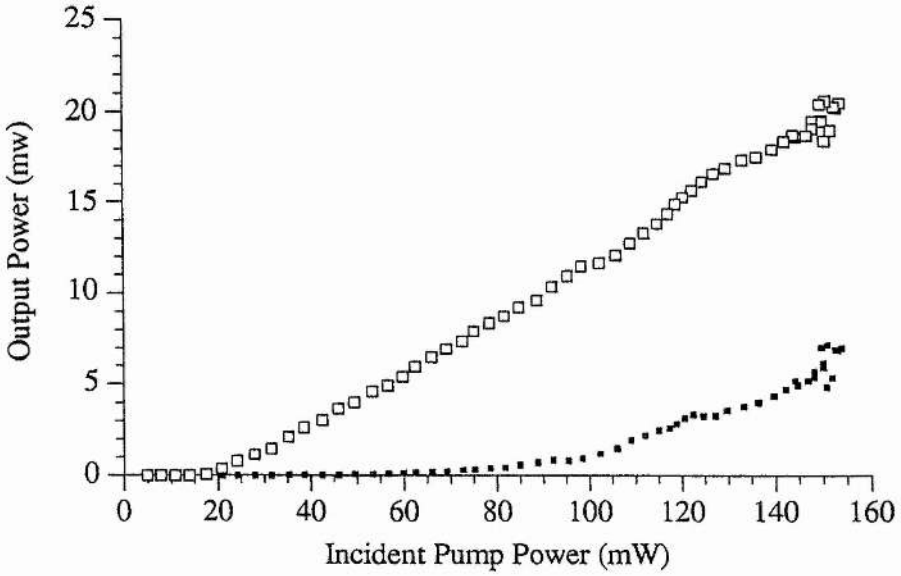

Figure 5.5.2: Performance of Low Pump Power Lens Coupled Composite Material Device (Open Squares; Total Fundamental Power) (Filled Squares; Green Power)

The transverse mode properties of the fundamental output were examined in the far-field. In figure 5.5.3 the spatial mode of the output is shown for pump powers of 53 mW (upper curve) and (lower curve) 153 mW. The far-field intensity cross-sections were found to be very close to being Gaussian; measurements were also performed on the divergence properties of the fundamental at each of these incident powers, which

yielded an M^2 value of 1.1 +/- 9 %. Shown in figure 5.5.4 below are the near field intensity cross-sections of the fundamental beam for the above pump powers as measured at the focus produced by a 20 cm focal length lens.

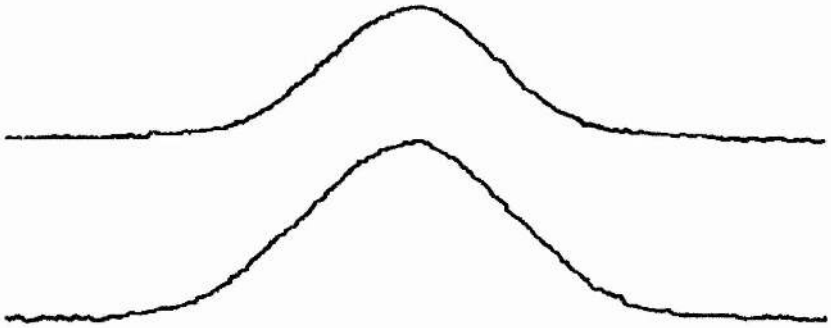

Figure 5.5.3: Far-field Intensity Cross-sections for (top) 53 mW of Pump Power and (bottom) 153 mW of Incident Pump Power

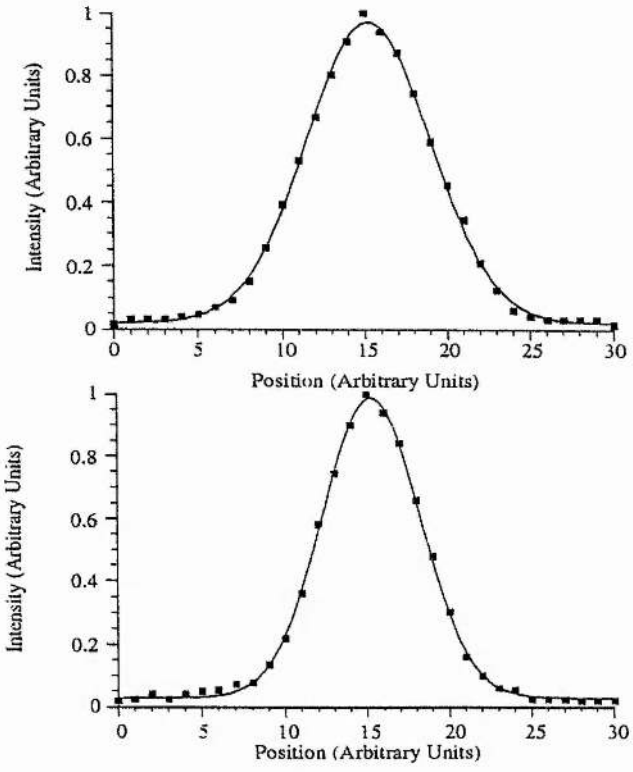

Figure 5.5.4: Near-field Intensity Cross Sections at (top) 53 mW of Incident Pump Power and (bottom) 153 mW of Incident Pump Power.

Super-imposed upon the cross-sections in figure 5.5.4 are Gaussian fits to the obtained points. Clearly the composite material device is operating in the lowest order spatial mode of operation over all the incident pump powers used in these preliminary experiments. The excellent beam quality seen in the fundamental beam was mirrored in the generated green output though stray reflections from the pump optics caused secondary, low intensity spots to appear beside the central lobe.

The divergence of the 1.064 μm output was found to be dependent on the incident power. In figure 5.5.5 this dependence is shown.

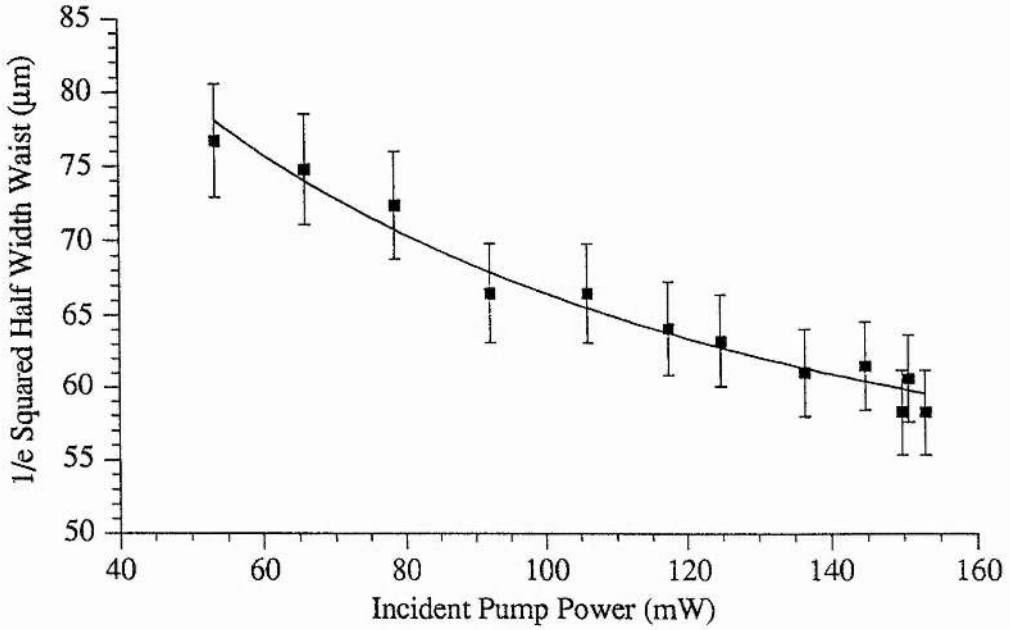

Figure 5.5.5: Oscillating Waist Within Composite Material Device as a Function of Incident Pump Power

The line fit to the points exhibits an inverse fourth root dependence as predicted by Zayhowski's modelling of the thermal guiding processes in Nd:YAG microchip lasers [8]. This may indicate a Gaussian eigenmode confinement mechanism of a similar type to that observed in Nd:YAG microchip lasers although as was discussed above there may be a significant contribution to cavity stability from modification to the microresonator configuration via input surface curvature [7-10]. In many ways the thermal properties and the absorption characteristics of 3 % doped Nd:YVO_4 represent a

cavity stability mechanism between that of LNP and Nd:YAG/Nd:MgO:$LiNbO_3$ microchip lasers [8,30] and undoubtedly merit further experimental and theoretical attention.

The conversion efficiency into the green from the circulating fundamental was studied in detail. The reflectivity of the output surface of the KTP element at 1.064 μm had been measured by the manufacturers to be R=99.92 %. It was possible therefore to calculate easily the amount of circulating fundamental power by measuring the amount 1.064 μm power leaked through the output surface coating. The absolute, experimental value of $d_{eff.}$=3.2 pm V^{-1} as obtained by Eckardt et al. [20] was assumed. Assuming $\Delta k=0$ the oscillating waist size (figure 5.5.5) and cavity field magnitude were then used to calculate the amount of second harmonic light that would be generated as a function of incident pump power. Adopting the conventions appropriate to MKS units [31] the amount of conversion into the second harmonic is given by the equation below.

$$P^{(2\omega)} = 8\left(\frac{\mu_0}{\varepsilon_0}\right)^{3/2} \frac{\omega^2 (d_{eff.})^2 l^2}{\pi \omega_0^2 n^3} \left(P^{(\omega)}\right)^2 \left(\frac{\sin^2(\Delta k l/2)}{(\Delta k l/2)^2}\right) \quad \text{Eqn. 5.3}$$

Where ω is the frequency of the fundamental radiation, $d_{eff.}$ is the effective non-linear coefficient, $P^{(\omega)}$ is the circulating fundamental power, ω_0 is the mode waist size, l is the non-linear crystal length and Δk is the phase mismatch [1-20,31].

The experimental results are shown below in figure 5.5.6 in comparison with the expected values of second harmonic power.

The close agreement between the two sets of results in figure 5.5.6 clearly indicates that the second harmonic power does indeed depend on the square of both the oscillating mode size and the square of the circulating fundamental flux. The small discrepancies between the two sets of results may be due to perhaps the angle cut of the material being slightly different from that necessary to satisfy the phase-matching condition. Another significant source of lower conversion efficiency would be non-optimal fundamental polarisation relative to the KTP piezo-electric axes. The KTP doubling crystal acts

effectively as a multiple order, temperature sensitive waveplate for the oscillating fundamental with n_e-n_o= 0.0865 [27,32]. In addition to the waveplating action in the KTP the Nd:YVO_4 is also birefringent n_e-n_o= 0.21 (n_e=2.17, n_o=1.96) [3,4] and may act as temperature sensitive waveplate.

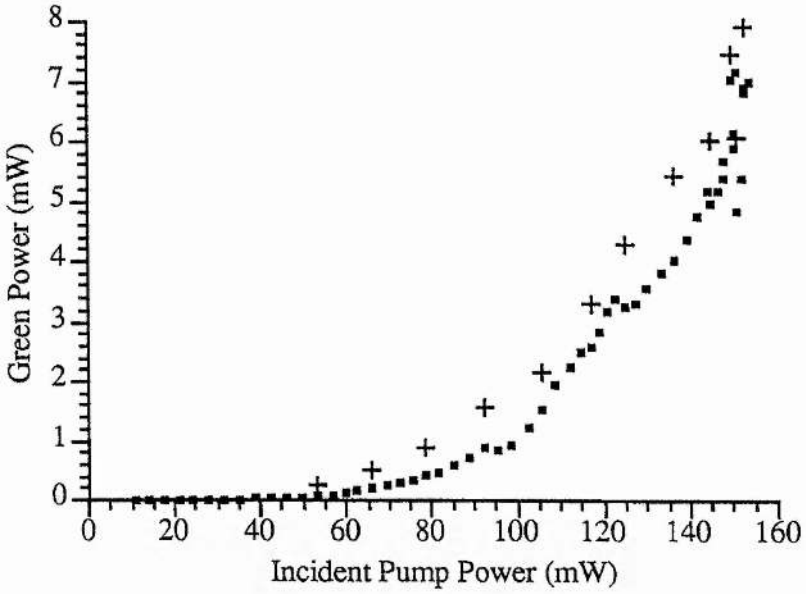

Figure 5.5.6: Experimentally Observed Green Powers (Filled Squares) in Comparison with Second harmonic Powers Expected Theoretically (Crosses).

However the KTP non-linear material is eight times as long as the Nd:YVO_4 material. The amount of phase difference seen in a double pass through either the gain material or the non-linear material is given by [32].

$$\delta = \frac{4\pi\Delta nL}{\lambda} \qquad \text{Eqn. 5.4}$$

Where Δn is the birefringence of the material, L is the length of the material and λ is the wavelength of the circulating fundamental. From the above equation it is evident that what is important is the both the amount of birefringence of the material and its length.

Therefore the waveplating action of the KTP over its length will be approximately three times that present in the Nd:YVO_4.

In larger intra-cavity doubled solid-state lasers which utilised angle-cut KTP as the doubling crystal the presence of the waveplating action of the KTP has normally been eliminated by the insertion of a cavity polarising element to either constrain the cavity eigenpolarisation or to cancel out the waveplating action of the KTP [33,34]. Alternatively, accurate temperature control of the KTP length has been used such that the sum waveplating action of the KTP over one round trip through the cavity is an integral number of π radians. In other words, the KTP would have to act effectively as a $\lambda/2$ waveplate. In the composite material device concept access to the cavity for the insertion of polarisation selectivity is clearly impossible. The other alternative is temperature control of the KTP. This approach would clearly involve a considerable increase in the complexity of the frequency doubled device and the intimately contacted KTP, over the changing incident pump powers, is experiencing a dynamic thermal environment and the temperature control of the KTP would have to continually altered.

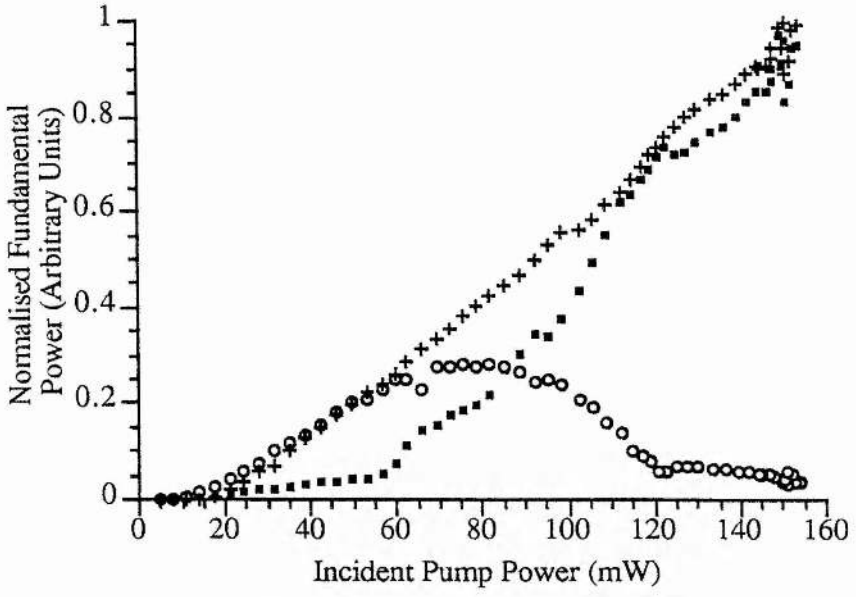

Figure 5.5.7: Normalised Fundamental Power in
(i) Circles: Polarisation State Perpendicular to Nd:YVO_4 c-axis
(ii) Small Filled Squares: Polarisation State Parallel to Nd:YVO_4 c-axis
(iii) Crosses: Total Normalised Fundamental Power

In order to examine the amount of thermally induced waveplating in the KTP the amount of fundamental power contained in polarisation directions parallel to and

perpendicular to the Nd:YVO_4 c-axis was measured as the incident pump power was increased from threshold up to the maximum value. The values are shown in figure 5.5.7 above.

Clearly the KTP experiences sufficient changes such that the waveplating action of the KTP crystal is altered markedly. Indeed the eigenpolarisation state of the circulating fundamental (that is the polarisation state of the intracavity radiation which is allowed to be built up without being continually perturbed) is changing across the values of pump power used. The fundamental polarisation state is clearly elliptical but of varying degrees ranging from near circularity at 85 mW of incident pump to a degree of ellipticity virtually indistinguishable from c-axis linearly polarised light. This polarisation state within the KTP may clearly drive down the amount of conversion from fundamental to second harmonic the theory of which assumes a constant fundamental input polarisation. From the results shown in figure 5.5.6 it is also clear that the amount of conversion obtained is only slightly less than that expected from the known values of 1 μm flux and confined mode size. What is perhaps more of an issue is the relation between the anisotropic gain of the Nd:YVO_4 material [1-4] and the elliptical eigenpolarisation of the microresonator. However, as the relation between incident power and fundamental output power is nearly linear over the pump powers used it is evident that the behaviour of the 1.064 μm operation of the device is no different from that if the eigenpolarisation of the cavity remained constant. Indeed from figure 5.5.6 it is evident that the optical gain as seen by the circulating 1.064 μm is insensitive to the changing eigenpolarisation state and to all intents and purposes is very similar to the eigenpolarisation state being linear along the Nd:YVO_4 c-axis [1-4] at all pump powers.

Spectral Purity and Signal to Noise Ratio of Output of Device

Chapter 4 discussed the theory behind the spectral selectivity of a microchip laser cavity as a function of the spectroscopic characteristics of the gain material around the wavelength of interest, the intra-cavity mode spacing and the gain length within the

material. The modelling and results presented indicated that microchip lasers have the highly desirable property of oscillating on a single axial mode under the appropriate conditions. The spectral purity of the output of the composite material microchip laser was monitored continuously using a scanning plane/parallel Fabry-Perot etalon and a one metre "Monospek" monochromator. It was found that even just above threshold the device was oscillating on two axial modes in the infra-red. The ratio of the intensities in the infra-red was approximately seven to one from stronger to weaker mode. The spacing between the two axial modes and their relative intensities may be seen below in the transmission of the 176 GHz free spectral range Fabry-Perot.

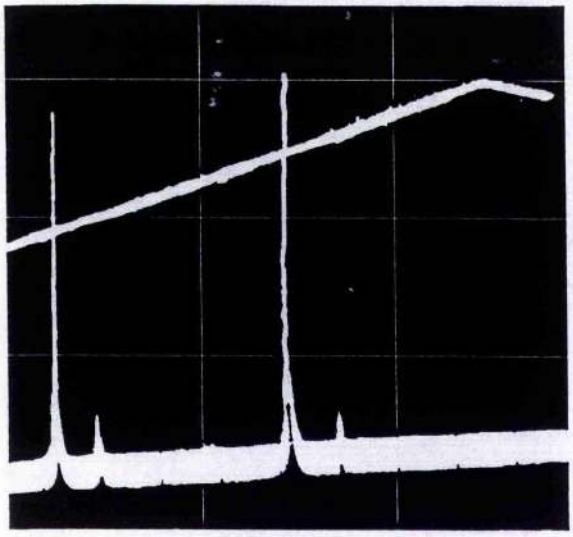

Figure 5.5.8: Output Spectrum of Composite Material Device for 150 mW Pump Power as Obtained from Transmission of Scanning Fabry-Perot. The Straight Line at the Top is the Drive Voltage for Piezo-ceramic Two Free Spectral Ranges of the Transmission of the Fabry-Perot are Shown

The frequency separation of the two infra-red axial modes was measured from the above trace to be 30 GHz Examination of the infra-red output using the monochromator verified that the additional, weaker spectral component was driven by the principal gain bandwidth, located at 1.0643 μm, and not by an adjacent transition. A Glan-Thomson polariser was placed in the infra-red output of the device to examine the polarisation state of each of the two spectral components. It was found that components of each longitudinal mode were present in polarisation states parallel to and perpendicular to the Nd:YVO_4 crystal c-axis. This indicated that both axial modes originated in the high gain

polarisation direction of the Nd:YVO_4 crystal [1-4]. The axial mode spacing for the 2 mm KTP and 0.5 mm Nd:YVO_4 was calculated to be 33 GHz. The frequency spacing of the two spectral components corresponds to a position very similar to the expected position for a second axial mode associated with the lowest order spatial mode. The second spectral component is most likely to be due to weak oscillation of an adjacent axial mode.

The "green problem" [36,37] was first considered in detail by Baer who observed chaotic amplitude fluctuations in an intra-cavity doubled, diode pumped Nd:YAG laser. Baer found that the green output of the laser consisted of a series of apparently random spikes superimposed on a small C.W. background [36,37]. Clearly such amplitude fluctuations in the intensity of the green output would be a major concern in practical uses such as high density optical storage systems [38,39]. When Baer used an intra-cavity etalon to constrain the laser to operate on a single axial mode the chaotic fluctuations ceased and when the etalon was adjusted so as to permit two axial modes in the infra-red the fluctuations became periodic. Examining the green output during dual axial mode operation Baer observed the existence of three spectral components. There were two components, one for the doubled component of each of the infra-red modes and an additional component corresponding to a sum-frequency interaction between the two axial modes [36,37]. Two other features of the periodic intensity fluctuations in the green were firstly that the modulation depth of the oscillation was found to be only weakly dependent on the pump level and secondly that as the non-linear coupling coefficient was lowered, by moving the KTP crystal away from the cavity waist, the frequency of the oscillation increased.

Baer explained this behaviour in a simple phenomenological manner by considering the sum-frequency interaction between the two infra-red axial modes and the intensity dependent losses borne by each mode through this process. In the sum-frequency interaction between the two modes the power contributed to the sum-frequency output from each axial mode is the same [36,37]. Therefore both modes share equally the

losses that are due to this non-linear process. In contrast the doubling losses for each axial mode are borne by that mode alone. The intensity fluctuations and the cavity losses for each mode have been considered by Baer in the time domain as shown below.

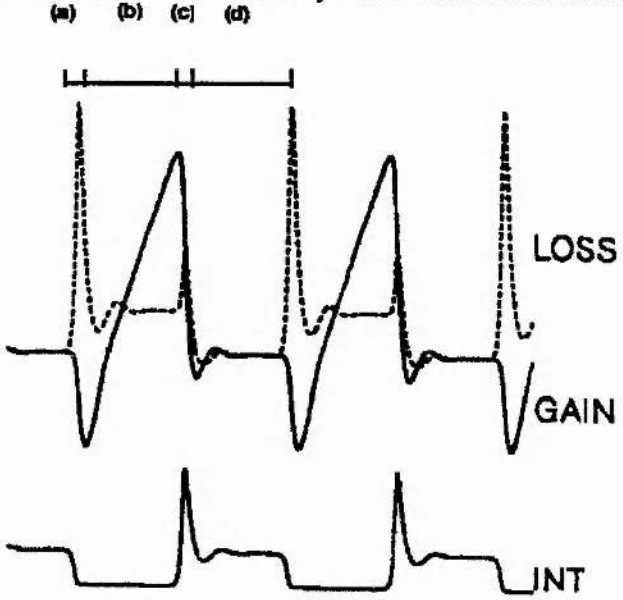

Figure 5.5.9: Gain and Loss of Mode 1 as a Function of Time for an Intra-Cavity Doubled Two Mode Laser. The Intensity of Mode 1, Which is Shown Here Switching Altenatively On and Off, is Shown as a Timing Reference.(after [36])

The temporal progression of the interaction, which is from left to right across the page, falls into the distinct regions as indicated in the figure above.

a) Mode 2 emits a pulse thus increasing the losses for mode 1 via the sum-frequency interaction such that mode 1 falls below threshold and ceases to oscillate.

b) The intensity of mode 2 reaches a quasi-steady state and the losses for mode 1 stabilise. The gain for mode 1 which has remained undepleted begins to increase with time such that mode 1 reaches threshold and begins to oscillate.

c) Mode 1 emits a pulse thus increasing the sum-generation losses for mode 2 which are sufficient to bring down mode 2 to below threshold.

d) Mode 1 reaches a quasi-steady state while the gain for mode 2 increses linearly with time such that the mode 2 reaches threshold and begins to oscillate and the cycle repeats.

Baer has used the above simple model for the amplitude fluctuations to understand perhaps the most unusual feature of the mode-coupling oscillations. This is the inverse dependence of the frequency of the periodic amplitude fluctuations with non-linear coupling coefficient. This may be accounted for when one considers that for increasing non-linear coupling the added sum-frequency losses for mode 1 in part (a) of the cycle are increasing and consequently the mode is brought further down below threshold. Therefore more time is needed for the gain for mode 1 to build up to an appropriate value such that mode 1 is above threshold [36]. It should be noted however at this point that for coupling to occur between two longitudinal modes both modes must be in the same polarisation orientation [36,37]. Oka and Kubota have shown both analytically and experimentally that for orthogonally polarised axial modes mode coupling does not occur [40]. Similarly for the purpose of the above discussion Baer has assumed that the amount of coupling of the fundamental into the second harmonic is large (approx. 20 % of the available fundamental [36]) and that the two oscillating axial modes are of similar intensity and close enough in frequency separation such that they are both within the phase-matching bandwidth for SHG and sum-frequency interactions.

In the composite material device characterised above it was observed that the intensity ratio of the two axial modes was approximately eight to one. Similarly the frequency separation of the two modes is significantly larger than that present in Baer's intra-cavity doubled device by a factor of approximately ten [36]. The full-width half-maximum spectral bandwidth of the SHG process in KTP is, for this crystal length, 1.2 nm [14]. The wavelength separation of the two observed axial components is 0.2 nm which is not insignificant in the light of this spectral bandwidth. Therefore the two axial modes may in fact see a coupling differential into both the SHG and sum-frequency processes because of their relatively larger wavelength separation as compared to other larger intra-cavity doubled systems.

In order to look for periodic amplitude fluctuations due to axial mode coupling the signal to noise ratio of the output of the composite material device was monitored using the experimental set up as shown below.

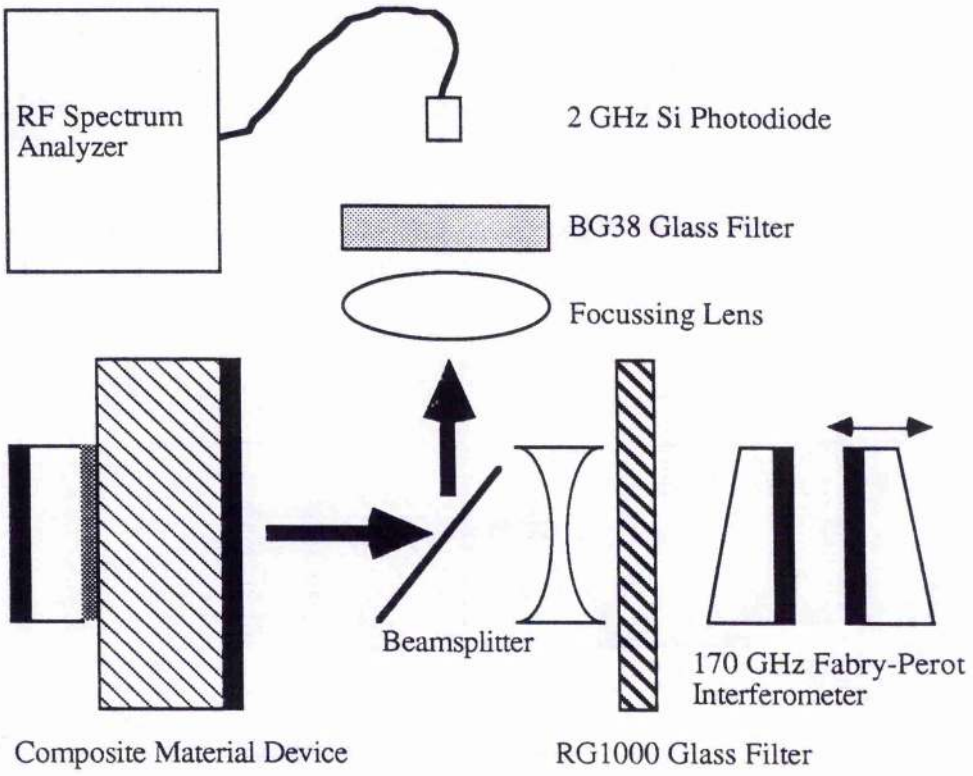

Figure 5.5.10: Experimental Apparatus for Examination of S/N Ratio of Composite Material Device

The BG 38 filter in front of the A.C. coupled, fast photodiode (2 GHz) blocked the fundamental and any residual pump from the device such that the noise spectrum of the green output could be monitored on the spectrum analyser. The RG 1000 filter blocked both the visible output from the device and any residual pump light such that the 170 GHz scanning Fabry-Perot interferometer monitored the fundamental spectrum from the device. A Glan-Thompson polariser was inserted in front of the Fabry-Perot interferometer and allowed analysis of the polarisation orientation of any observed spectral components.

As shown in figure 5.5.8 at 150 mW of pump power the infra-red output of the device was found to consist of two axial modes, separated by 30 GHz and in the same

polarisation orientation. This situation should lead to a periodic fluctuation in the intensity of the generated green output. The R.F. noise spectrum was examined from 0 to 2 GHz and is shown below. The R.F. noise spectrum shown below is averaged over 100 samples.

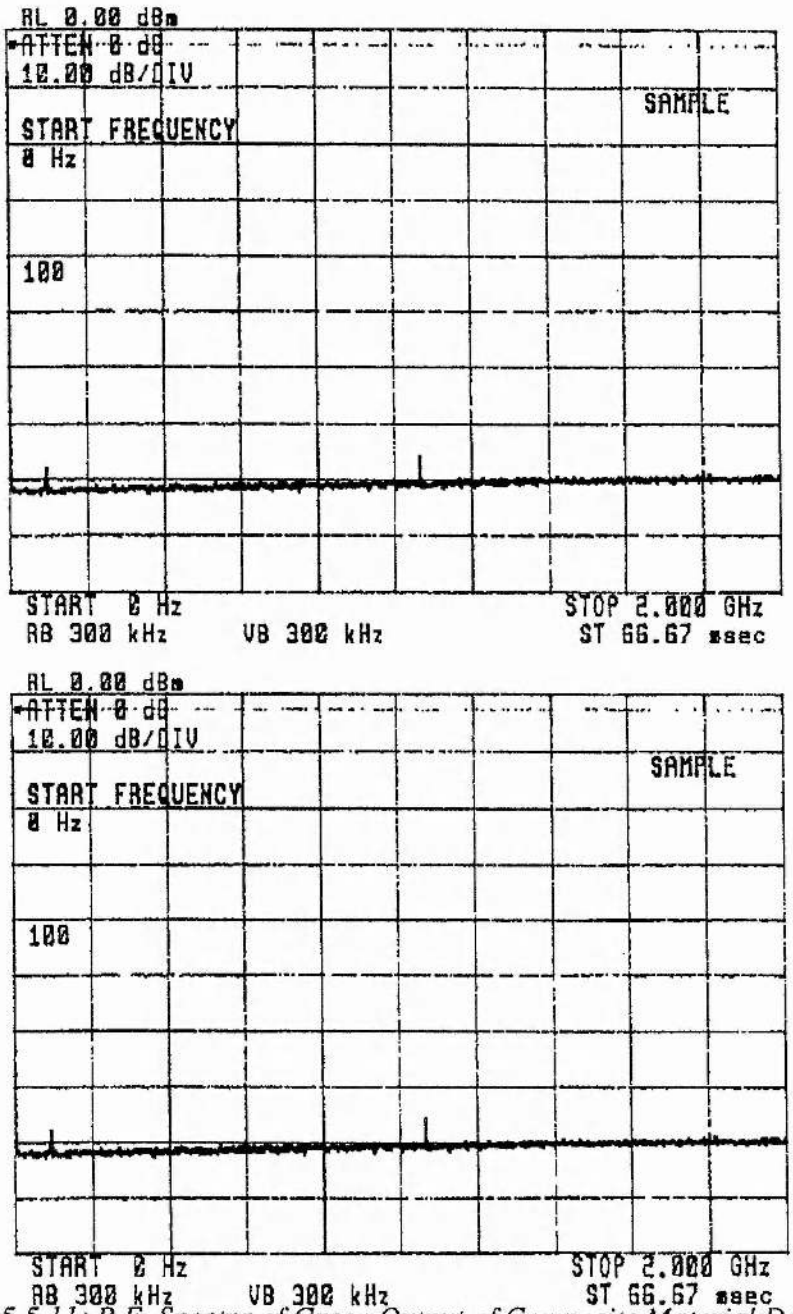

Figure 5.5.11: R.F. Spectra of Green Output of Composite Material Device for 150 mW of Incident Pump Power Top: Green Output Unblocked Bottom: Green Output Blocked

The small features at 95 MHz and at 1.05 GHz which appear in both R.F. spectra are undoubtedly experimental artefacts. When the output beam from the device was blocked and the R.F. spectra examined over the same range the two small features were still evident. Clearly the signal-to-noise ratio of the green output is excellent over the 0 to 2 GHz range examined. The inter-transverse mode frequency for the cavity configuration under consideration is given by [35].

$$\Delta\upsilon = \frac{c}{2\pi z_0}\Delta(m+n) \qquad \text{Eqn. 5.5}$$

where

$$z_0 = \frac{\pi\omega_0^2 n_0}{\lambda} \qquad \text{Eqn. 5.6}$$

ω_0 is the $1/e^2$ half-width waist of the mode, n_0 is the refractive index of the material within the cavity, c is the speed of light, λ is the wavelength of the circulating radiation and m and n are the transverse mode indices. From figure 5.5.5 it may be seen that for 150 mW of incident pump power the fundamental mode waist is 60 μm. Substituting this value into equation 5.5. and 5.6 the resultant inter-transverse mode spacing is 1.4 GHz. From figure 5.5.11 no inter-transverse beat frequency may be seen. Clearly this indicates that the composite material device is not operating on an adjacent transverse mode and this confirms further the measurements of the M^2 value performed on the output of the device.

For applications such as high density optical storage, noise in the green output in the frequency range below 10 MHz is more of an issue as this frequency of perturbation is more likely to degrade the quality of the information recovered from the optical disc information layer [38,39]. As may be seen from figure 5.5.11 the video bandwidth of the spectrum analyser was 300 kHz for the R.F. scan of 2 GHz therefore it was desirable to look more closely at different frequency ranges.

For 150 mW of incident pump power (6 mW of C.W. green power) it was verified that the infra-red output of the device was of the same form as shown in figure 5.5.8. The R.F. noise spectrum of the green output was recorded up to 1 MHz and 10 MHz. As

may be seen from the R.F. spectra in figure 5.5.12 no periodic amplitude perturbations are observable in the green output of the device and by examination of the control R.F. spectrum and the 1 MHz scan there is an overall slight decrease in the signal-to-noise ratio of approximately 10 dB over the 1 MHz scan.

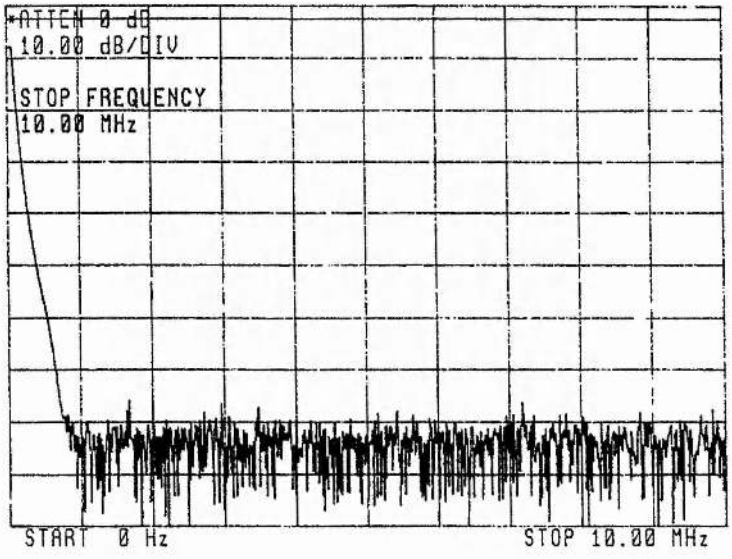

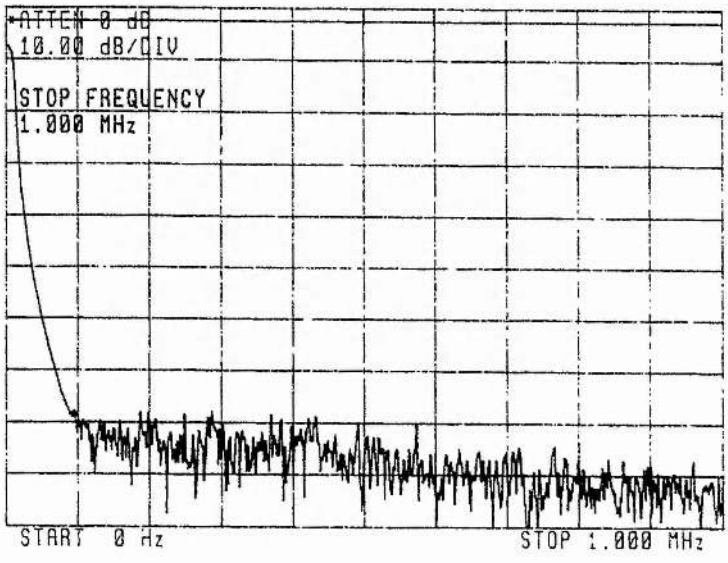

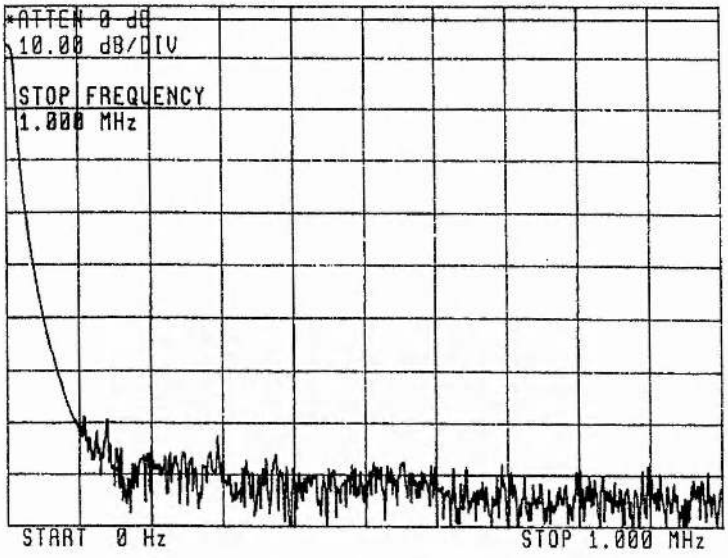

Figure 5.5.12: R.F. Noise Spectra of Green Output for 150 mW of Incident Pump for (Top) 0 to 10 MHz (Resolution Bandwidth = 100 kHz) (Middle) 0 to 1 MHz(Resolution Bandwidth = 10 kHz) (Bottom, Control) 0 to 1 MHz with Beam Blocked (Resolution Bandwidth = 10 kHz)

To verify that the detection system used in this experiment could actually resolve amplitude fluctuations in the green output of the device the following experiment was performed. As may be seen in figure 5.5.13 below a small sinusoidal modulation was applied to the SDL laser driver such that the pump power was modulated.

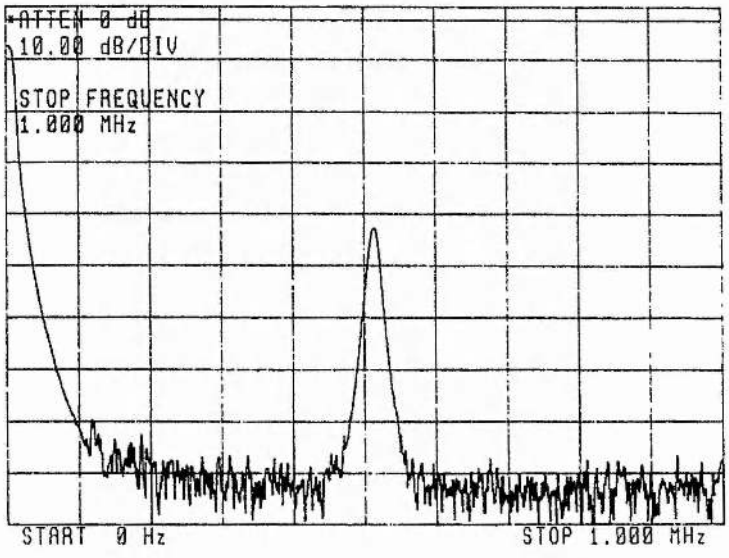

Figure 5.5.13: R.F. Spectrum of Sinusoidally Modulated (2.5% p.-p. at 520 kHz) Green Output

The depth of the perturbation to the pump was chosen such that when the green output of the device was examined, using a d.c. coupled reverse biassed BPX-65 photodiode, the sinusoidal perturbation was 2.5 %, peak-to-peak, of the total signal. The frequency of the modulation was set to be 520 kHz. The applied modulation to the pump was then doubled such that, peak-to-peak, it was measured to be 5 % of the total green output. Unfortunately in order to achieve this modulation depth the frequency of the modulation had to be lowered to 340 kHz because of limitations in the frequency response of the SDL laser diode driver. The R.F. spectrum of the larger modulation to the pump may be seen below.

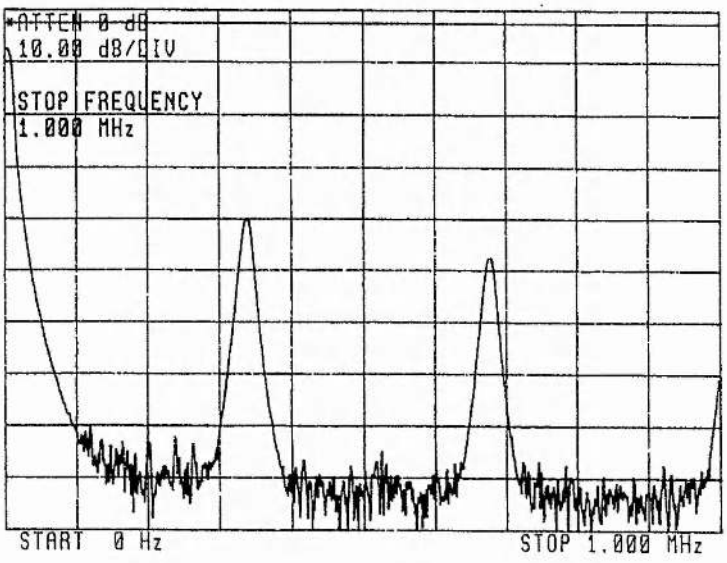

Figure 5.5.14: R.F. Spectrum of Sinusoidally Modulated (5% p.-p. at 340 kHz) Green Output

The second harmonic of the true signal may be seen at approximately 700 kHz. The peak corresponding to the 5% amplitude modulation was found to be 3 dB above the noise floor from that corresponding to the 2.5% modulation depth. Therefore the resolution of the apparatus is sufficient so as to discern amplitude fluctuations 50 dB below 2.5 % of the d.c. green signal. The applied peak to peak modulation is one fortieth (16 dB) of the C.W. signal level. Therefore the apparatus used is capable of resolving amplitude fluctuations 66 dB below the C.W. signal level.

Baer's modelling of the "green problem" [36] as outlined above predicted that in the regime where the non-linear coupling coefficient in a laser cavity was low then the amplitude fluctuations in the green would increase until they reached the relaxation oscillation of the laser. Using the conventional rate equation methodology the frequency of the relaxation oscillations possible in the composite material device, for excitation ten times above threshold, were calculated to be 140 kHz. It was assumed for the purposes of this calculation that the presence of the non-linear frequency conversion did not damp the relaxation oscillation frequency. The R.F. spectrum of the green output of the device, under the axial mode conditions present in figure 5.5.8, for the region corresponding to the laser relaxation oscillation frequency may be seen below.

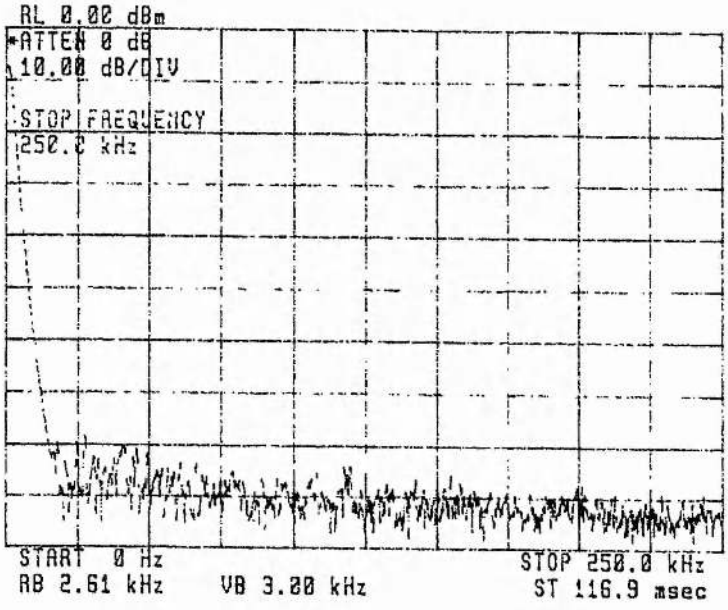

Figure 5.5.15: R.F. Spectrum of Green Output of Composite Material Device in the Region Corresponding to Relaxation Oscillation Frequency of the Device

Clearly the output of the device does not exhibit amplitude fluctuations characteristic of relaxation oscillations associated with the excitation rate and the laser cavity under consideration.

The reason for the stable operation of the composite material device even in a dual axial mode condition may be attributable to the relatively low non-linear coupling coefficient present in the composite material device. Additionally, the dominance of one axial

mode over the other may reduce the loss fluctuations as seen by the dominant mode due to the sum-frequency interaction [36]. As has been stated in the outline of Baer's model of the green problem the spectral bandwidths of both the doubling and sum-frequency non-linear interactions are finite and affect the magnitude of the non-linear coupling of the axial modes.

Section 5.6: A Close Coupled Nd:YVO_4/KTP Composite Material Microchip Laser.

The composite material device described above clearly operated reasonably efficiently and stably but had the disadvantage of having to be excited, via coupling optics, by a laser diode within an industry-standard TO-3 can. This limited, by a combination of aperturing and deterioration of the laser diode, the amount of pump radiation available for excitation of the device to 150 mW. In addition to the restriction of the amount of incident power available measurements of the pump spot size indicated that the pump field, as produced by the coupling optics, was significantly less than that possible close to the open facet of a half-Watt laser diode array [28,42]. This clearly impeded any effort to scale up the green output powers available from such a device to a point where these devices may effectively compete with green HeNe lasers or air cooled-argon-ion lasers for example. A close-coupled composite material device would also represent a quantum leap in miniaturisation and technologically be highly desirable.

The pump source for this experiment was exactly the same laser diode as used in the lens coupled experiments (Spectra Diode Laboratories SDL-2432) described above but was an open facet device. The dimensions of the active area were 100 μm in the plane parallel to the diode junction and 1 μm in the plane perpendicular to the diode junction [42]. The constituent parts of the close-coupled device were exactly the same two pieces used in the lens-coupling experiments described above. The Nd:YVO_4 gain material was oriented correctly for maximum pump absorption and appropriately positioned over the active area of the semiconductor laser chip with most of the aperture of the Nd:YVO_4 gain material over the diode sub-mount. The bottom edge of the Nd:YVO_4

gain material was secured using cyanoacrylate adhesive. The Nd:YVO_4 gain material as mounted on the laser diode submount is shown in the photograph below.

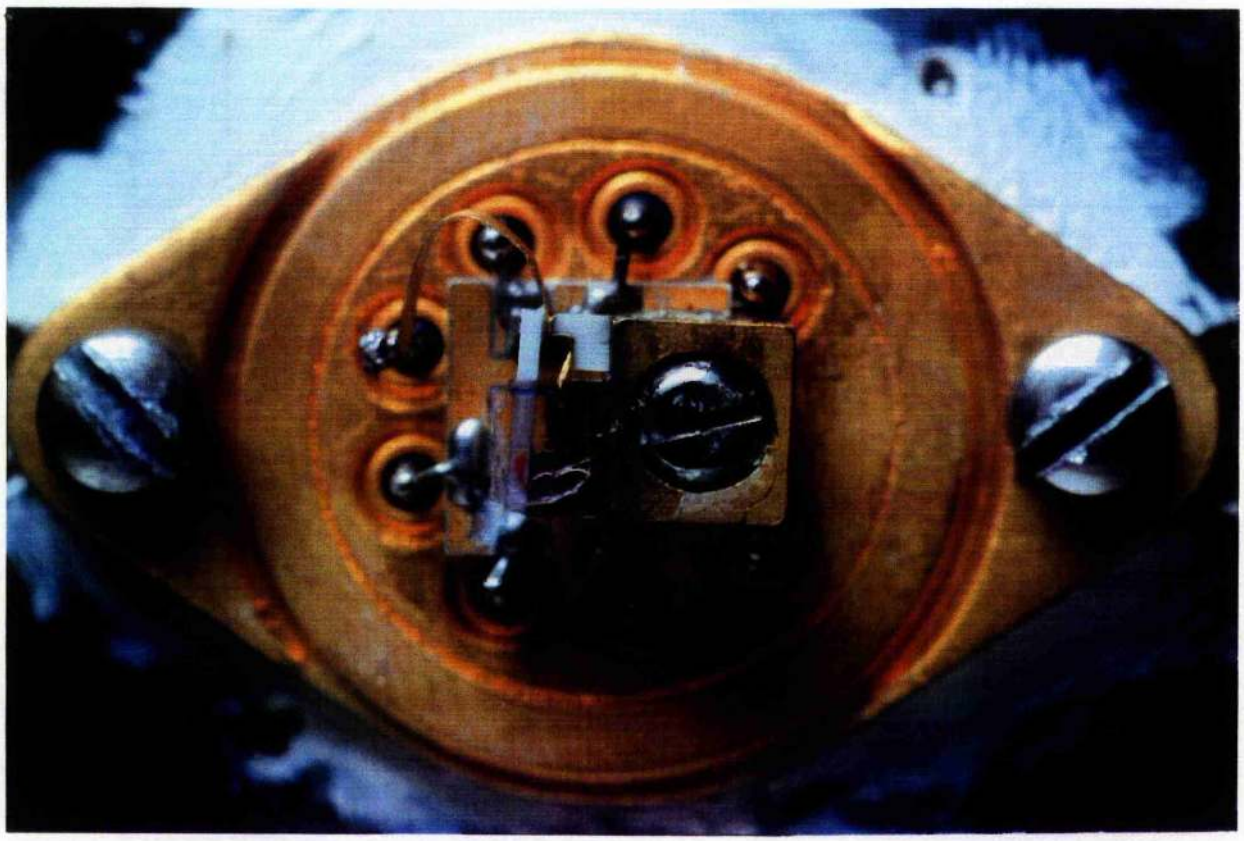

Figure 5.6.1: Nd:YVO_4 Gain Material Closely Coupled to Laser Diode (The Gain Material is the Pinkish Slab in the Middle of the Picture)

In mounting the Nd:YVO_4 gain material every effort was made to ensure that the input surface of the Nd:YVO_4 was in direct contact with the diode submount. What was unknown was the recess distance from the diode chip facet and the surface of the diode sub-mount. Clearly because of the divergence properties of the laser diode output beam, it was desirable, in order to access the highest possible density of pump field, to have the Nd:YVO_4 gain material as close as possible to the laser diode facet.

A small drop of index matching fluid as used above was placed on the Nd:YVO_4 gain material and the two pieces brought together in a Fizeau interferometer to the same high degree of optical parallelism as was achieved in the lens coupled device such that the optical parallelism between the HR surfaces of the composite device was limited only by the initial parallelism of each component. The photograph below shows the two constituent parts of the device before being brought together.

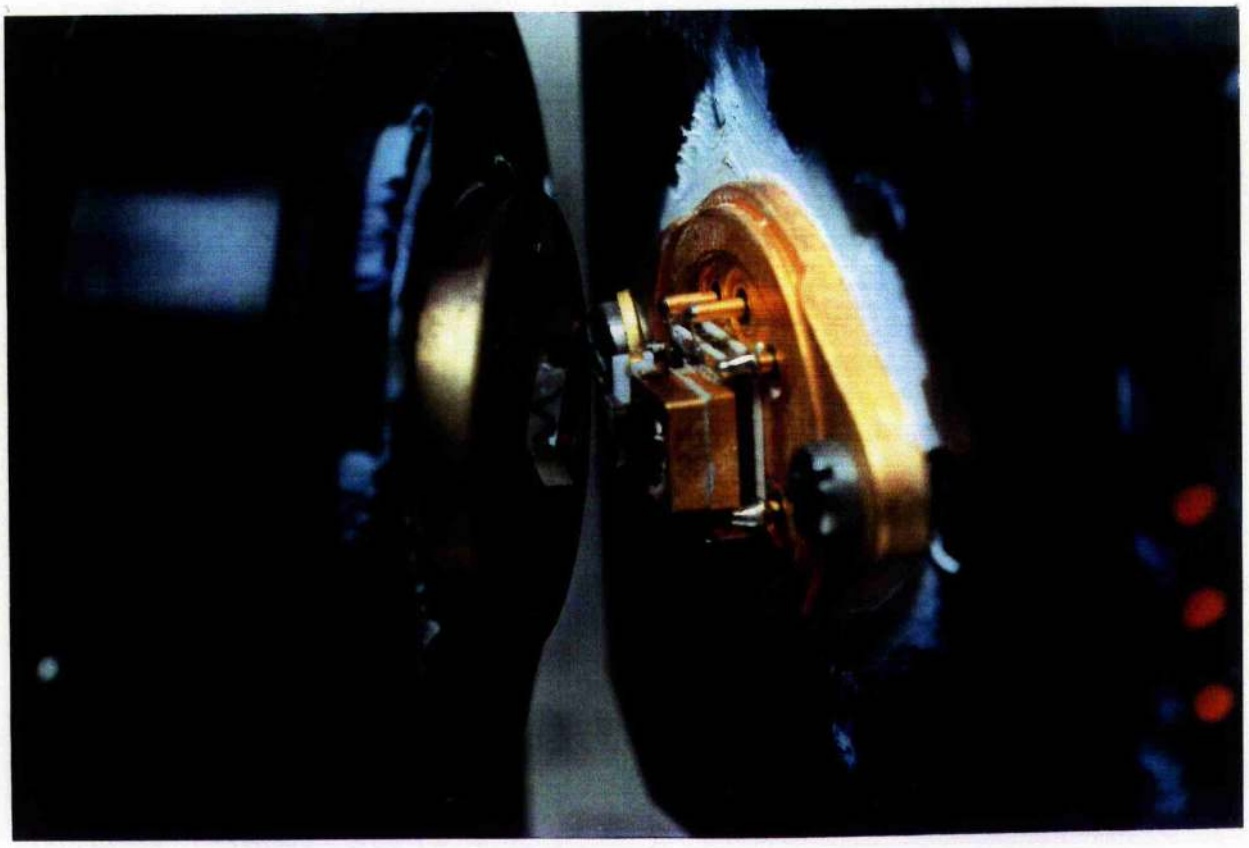

Figure 5.6.2: Constituent Parts of Composite Material Microchip Laser Before Assembly
The KTP Material is on the Left of the Above Figure. The Gain Material is on the Right of the Picture on the Laser Diode Sub-Mount

The power performance of the composite material device may be seen in figure 5.6.3 below.

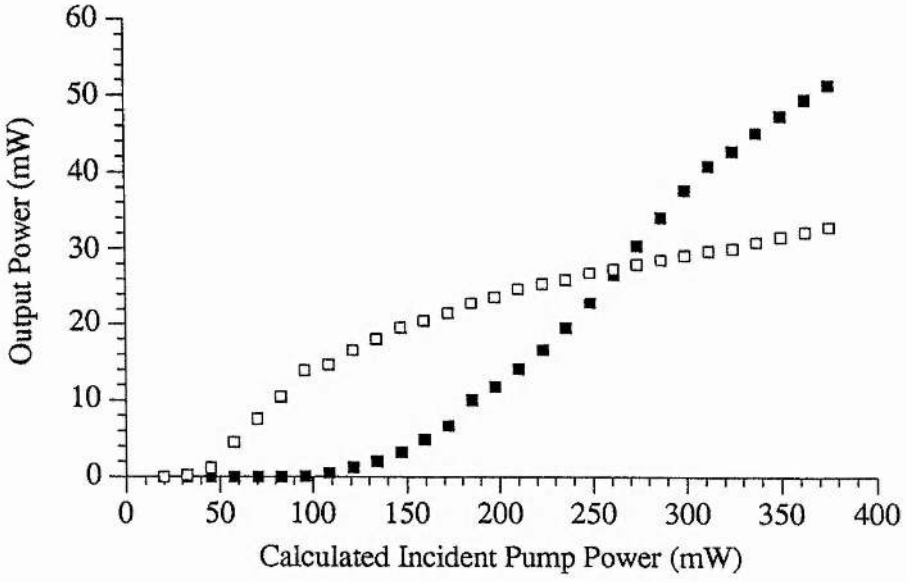

Figure 5.6.3: Green Output Power (Filled Squares) and Total Fundamental Power (Open Squares) as a Function of Incident Pump Power for Closely-coupled Composite Material Device

The maximum conversion efficiency from 809 nm pump to the green was 12 %. The higher efficiency of the composite material device is undoubtedly due firstly to the fact that the incident pump powers used in this experiment are significantly higher than in the lens coupled device. Secondly, the pump field density at the input surface of the closely coupled device may be higher than that produced by the coupling optics configuration used above. No fluctuations in the output power of the composite material device attributable to diode wavelength changes were observed. The output at 50 mW of green output power may be seen in the photograph below.

The secondary spot visible in figure 5.6.4 on the card to the bottom left of the central lobe is due to a reflection off the facet of the semiconductor chip and is an interesting indicator of the angular tolerance on the alignment between the input surface of the device and the facet of the laser diode chip. The slight angular misalignment between the device and the pump source may additionally have the effect of increasing the optical isolation between the microchip laser and its diode pump. The spatial quality of

the output beam was found to be as good as that obtained with the lens coupled device provided that the gain material was kept flush with the laser diode sub-mount during assembly. Both long term stability and short term stability were found to be comparable with those of the lens coupled device.

Figure 5.6.4: 50 mW of Green Output Power from Closely-Coupled Composite Material Device

Section 5.7: 130 mW Green Output Power from a Laser Diode Array Pumped Nd:YVO_4/KTP Composite Material Microchip Laser.

The gain and non-linear materials constituting the green microchip laser discussed above were assembled to the same exacting optical parallelism standards as discussed

before and placed in front of a coupling optics train identical to that used in section 5.5. The only difference between the experimental configuration described here and that described in section 5.5 was the laser diode pump source. Instead of the previous 0.5 W SDL device emitting from a 100 μm x 1 μm aperture a 2 W SDL device emitting from a 200 μm x 1 μm aperture was utilised. Because of aperturing at the focusing lens the coupling optics used would still produce a comparable spot size to that of the half-Watt device but the 2 W diode would be capable of delivery of more incident power because of its higher brightness [42]. The rationale behind this particular experiment was to investigate the possibility of scaling green output powers by using laser diode pump sources of increasing brightness.

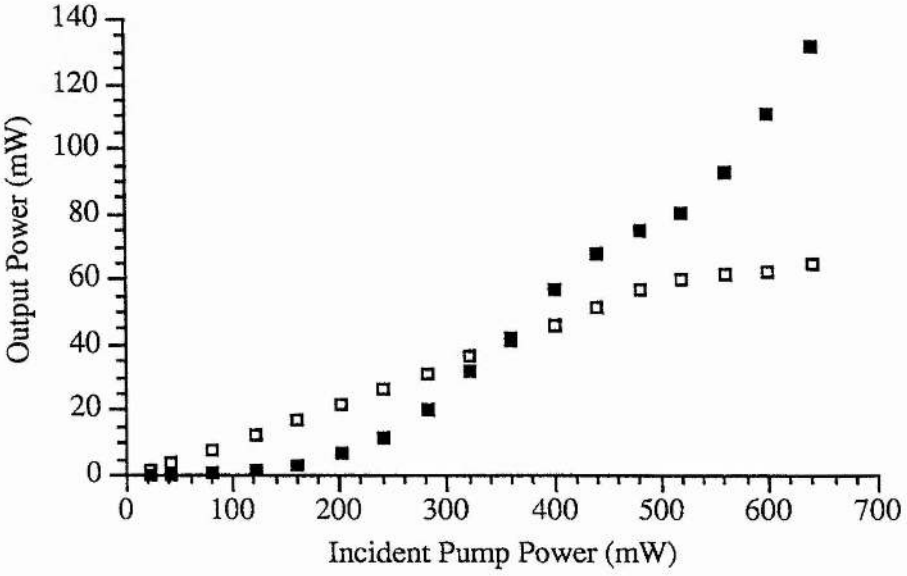

Figure 5.7.1: Power Performance of High Brightness Pump Source Excited Composite Material Microchip Laser (Open Squares: Fundamental Power) (Filled Squares: Green Power)

As may be seen from the power curve shown above approximately 130 mW of incident pump power was obtained for 650 mW of incident pump power. This represents a conversion efficiency of 20 % for pump power to green power. More interestingly was the fact that even at these high incident pump powers the fundamental output of the device remained Gaussian in cross-section as may be seen in the figure below.

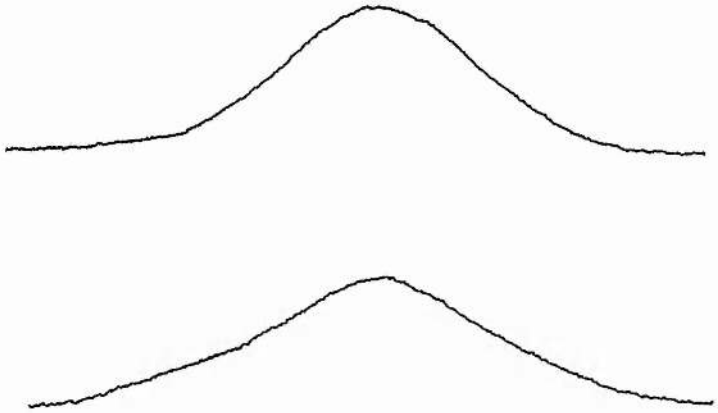

Figure 5.7.2: Far-field Intensity Cross-section of Output Beam at (Top) 250 mW of Incident Pump Power and (Bottom) 650 mW of Incident Pump Power

As was seen in the low-powered lens coupled device and the closely-coupled device the green output power exhibited highly stable operation. Clearly these preliminary experiments point to the advantages of high brightness laser diodes as excitation sources for composite material microchip lasers. These preliminary results indicate that this type of device may eventually rival air cooled Argon ion lasers as C.W. green sources.

Section 5.8: Conclusions and Summary

A composite material Nd:YVO_4/KTP microchip laser was successfully fabricated and characterised. The composite material device consisted of a 0.5 mm thick Nd:YVO_4 gain section in intimate optical contact with a 2 mm thick KTP non-linear section. The device was longitudinally pumped by

i) A 100 μm x 1 μm laser diode array via coupling optics up to 150 mW of incident pump power.

ii) A 100 μm x 1 μm laser diode array directly from the open facet of the array

iii) A 2 W 200 μm x 1 μm laser diode array via coupling optics up to 650 mW of incident pump radiation.

The most rigorous characterisation of the device was performed using the low pump power lens coupling excitation scheme. The device in this excitation scheme produced 6 mW of stable green radiation for 150 mW of pump radiation. The device operated in a near diffraction limited spatial mode at all pump powers. The composite material microchip laser cavity was found to exhibit a pump power dependent output beam divergence indicating a dynamic, pump power dependent cavity configuration. The KTP non-linear element was found to act as a temperature sensitive waveplate creating a variable, elliptical eigenpolarisation state within the cavity. This eigenpolarisation state was found to degrade, though only very slightly, the amount of conversion of the fundamental into the second harmonic. The spectral output of the device was found to consist of two infra-red axial modes separated by the free-spectral range of the cavity and in an intensity ratio of approximately eight to one. Despite both modes being in a polarisation orientation suitable for a sum-frequency interaction no periodic amplitude fluctuations in the green output could be observed despite using an R.F. spectrum analyser sensitive to amplitude fluctuations 66 dB below the C.W. green output signal. The lack of observable amplitude fluctuations in the green output was attributed to the relatively low non-linear coupling present in the laser system, the intensity dominance of one mode over the other and the relative large wavelength separation of the axial modes.

When pumped directly from the facet of a half-Watt 100 μm x 1 μm array the same composite material microchip laser produced 50 mW of C.W., fundamental spatial mode stable green output power. Such a composite material device could easily fit within an industry standard TO-3 can to provide a cost-effective, ultra-compact source of coherent green radiation. The potential for power scalability was demonstrated when the device was pumped successfully using a 2 W 200 μm x 1 μm array via coupling optics. Over 130 mW of C.W. green radiation of high spatial quality green radiation was obtained in these preliminary experiments which pointed to further improvements being readily achievable by the use of high brightness laser diode pump sources.

References

[1] J. R. O'Conner, Appl. Phys., **9**, p. 407, (1966)

[2] P. P. Yaney and L. G. DeShazer, J. Opt. Soc. Am., **66**, no. 12, p. 1405, (1976)

[3] L. G. DeShazer, A. W. Tucker, M. Birnbaum and C. L. Fincher, 1975 I.E.E.E./O.S.A. Conference on Laser Engineering and Applications Technical Digest Post Deadline Paper no. 4.10

[4] I.T.I. Electrooptics Corp., Los Angeles, Ca., U.S.A., Data Sheet on Nd:YVO_4

[5] S. A. Payne, B. H. T. Chai, W. L. Kway, L. D. Deloach, L. K. Smith, G. Lutts, R. Peale, X. X. Zhang, G. D. Wilke and W. F. Krupke, Paper CPD12-1/24, Conference on Lasers and Electro-optics, (CLEO), 1993, Technical Digest Series, Vol. 11, Optical Society of America, Washington D. C., U. S. A., p.24

[6] H. G. Danielmeyer and M. Blaette, Appl., Phys., **1**, p. 269-273, (1973)

[7] N. MacKinnon and B. D. Sinclair, Opt. Comm., **94**, p. 281-288, (1992)

[8] J. J. Zayhowski, in Optical Society of America Proceedings on Advanced Solid-State Lasers, H. P. Jenssen and G. Dube, eds., Vol. 13, (Optical Society of America, Washington D. C., U.S.A.)

[9] P. A. Leilabady, D. W. Anthon and P. O. Gullicksen, Paper CM16, Conference on Laser and Electro-optics, (CLEO), 1992, Technical Series Digest, Vol. 11, Optical Society of America, Washington D. C., U. S. A., p. 58

[10] D. W. Anthon, A. T. Eggleston, G. R. Ristau, Paper CM14, Conference on Laser and Electro-optics, (CLEO), 1992, Technical Series Digest, Vol. 11, Optical Society of America, Washington D. C., U. S. A., p. 60

[11] K. F. Hulme, Rep. Prog. Phys., **36**, p. 497, (1973)

[12] R. F. Belt, G. Gashurov and Y. S. Liu, Laser Focus, October 1985, p. 110

[13] W. Koechner, "Solid-State Laser Engineering", Springer-Verlag, Second Edition, p.477

[14] H. Ito, H. Naito and H. Inaba, J. Appl. Phys., **46**, no. 9, p. 3992, (1975)

[15] M. V. Hobden, J. Appl. Phys., **38**, no. 11, p. 4365, (1967)

[16] J. Q. Yao and T. S. Fahlen, J. Appl. Phys., **55**, no. 1, p. 65, (1983)

[17] D. N. Nikogosyan and G. G. Gurzadyan, Sov. J. Quant. Electron., **17**, no.8, p. 970 (1987)

[18] J. T. Lin, Lasers and Optronics, July 1989, p. 61

[19] R. C. Eckardt, H. Masuda, Y. X. Fan and R. L. Byer, I.E.E.E. J. Quant. Electron., **QE-26**, no. 5, p. 922, (1990)

[20] T. Y. Fan, C. E. Huang, B. Q. Hu, R. C. Eckardt, Y. X. Fan, R. L. Byer and R. S. Fiegelson, Appl. Phys., **26**, no. 12, p. 2390, (1987)

[21] J. Hong, B. D. Sinclair, W. Sibbet and M. H. Dunn, Appl. Opt., **31**, no. 9, p. 1318, (1992)

[22] R. W. Wallace and S. E. Harris, Appl. Phys. Lett., **15**, no. 4, p. 111, (1969)

[23] T. Y. Fan and R. L. Byer, Opt. Lett., **12**, p. 809, (1987)

[24] J. Hong, Ph. D. Thesis, University of St. Andrews, Ch. 6, p. 135

[25] A. Yariv, "Quantum Electronics", Third Ed., Wiley, (1989), p. 402

[26] N. MacKinnon and B. D. Sinclair, Opt. Comm., **95**, no. 1, (1994)

[27] T. Sasaki, T. Kojima, A Yokotani, O. Oguri and S. Nakai, Opt. Lett., **16**, p. 1665, (1991)

[28] N. MacKinnon, Ph. D. Thesis, University of St. Andrews, Ch. 4., p. 85

[29] W. H. Steel, "Interferometry", Cambridge University Press, 1967, p. 10

[30] N. MacKinnon, C. J. Norrie and B. D. Sinclair, J. Opt., Soc., Am., B, 11, no. 3, p. 1, (1994)

[31] A. Yariv, "Quantum Electronics", Third Ed., Wiley, (1989), p. 378

[32] H. Nagai, M. Kume, I. Ohta, H. Shimizu and M. Kazumura, I.E.E.E. J. Quant. Electron., **QE-28**, no. 4, p. 1164, (1992)

[33] T. Y. Fan, I.E.E.E. J. Quant. Electron., **QE-27**, no. 9, p. 2091, (1991)

[34] T. Sasaki, T. Kojima, A. Yokotani, O. Oguri and S. Nakai, Opt. Lett., **16**, no. 21, p. 1685, (1991)

[35] A. Yariv, "Quantum Electronics", Third Ed., Wiley, (1989), p. 118

[36] T. Baer, J. Opt. Soc. Am. B, **3**, p. 1175, (1986)

[37] G. E. James, E. M. Harrel, C. Bracikowski, K. Wiesenfeld and R. Roy, Opt. Lett., **15**, no. 20, p. 1141, (1990)

[38] H. Nagai, M. Kume, A. Yoshikawa and K. Itoh, Appl. Opt., **32**, no. 33, p. 6610, (1993)

[39] A. Arimoto, M. Ojima, N. Chinone, A. Oishi, T. Gotoh and N. Ohnuki, Appl. Opt., **25**, no. 9, p. 1398, (1986)

[40] M. Oka and S. Kubota, Opt. Lett., **13**, no. 10, p. 805, (1988)

[41] R. Dunsmuir, J. of Electron. Control, **10**, p. 453, (1963)

[42] A. Siegman, "Lasers", University Science Books, (1986), p. 963

[43] Spectra Diode Laboratories, San Jose, Ca. U.S.A., Laser Diode Operators Manual, 1993

Chapter 6: Conclusions and Options for Further Work

Section 6.1: Conclusions and Summary of Work Carried Out

This thesis has outlined the basic operating characteristics of LNP microchip lasers and demonstrated derivatives of the microchip laser which extend this concept into the realm of non-linear optics and miniature solid-state visible sources.

In chapter 2 we described how a laser diode array pumped, electro-optically tunable microchip laser was successfully demonstrated. The material utilised was Nd:MgO:$LiNbO_3$ which combined both the optical gain for the microchip laser and the electro-optic effect necessary for frequency modulation. At the maximum output power of 13 mW the device operated in a near diffraction limited spatial mode (M^2 = 1.1) on six axial modes. The multi-axial mode operation was attributed to the fact that the lasing bandwidth of the principal 1.084 μm transition is relatively large with a full-width, half-maximum of 430 GHz at 13 mW of output power as opposed to a transition width of 200 GHz for the 1 μm line in Nd:YAG. Clearly the multi-longitudinal operation would limit the utility of this prototype device for many applications. However the multi-axial mode operation could be suppressed by choosing a cavity length one sixth of that used in the experiments here. A heterodyne experiment was performed between two laser diode array pumped Nd:MgO:$LiNbO_3$ microchip lasers. The axial modes of the electro-optically tuned microchip laser were found to tune at a rate of 8.9 MHz V^{-1} mm. This tuning sensitivity was found to be very similar to that expected from an analysis of the linear electro-optic effect in Nd:MgO:$LiNbO_3$.

Chapter 3 described how, using a Fizeau interferometer, the pump power induced cavity stability mechanisms present in Ti:sapphire laser pumped LNP microchip lasers were determined. It was found that the primary contribution to cavity stability came from pump induced curvature of the input surface modifying the cavity geometry from being nominally plano/plano to approximately half-symmetric. The

refractive index change within the material itself was found not to contribute to the pump induced cavity stability of the microresonator. This is in contrast to the regime present in Nd:YAG microchip lasers where pump induced stability is defined by a weak confining positive duct distributed throughout the length of the microresonator. The LNP microchip laser operated in a near diffraction limited (M^2 = 1.05) spatial mode of operation up to a maximum single frequency 1.047 μm power of 20 mW. Above this output power multi-axial mode operation was characterised by excitation of a cavity mode under an adjacent gain bandwidth located at 1.055 μm as opposed to a cavity mode adjacent to the principal axial mode.

The spectral behaviour of the LNP device, pumped this time by a laser diode array, was the subject matter for chapter 4. A model , based on spatial dephasing of adjacent longitudinal modes within an exponentially decaying gain length, was applied to the diode pumped LNP device. The model was then utilised to predict the behaviour of a microchip laser fabricated from Nd:YVO_4 as a function of gain and cavity length. What was found to be important to the single frequency performance of the device was the extent to which the available gain was localised to the input surface where adjacent longitudinal modes are significantly spatially overlapped. The single frequency behaviour of the device was then characterised as a function of absorption coefficient within the gain material. Some of the discrepancies evident between the modelled behaviour and the observed behaviour were accounted for by taking into account a thermally induced reabsorption loss differential between the two modes. The observed singie frequency results obtained with the diode pumped LNP device were also found to have a different form from that expected from the spatial dephasing model. A marked improvement, over what would be expected from the model, in the single frequency performance of the device was observed at very short gain lengths. This was attributed to a pump density dependent energy migration process of type similar to Auger recombination. Using the laser diode pump source 14 mW of single frequency, fundamental spatial mode light was observed.

Chapter 5 contained a large portion of work on a diode pumped composite material microchip laser for production of green radiation via frequency doubling in KTP, of 1.064 μm fundamental radiation from Nd:YVO_4. The composite device, when pumped by a laser diode array via coupling optics gave up to 150 mW of incident power, operated with excellent beam quality (M^2 = 1.1) at all incident pump powers. A thorough characterisation of the device was performed at pump powers up to 150 mW. At this pump level 6 mW of C.W. green radiation was obtained. The oscillating waist within the device was found to be dependent on the inverse fourth root of the incident pump power. The non-linear conversion of the fundamental into the green as a function of incident power was calculated from the known values of fundamental flux, oscillating waist and effective non-linear coefficient. It was found that the amount of green obtained was only slightly less than that expected from observed quantities. A possible cause of this discrepancy was found to be the variable eigenpolarisation state in the cavity set up by the presence of the birefringent KTP crystal. Components of the fundamental both parallel to and perpendicular to the Nd:YVO_4 crystal c-axis were examined. It was found that the eigenpolarisation of the cavity went through varying degrees of ellipticity. Using a scanning plane/parallel Fabry-Perot interferometer it was found that the device operated on two axial modes in the infra-red. The intensity ratio of the stronger to the weaker mode was approximately seven to one. The intensity stability of green output was examined using an R.F. spectrum analyser which was capable of resolving amplitude fluctuations in the green output 66 dB below the C.W. green signal. Despite operating on two axial modes in the infra-red no evidence of periodic amplitude fluctuations in the device output could be detected. This was attributed to the relatively weak non-linear coupling between the two longitudinal modes. The prospects for increased miniaturisation of these devices and increased output powers was demonstrated when 50 mW of C.W. green power was obtained when a composite device was close coupled on to the facet of a half-Watt laser diode array. The output beam of the higher power device exhibited the same spatial quality as the lower power lens coupled

device. Further improvements in the output power of the composite material device were obtained using a pump source of higher brightness when up to 130 mW of C.W. green radiation was obtained in a near diffraction limited beam.

This thesis has pointed the way ahead for microchip laser research and applications. It is evident that this new breed of miniature solid-state laser, in its various incarnations, will significantly broaden the range of opportunities for use of solid-state lasers in many applications. We regard especially the development of the green microchip laser as a significant step forward in the commercialisation of diode pumped visible lasers. In terms of developmental work there remains much still to be done on this green device but given an appropriate amount of effort there is no reason why some of the outstanding technical difficulties may not be solved.

Section 6.2: Options for Further Research

The opportunities for research into microchip lasers fall into two categories. Firstly there is the opportunity for further theoretical and experimental work into the fundamental properties of these devices. The other avenue of research is into developmental work into composite cavity designs for Q-switched microchip lasers and microchip lasers of different colours.

From the work on the fundamental operating characteristics of microchip lasers much could be done on the cavity stability regimes present in Nd:YVO_4 microchip lasers. This material provides a regime which may possibly be a blend of input surface deformation as, LNP microchip lasers, though with a contribution from a distributed waveguide within the material as Nd:YAG microchip lasers. Additionally, the remaining regime still as yet not thoroughly investigated, is the combination of negative dn/dT, as in LNP, but relatively uniform pump absorption, as in Nd:YAG. One such material which combines these physical properties is neodymium-doped strontium fluorovanadate (or Nd:S-VAP for short). Preliminary experiments on an Nd:S-VAP infra-red microchip laser have indicated the existence of quite severe

pump-induced thermally-related problems. These difficulties appear to severely limit the output power possible from this material in a microchip laser despite the existence of a $\sigma_{em}.\tau_{f.}$ product larger than that for 1 % doped Nd:YVO_4. The transverse mode structure of the output beam however does not appear to degrade with increasing pump power.

The developmental work still possible in the field of microchip lasers remains quite large. The composite material design which has been exploited in this thesis to provide green output may also be exploited so as to produce different colours especially in the blue and the red. Perhaps this principle may also be applied to frequency down-conversion again, perhaps using KTP, of the 1 μm light from Nd:YVO_4. Such an "eyesafe" microchip laser could perhaps supersede the present use of more exotic rare earth ions some of which have quasi-three level systems, such as Ho^{3+} or Tm^{3+}, and consequently relatively inefficient lasing regimes. The above composite material designs realising different visible, or eyesafe, wavelengths of operation may be applied to arrays of laser diodes to produce linear or two-dimensional arrays of microchip laser emitters.

Further work could be devoted to the development of Q-switched microchip lasers of higher pulse energies. The disadvantage of the current method of Q-switching microchip lasers i.e. that using a resonant reflector as a voltage controlled output coupler is that the device must run single frequency. A bias voltage must also be applied to the non-linear section such that before Q-switching is possible the free spectral range of the non-linear section is an integral multiple of that of the gain section. This particular method is well suited to single element devices but has a number of significant drawbacks when used to switch either one or two dimensional arrays. In an array of such devices the optical thickness of each of the component sections requires a different bias voltage and Q-switching voltage.

Using a voltage controlled electro-optic deflector as outlined in a proposed Q-switched microchip laser would overcome this problem.

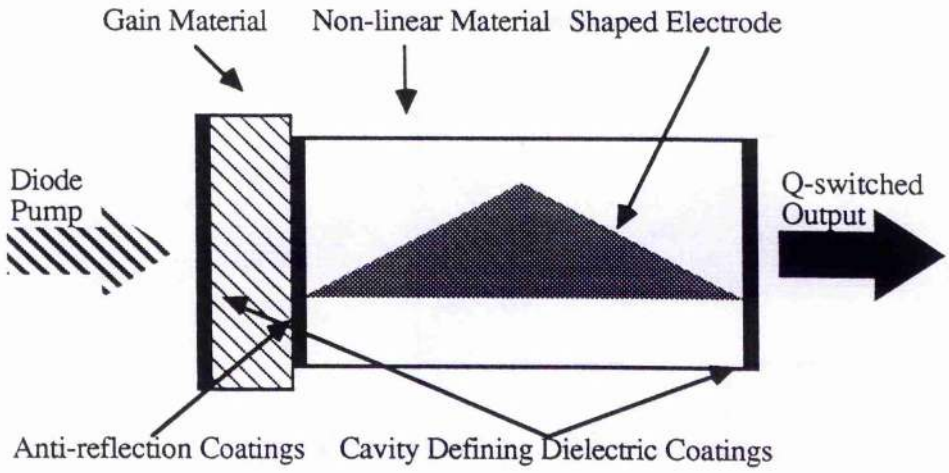

Figure 6.2.1: Proposed Q-switching Scheme for Microchip Laser Based Electro-optical Cavity Misalignment

The electro-optic deflection method relies on the sensitivity of microchip laser cavities to angular misalignment, or wedging, between input and output surfaces. When a voltage is applied to the shaped electrode the non-linear beam behaves like a prism deflecting the path of the beam which is polarised in parallel to the direction of the applied electric field. This effectively introduces a significant wedge between the input and output surfaces. Different cavity stability regimes will require different amounts of hold-off voltage but the above approach has the advantage that the hold-off of lasing is insensitive to the actual magnitude of the voltage as long as it is above a certain level. The above method is non-wavelength specific so in a linear array of microchip lasers, each having a slightly different wavelength of operation, a single Q-switching voltage may hold-off the whole array. The electro-optical deflector may therefore be employed to hold-off devices which are much further above threshold. This coupled with gain media with longer upper state lifetimes may facilitate higher peak power microchip lasers.

Clearly the microchip laser concept has, since its inception a few years ago, begun to move into areas previously the domain of larger bulk holosteric laser systems. The work presented in this thesis has, we hope, made a significant contribution to this

process. There is no doubt that this process will continue apace as the current material, laser diode and coating technology matures.

Appendix A: Derivation of Correlation Factor <ψ(1,2)> for Microchip Laser

In chapter four the correlation factor <ψ(1,2)> for a microchip laser was discussed. The correlation factor which expressed the normalised integrated gain common to two longitudinal modes saturating an inversion density in a homogeneous laser medium []. The correlation coefficient between the principal axial mode (mode 1) and the m^{th} cavity mode was given by Zayhowski as being.

$$\langle\psi(1,2)\rangle \equiv \frac{1}{L\langle N_0\rangle}\int_0^L N_0(z)\cos\eta dz \qquad \text{Eqn A.1}$$

Where η is the phase difference between the two field patterns associated with the two axial modes and is given by.

$$\eta = 2(k_1 - k_2)z \qquad \text{Eqn. A.2}$$

The correlation coefficient is normalised with respect to the unsaturated inversion density and cavity length L. Assuming that both modes have a nodal point at the input mirror and calling $(k_1-k_2)=\Delta k$.

$$\langle\psi(1,2)\rangle \equiv \frac{1}{L\langle N_0\rangle}\int_0^L N_0(z)\cos 2\Delta kzdz \qquad \text{Eqn. A.3}$$

$$\langle N_0\rangle \equiv \int_0^L N_0(z)dz \qquad \text{Eqn. A.4}$$

Where $N_0(z)$ is the saturated inversion density and is given by $N_0(z)=N_{00}e^{-\alpha z}$ where α is the absorption coefficient of the pump light within the material and N_{00} is the instantaneous value of the inversion density at the input surface of the device. Consider the integral portion of equation A.3. This will have the form of the standard integral [1].

$$\int e^{ax}\left[\cos^n(bx)\right]dx \qquad \text{Eqn. A.5}$$

Where in a=-α, n=1, b=2Δk and z=x. The solution to the standard integral given by equation A.4 is.

$$\frac{1}{a^2+n^2b^2}\left[\begin{array}{l}(a\cos bx+\ nb\sin bx)e^{ax}\cos^{(n-1)}bx \\ \quad +\ n(n-1)b\int e^{ax}\left[\cos^{(n-2)}bx\right]dx\end{array}\right] \qquad \text{Eqn. A.6}$$

Adapting the above solution appropriately to the integral part of equation A.3 gives.

$$\int_0^L N_0(z)\cos(2\Delta kz)dz=\frac{1}{\alpha^2+(2\Delta k)^2}\left[\begin{array}{l}e^{-\alpha z}(-\alpha\cos 2\Delta kz\ + \\ 2\Delta k\sin 2\Delta kz)\end{array}\right]_0^L \qquad \text{Eqn. A.7}$$

Therefore the correlation coefficient now becomes.

$$\langle\psi(1,2)\rangle\equiv\frac{1}{L\langle N_0\rangle}\frac{1}{\alpha^2+(2\Delta k)^2}\left[\begin{array}{l}e^{-\alpha z}(-\alpha\cos 2\Delta kz \\ +\ 2\Delta k\sin 2\Delta kz)\end{array}\right]_0^L \qquad \text{Eqn. A.8}$$

It may be shown that.

$$\frac{1}{L}\int_0^L N_0(z)dz=\langle N_0\rangle=-\frac{N_{00}}{L\alpha}\left[e^{-\alpha L}-1\right] \qquad \text{Eqn. A.9}$$

Evaluating the limits in equation A.7 and substituting equation A.9 into equation A.7 gives.

$$\langle\psi(1,2)\rangle\equiv\frac{-\alpha}{e^{-\alpha L}-1}\left(\frac{1}{\alpha^2+4\Delta k^2}\right)\left(e^{-\alpha L}(-\alpha\cos 2\Delta kL\ +\ 2\Delta kL\sin 2\Delta kL)\ -\ \alpha\right) \qquad \text{Eqn. A.10}$$

Knowing that $2\Delta kL=2(m_1-m_2)\pi$ the bracketed term in the above equation containg the sinusoidal terms reduces to.

$$\left(-\alpha e^{-\alpha L}\ +\ \alpha\right) \qquad \text{Eqn. A.11}$$

Substituting the above equation into equation A.10 and re-arranging gives the correlation factor between the principal axial mode , mode 1, and the m th axial mode.

$$\langle \psi(l,m) \rangle = \frac{1}{1 + \left(\frac{2\Delta m \pi}{L\alpha}\right)^2} \qquad \text{Eqn. A.12}$$

Where Δm is the difference in axial mode numbers between the modes being considered.

References

[1] C.R.C. Handbook of Chemistry and Physics, 53rd Edition, Weast, 1972, p. A155